Development and Testing of Instrumentation for Space-Based Ultraviolet and X-Ray Astronomy

Dissertation

der Mathematisch-Naturwissenschaftlichen Fakultät
der Eberhard Karls Universität Tübingen
zur Erlangung des Grades eines Doktors
der Naturwissenschaften (Dr. rer. nat.)

vorgelegt von

Sebastian Diebold

aus Tübingen

2015

Tag der mündlichen Qualifikation: 24. März 2015
Dekan: Prof. Dr. Wolfgang Rosenstiel
1. Berichterstatter: Prof. Dr. Klaus Werner
2. Berichterstatter: Prof. Dott. Andrea Santangelo

Abstract

Since the atmosphere of the Earth is opaque for ultraviolet (UV) and X-ray radiation, space-based observatories are crucial for astronomical studies and scientific progress in these domains. The two key aspects of this thesis are both related to future astronomical satellite missions and concern the development of a position sensitive UV detector and the reliability assessment of silicon X-ray sensors.

An advanced microchannel plate (MCP) detector for the UV band is currently under development at the IAAT. High sensitivity, a large dynamic range, long term stability, and a low power dissipation are the necessary requirements to push the performance and lifetime of future UV missions and, therefore, are the key drivers of this effort. Besides the production of efficient photocathodes, the main innovation to reach these goals is the application of a cross-strip anode. This kind of anode has not been used in spaceborne UV detectors so far, particularly because the development of low power front-end electronics is challenging due to a large number of readout channels. A test setup equipped with MCPs to generate realistic signal stimuli for the readout electronics under development has been designed and constructed as part of this thesis.

The second part of this thesis concerns studies of the effects of orbital low energy proton radiation on X-ray sensors. These soft protons can seriously degrade the photon detection performance and are potentially more harmful than energetic protons. Furthermore, instruments with grazing incidence X-ray optics concentrate the ambient orbital proton flux in their focal plane, where the sensors are located. Soft proton radiation is thus considered a major risk to future X-ray missions such as *eROSITA*, *LOFT*, and *Athena*, requiring a thorough assessment and mitigation strategy. Within this work, a unique soft proton irradiation experiment has been set up at the local accelerator facility. It features an unprecedented high flux uniformity over a large area and a monitoring system for the spectrum and the fluence. The setup has been used in two irradiation campaigns for *LOFT* sensor prototypes and for the irradiation of coated optics for *ADM-Aeolus*, a future satellite mission to map Earth's global wind profiles. A recent upgrade of the setup enables measurements of the grazing angle soft proton scattering efficiency of which experimental data was scarcely available up to now. Systematic measurements with samples of *eROSITA* spare mirror shells have been performed. The results deviate from previous measurements and show limitations of widely used simulation codes. The data will be used as an input for a novel ray tracing software dedicated to model proton propagation through X-ray optics.

Zusammenfassung

Die Erdatmosphäre ist opak für ultraviolettes (UV) Licht und Röntgenstrahlung. Der Betrieb von Observatorien im Weltraum ist deshalb eine entscheidende Grundvoraussetzung für astronomische Untersuchungen und den wissenschaftlichen Fortschritt in diesen Wellenlängenbereichen. Die vorliegende Arbeit befasst sich mit dem Entwurf und der Planung von Messinstrumenten für derartige Satellitenmissionen. Die beiden Schwerpunkte der Arbeit betreffen die Entwicklung eines weltraumtauglichen positionsempfindlichen UV-Detektors sowie die Evaluation der Zuverlässigkeit von siliziumbasierten Röntgendetektoren.

Das IAAT entwickelt derzeit einen neuartigen Mikrokanalplatten-Detektor für UV-Licht. Hohe Sensitivität, ein großer Dynamikumfang, gute Langzeitstabilität und eine geringe Wärmeabgabe sind dabei wichtige Voraussetzungen für eine verbesserte Leistungsfähigkeit und Lebensdauer des Instruments und Ziel dieser Bemühungen. Neben der Produktion effizienter Photokathoden ist der Einsatz einer sogenannten Cross-strip-Anode die zentrale Innovation. Dieser Anodentyp wird bislang in weltraumgebundenen UV-Detektoren nicht eingesetzt, weil insbesondere die Entwicklung einer Ausleseelektronik mit geringer Wärmeabgabe für die große Zahl an Kanälen eine Herausforderung darstellt. Um realistische Auslöseimpulse für die sich in der Entwicklung befindliche Ausleseelektronik zu erzeugen, wurde im Rahmen dieser Arbeit ein mit Mikrokanalplatten bestückter Testaufbau entworfen und umgesetzt.

Der zweite Teil dieser Arbeit befasst sich mit den Auswirkungen von orbitaler niederenergetischer Protonenstrahlung auf Röntgendetektoren. Diese sogenannten weichen Protonen können die Fähigkeit dieser Instrumente zur Photonendetektion empfindlich verschlechtern und sind potentiell schädlicher als höherenergetische Protonen. In Röntgenteleskopen mit fokussierender Optik wird darüber hinaus der orbitale Protonenfluss auf die Detektoren in der Fokalebene konzentriert. Weiche Protonenstrahlung wird aus diesen Gründen als ein Hauptrisiko für zukünftige Röntgenmissionen wie *eROSITA*, *LOFT* und *Athena* betrachtet; eingehende Untersuchungen und vorbeugende Maßnahmen sind erforderlich. Aufbau und Durchführung eines einzigartigen Bestrahlungsexperiments an der Beschleunigeranlage der Universität waren deshalb ebenso Bestandteil dieser Arbeit. Das Experiment zeichnet sich durch eine bislang unerreichte Gleichmäßigkeit der Flussverteilung aus und besitzt ein Messsystem für die spektrale Energieverteilung und die applizierte Dosis, das vom bestrahlten Objekt unabhängig ist. Der Aufbau wurde für zwei Bestrahlungskampagnen für *LOFT*-Detektorprototypen verwendet sowie für die Bestrahlung beschichteter Optiken für *ADM-Aeolus*, eine zukünftige Satellitenmission zur Kartierung globaler Windprofile in der Erdatmosphäre. Eine kürzlich erfolgte Erweiterung des Auf-

baus ermöglicht Messungen der Streueffizienz niederenergetischer Protonen unter streifendem Einfall, wofür experimentelle Daten bisher kaum verfügbar waren. Systematische Messungen wurden an Proben von *eROSITA*-Reservespiegelschalen durchgeführt. Die Ergebnisse weichen von bisherigen Messungen ab und zeigen Beschränkungen vorherrschender Simulationen auf diesem Gebiet auf. Sie dienen zudem als Grundlage einer neuartigen Raytracing-Software, die zur Modellierung der Protonenpropagation durch Röntgenoptiken bestimmt ist.

Contents

Contents

1 Introduction

The atmosphere of the Earth is opaque for a predominant fraction of the electromagnetic spectrum. This is illustrated in Fig. 1, which shows the atmospheric optical depth as a function of altitude and wavelength. In the optical (380–780 nm) and in the radio band ($\sim 1\,\mathrm{mm}$–$10\,\mathrm{m}$), as well as in several narrow windows in the near-infrared, a sufficient transmittance allows ground-based astronomy. In contrast, UV radiation (92–310 nm) can only penetrate down to 50–100 km above sea level, extreme UV (10–92 nm) and soft X-ray radiation (100 eV–10 keV) are absorbed at even higher altitudes around 150 km, whereas hard X-rays (10 keV–500 keV) can reach down to about 40 km. The dominant absorption processes are dissociation and ionization of atmospheric molecules such as oxygen, nitrogen, and ozone (Davies, 1997).

Astronomical observations in the UV and the X-ray band depend on the operation of instruments at sufficiently high altitudes, ultimately deployed in space. Although sounding rockets can reach apogees of several hundred kilometers, the maximum observing time is limited to about 20 minutes[1]. Recently developed Ultra-Long Duration Balloons (ULDBs) attain flight durations of up to 100 days, but their altitude limit is around 35 km (Brosch, 2009). Most missions using these platforms are thus primarily focused on the test and qualification of novel instrumentation, whereas observatory class spaceborne telescopes that are comparable to ground-based facilities usually rely on satellites.

The development, launch, and operation of satellite observatories demands extensive financial resources. The extremely high costs of space-qualified hardware are due to the requirements posed by the harsh orbital environment, in particular the thermal and radiation conditions. In order to ensure high reliability, specially selected components as well as extensive development and qualification efforts for the telescope and for all of its subsystems are required. Once deployed in orbit, a satellite is literally on its own – repairs are not possible and the smallest fault in the instrumentation can terminate the mission. However, some space observatories have proven a successful operation in Earth orbits over a time period of 15 years or even longer and

---

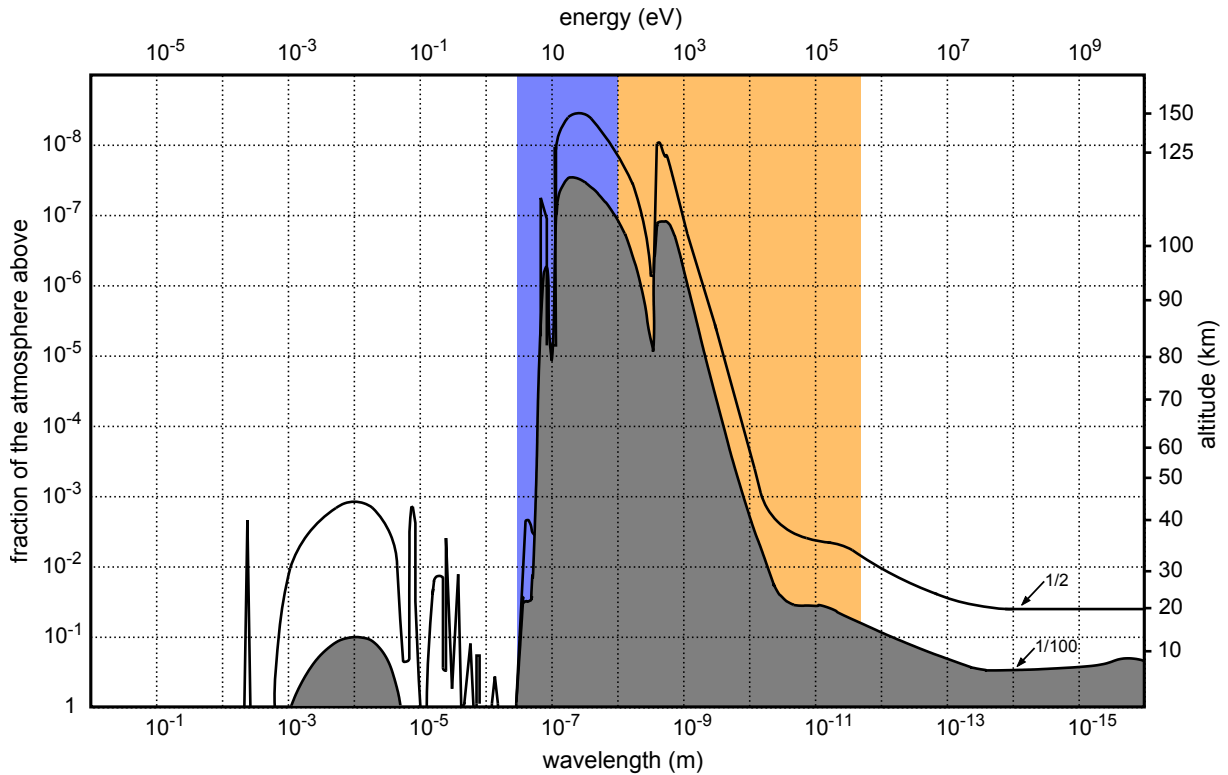[1] `http://rscience.gsfc.nasa.gov/srrov.html`

Figure 1.1: Plot of the atmospheric optical depth as function of wavelength and energy. The scale on the left gives the fraction of the atmosphere above a certain altitude, while the scale on the right lists the corresponding altitude. The black solid line marks the atmospheric depth at which half of the incident flux is absorbed; at the top of the gray shaded area one percent of the incident flux remains. The UV domain, including the extreme UV, is colored in blue; the X-ray band in orange (Giacconi et al., 1968, digitized by T. Schanz, modified)

are still delivering high quality data; examples are the *Hubble Space Telescope*[2] and the *Chandra X-Ray Observatory* (Weisskopf et al., 2003) of the NASA, as well as ESA's *X-ray Multi Mirror* (*XMM-Newton*) mission (Jansen et al., 2001).

The present cumulative dissertation is focused on the development and the reliability assessment of detectors for future astronomical space missions. It comprises four articles, all of which are published in peer-reviewed journals. The objectives of the performed studies are presented in Chapter 2. The work covers three domains: Chapter 3 deals with the development efforts for a *detector for ultraviolet (UV) radiation*, whereas the related topics *soft proton radiation hardness of sensors for X-ray astronomy* and *proton propagation through focusing X-ray optics* are addressed in Chapter 4. In both chapters, the context of the work is introduced, the content

---

[2]`www.stsci.edu/`

of the publications is briefly summarized, and the reported results are touched. Discussions of various aspects that could not been explained sufficiently deep within the publications, i.e. the principles of different X-ray sensors, are included as well. Furthermore, a brief summary of a soft proton irradiation campaign for a future Earth observation satellite mission is given in Chapter 4, in order to highlight an additional application of the developed experimental setup. The four journal articles are reprinted in Chapter 5. Chapter 6 concludes with a summary and gives an outlook on future prospects.

2 Objectives of the Doctoral Research

The scientific objectives of this doctoral thesis subdivide into three domains, each associated with the development of spaceborne astronomical instrumentation:

1. In the context of the development and construction of a microchannel plate (MCP) detector for the UV wavelength range, a test bench was required to verify the functionality of a novel position sensitive cross-strip anode (CSA) and the associated readout electronics under realistic operation conditions. In contrast to previous tests of the electronics with a charge injector, this setup should provide the possibility to mount and operate MCPs in order to generate charge clouds on a CSA prototype in a way comparable to the final sealed-tube detector configuration. Furthermore, the setup was intended for the initial conditioning of factory new MCPs, which is essential to achieve a uniform and stable gain, and thus required a mechanism to move an additional MCP in and out of the front of the MCP stack without breaking the vacuum.

2. The second objective was the experimental study of the radiation hardness of silicon drift detector (SDD) prototypes designated for the use on-board the proposed *Large Observatory For x-ray Timing* (*LOFT*). A setup had to be constructed for the uniform irradiation of $7.25 \times 5.52 \, \text{cm}^2$ sensor prototypes with soft protons in the energy range $100 \, \text{keV}$–$1 \, \text{MeV}$. The proton flux had to be adjustable over a wide range to achieve reasonable irradiation durations between several minutes and about an hour to reach the requested fluences from a few percent up to a factor of ten of the expected orbital fluence. Since readout electronics for the SDD prototypes were not yet available, an independent monitoring system was required to measure applied fluences and spectra, as well as a procedure to determine the uniformity of the spatial flux distribution. Methods for an energy calibration and for the normalization of the fluence measurement had to be developed and evaluated. Various particle transport simulations were necessary to dimension the setup adequately and to suppress unwanted background that distorts the irradiation spectra.

3. As a third objective of the doctoral studies, the collection of experimental data of grazing angle soft proton scattering on focusing X-ray optics was selected. Therefore, the mentioned irradiation setup had to be upgraded with a target mounting that is adjustable with an angular precision better than 0.1°. Procedures had to be developed for the determination of the scattering angle and the calibration of the incidence angle and a reliable method for the determination of the incident proton flux on the target had to be found. Samples of spare mirror shells of *eROSITA* (*extended ROentgen Survey with an Imaging Telescope Array*), which will be the main instrument on the upcoming *SRG* (*Spectrum-Roentgen-Gamma*) satellite, should be used as scattering targets. The goal was to validate a theoretical model and existing simulation codes as well as to provide empirical input for a novel ray tracing code dedicated to simulate proton propagation through X-ray optics.

3 Detector Development for UV Astronomy

3.1 Context of the Development

The development of detectors based on MCPs for visible and UV radiation started at the AIT[1] in the 1980s (Barnstedt, 1985). The expertise gained from this initial work was successively extended to construct a detector that meets the requirements for an application in space. The effort culminated in two successful orbital flights of AIT MCP UV detectors in the *TUES* (*Tübingen Echelle Spectrograph*) instrument on-board of the *ORFEUS-SPAS* (*Orbiting and Retrievable Far and Extreme UV Spectrometer - Shuttle Pallet Satellite*) missions in 1993 (STS-51) and 1996 (STS-80) (Grewing et al., 1998).

Already at that time, Russia proposed an observatory class UV telescope, *Spektr-UV*, which was renamed later as *WSO-UV* (*World Space Observatory-Ultraviolet*) (Shustov et al., 2009). Although started as a national project, *Spektr-UV* was opened in the 1990s for international contributions and several nations joined the collaboration. Amongst them was Germany with the AIT, which was responsible for the development of the mission's main instruments and the associated detectors. The main instruments were a two channel echelle spectrograph (*HIRDES – High Resolution Double Echelle Spectrograph*) with a spectral resolution $R = \lambda/\Delta\lambda \approx 50\,000$ (Becker-Ross et al., 1994; Werner et al., 2008) and a long slit spectrograph (*LSS*) with $R \approx 1000$. Both instruments had been designed for the application of *solar-blind* and *photon-counting* detectors that allow photon-noise limited observations. Particularly, intrinsic solar-blindness is a unique feature of MCP detectors that other technologies such as CCDs (Charge-Coupled Devices; cf. Sec. 4.1 and Fig. 4.3) cannot offer. Advanced MCP detectors and the associated readout electronics were thus newly developed at the IAAT, to meet the demands for a higher sensitivity and a larger dynamic range than the *ORFEUS* detector could provide, while pushing the power dissipation below $10\,\mathrm{W}$ and extending the detector lifetime. Even though the German participation in the *WSO-UV* mission was canceled in 2013, the detector development at the IAAT

---

[1]Astronomical Institute Tübingen; today: IAAT – Institute for Astronomy und Astrophysics Tübingen

was continued with the same requirements, since these arose from constraints that are generic for the application in spaceborne UV instruments.

3.2 Microchannel Plate Detectors

MCPs have been used in a wider range of particle and photon detection problems than perhaps any other detector type (Fraser, 1989). The technology can be applied for the detection and high resolution imaging of particles, e.g. protons, ions, electrons, and neutrons, as well as photons from the optical band up to X-ray energies. MCP detectors are counting devices that are not providing energy information. For UV spectroscopy usually dispersive optics are connected to a position sensitive MCP detector. In the following, the principle of MCP based UV detectors is explained and the specific innovations in the detector design under development at the IAAT are highlighted.

3.2.1 Photon Detection Principle

The principle of a position sensitive MCP UV detector is illustrated in Fig. 3.1. The photon detection process can be separated in four steps:

1. The *conversion* process, in which an incident UV photon generates with a certain probability a photoelectron (PE) that exits the photocathode. The probability for this initial process determines primarily the quantum efficiency (QE) of the detector. Since it depends on the material and the wavelength, the bandpass in which the detector is sensitive can be chosen via the selection of the photocathode material. Particularly, detectors for the UV can be made solar-blind, i.e. insensitive to visible light. This simplifies the development of connected instruments such as spectrographs, since visible stray light does not affect the signal-to-noise ratio.

2. The *multiplication* of the PE in a stack of MCPs. An illustration is shown in Fig. 3.2. An MCP is a glass plate in which microscopic channels are etched to form a dense array of parallel oriented miniature electron multipliers (Wiza, 1979). The channels are coated with a semiconducting material, which acts as voltage divider and continuous dynode. The channel diameter ultimately limits the position resolution of an MCP detector. While MCPs with 4 µm channels are available, typically channels with 10 µm or even larger diameters are used because of the considerably larger open area. The gain depends on the
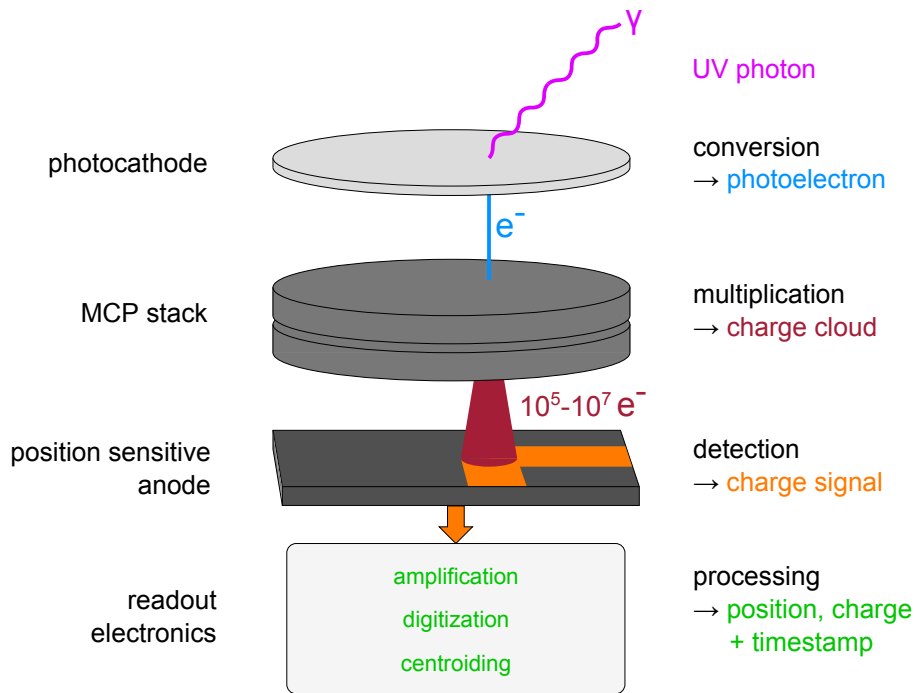
Figure 3.1: Principle of a position sensitive MCP detector for photon detection. A UV photon that hits the photocathode can produce a photoelectron (PE). If this electron exits the photocathode, it is accelerated towards a stack of MCPs. The MCPs multiply the initial PE with a typical gain of 10^5–10^7 (cf. Fig. 3.2). The exiting electron cloud is detected on a position sensitive anode. The charge signals from the anode are digitized in the readout electronics and the centroid is determined which corresponds to the position of the initial photon.

length-to-diameter ratio of the channels (typical around 80:1) and the applied high voltage (HV). The maximal gain of a single MCP is about 10^4, while a stack of two MCPs can reach 10^7.

3. The *detection* of the charge cloud exiting the MCPs. Various types of position sensitive anodes exist, which code the position of the charge cloud either in the charge distribution on different electrodes (wedge-and-strip, resistive, or cross-strip anode) or in the time-of-arrival difference of signals at the two ends of an electrode (delay-line anode). Since each type has a different electrode capacitance, the choice of the anode determines the amount of charge that is required to achieve a certain position resolution and, therefore, defines the needed operational gain of the MCPs.

4. The *processing* of the charge signals in the readout electronics. Each channel has to be equipped with a charge-sensitive preamplifier, a shaper, and an analog-to-digital converter (ADC). Some systems multiplex several channels onto one ADC. A trigger signal can be
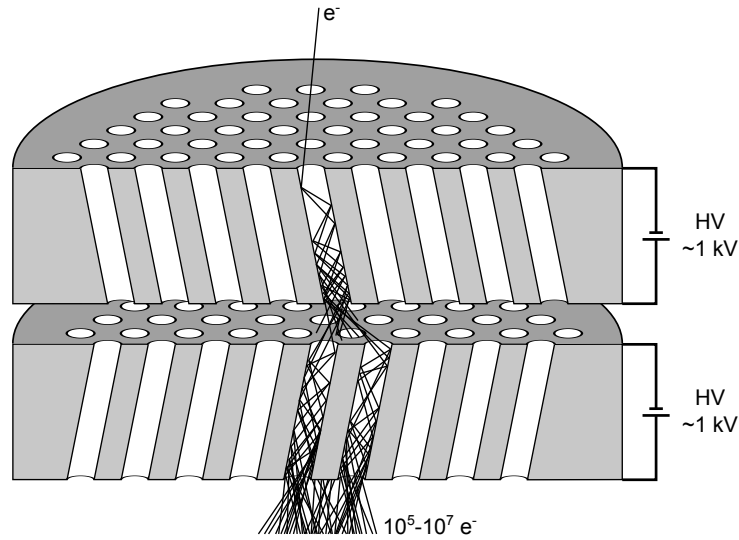
Figure 3.2: Cross-section of a stack of two MCPs. A high voltage of the order of 1 kV per MCP is applied. If a photon or charged particle hits a channel, secondary electrons are produced. These are accelerated in the electric field, generate additional electrons when impacting on the channel wall, and thus form a charge avalanche. The channels are slightly inclined to maximize the impact probability and to prevent feedback from positive ions that are generated when electrons collide with residual gas atoms or molecules.

generated within this chain, digitally, or from the HV of the MCPs. The initial photon position is determined by calculating the centroid of the charge cloud and output together with a timestamp. The complexity and power dissipation of the readout electronics depend primarily on the number of input channels and are influenced by the type of anode.

MCPs can only be operated under vacuum conditions, where the mean free path of electrons is large compared to the typical distances in the detector, otherwise the accelerated electrons ionize large amounts of gas molecules and the high current destroys the channel walls. Furthermore, most photocathode materials are hygroscopic or degrade under exposure to oxygen. These constraints make basically two types of detector configurations possible: the *open-face* and the *sealed-tube* type. An *open-face* detector can only be operated inside a vacuum chamber or in space. It uses an opaque photocathode, which is deposited directly onto the first MCP. For far-UV wavelengths below about 102 nm, for which no transparent window material exists, only this type is feasible. The drawback is the need for a shutter to transport and handle such a detector under atmospheric conditions. The alternative are *sealed-tube* detectors with an entrance window that is transparent for UV radiation, e.g. quartz or MgF_2. A semitransparent photocathode can be coated on the inner side of the window. The QE of semitransparent photocathodes depends strongly on the thickness: if the layer is too thin, it absorbs only a small portion of the incoming

photons. On the other hand, a layer that is too thick suppresses the exiting of the generated PEs. In order to balance both effects, the thickness has to be within a small margin. In principle, the combination of a semitransparent cathode on the window and an opaque cathode on the first MCP should be feasible to maximize the QE.

3.2.2 Developments and Innovations

A comprehensive description of the sealed-tube MCP detector under development is given in Diebold et al. (2013b) (cf. Sec. 5.1). The detector design comprises two main innovations for a spaceborne UV detector: a GaN photocathode and a cross-strip anode (CSA). Cesium activated GaN promises a superior QE in the whole UV band compared to state-of-the-art materials such as CsTe for the near-UV and CsI for the far-UV (Siegmund et al., 2008; Dabiran et al., 2009). However, the reproducible production of highly efficient semitransparent GaN on MgF_2 is difficult, thus the deposition of CsTe is also pursued simultaneously as an alternative (Hermanutz et al., 2014).

The principle of a CSA (Tremsin et al., 2003; Vallerga et al., 2010) is explained in Fig. 3.3. Due to the smaller electrodes of a CSA compared to other anode types, the capacitance is lower and, therefore, a specific spatial resolution can be achieved with a smaller amount of charge, i.e. at lower MCP gains. Since the aging of MCPs – a degradation of the gain due to changes of the secondary emission coefficient of the channel walls as described in Wiza (1979) – is coupled to the amount of extracted charge, a lower gain directly increases the lifetime. The main difficulty of the implementation of a CSA in the detector for a UV instrument is the large number of channels – 128 in the present design – combined with restrictions on the power dissipation of the readout electronics as well as spatial constraints on the system. A possible solution was found in the BEETLE readout chip (Löchner, 2006; Löchner and Schmelling, n.d.), which had originally been developed at the Max-Planck-Institute for Nuclear Physics in Heidelberg for the vertex detector of the *LHCb* experiment at CERN (Volyanskyy, 2013). This chip features 128 input channels, each equipped with a charge-sensitive preamplifier, a shaper, and a ring buffer. When an event triggers the readout, a defined number of samples from the ring buffers are multiplexed and output on one to four channels. The need of just one to four ADCs for 128 channels and its low power dissipation make the BEETLE an ideal candidate for the front-end electronics of a CSA.
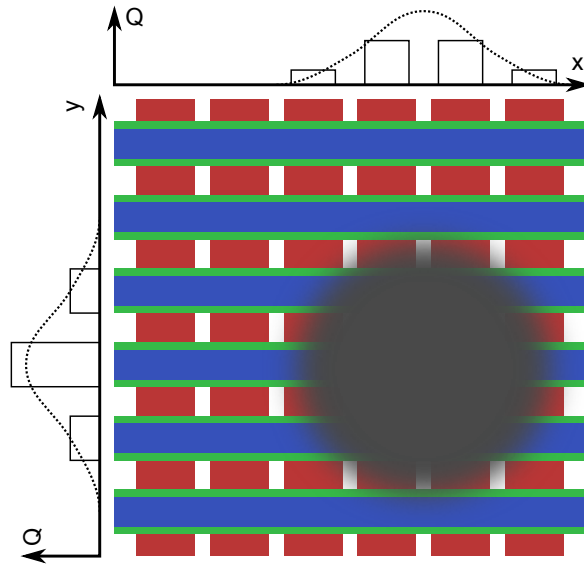
Figure 3.3: Schematic diagram of a cross-strip anode. The bottom strips (red) code the position in x-direction and the top strips (blue) the y-position. Top and bottom strips are separated by an insulating layer (green). The bottom strips are wider than the top strips to achieve an equal open area. The charge cloud from an MCP stack (grey) spreads over several strips in both directions, which gives rise to a centroiding accuracy considerably smaller than the strip pitch.

3.3 MCP Test Setup

An evaluation PCB (Printed Circuit Board) for the BEETLE chip, on which ten channels of its 128 inputs are bonded, was included in a test bench for commissioning the chip. A specifically developed ten channel charge injector provided input signals; a single ADC was used for the readout (Pfeifer et al., 2014). Output waveforms obtained with this setup were published in Diebold et al. (2013b) (cf. Sec. 5.1). The next step towards BEETLE-based readout electronics was the construction of an MCP test setup that is similar to the final detector configuration. The designing and manufacturing of the test setup was a part of the present thesis. The intention was to test the prototype electronics under realistic conditions with charge pulses from an MCP stack. A CAD model of this setup had been included in Diebold et al. (2013b) (cf. Sec. 5.1), an updated version is shown in Fig. 3.4. A quartz window allows to illuminate the setup with a mercury lamp that emits strong lines in the UV down to 184.9 nm (Wilkinson and Andrew, 1963). A stack of two MCPs with 40 mm active diameter is used without a photocathode, since the intrinsic conversion efficiency is sufficient for test purposes. Trigger rates up to several kHz could be reached in this configuration. The anode is mounted on a shiftable holder to study
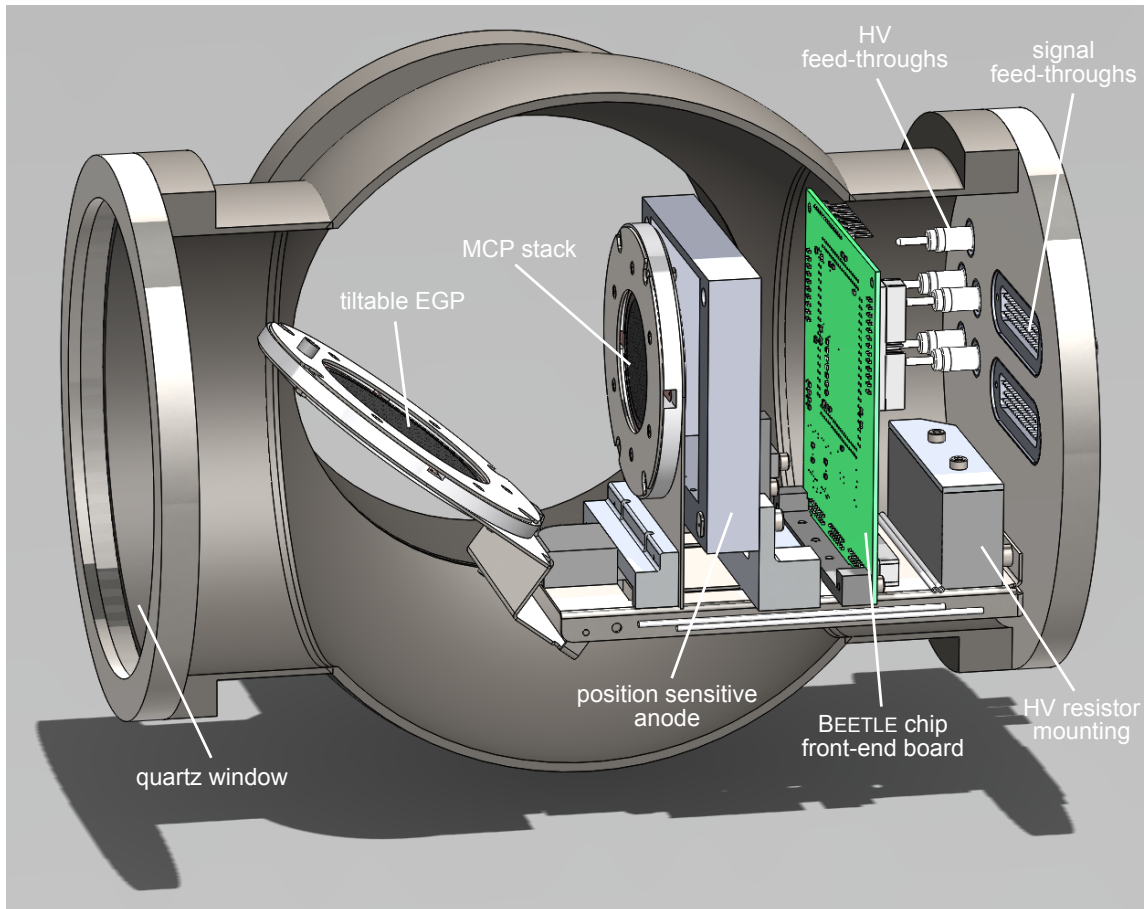
Figure 3.4: CAD drawing of the MCP test setup developed as part of this thesis. The vacuum chamber has a quartz window for UV illumination of the MCP stack by means of an external mercury lamp. A position sensitive anode can be mounted on a shiftable holder and connected to the inputs of a BEETLE chip. Two 50-pin Sub-D feed-throughs are used for data signals; five SHV (Save High Voltage) feed-throughs connect the MCP stack and the tiltable EGP (Electron Generator MCP) via HV resistors mounted below.

how different distances to the MCPs influence the width of the charge cloud and to determine the optimal distance to the cross-strip anode.

A tiltable mounting in front of the MCP stack is designed to hold an Electron Generator MCP (EGP) with an active area of 60 mm. An EGP is a specially fabricated MCP that emits electrons all-over its area when a high voltage is applied. The flux density is typically exceeding 10^{-10} A/cm^2 with a uniformity $\pm 10\%$ (Photonis, 2009).

The conditioning of an MCP stack for the operation in a detector was not used up to now, but first measurements with an *ORFEUS* wedge-and-strip anode were made inside the vacuum
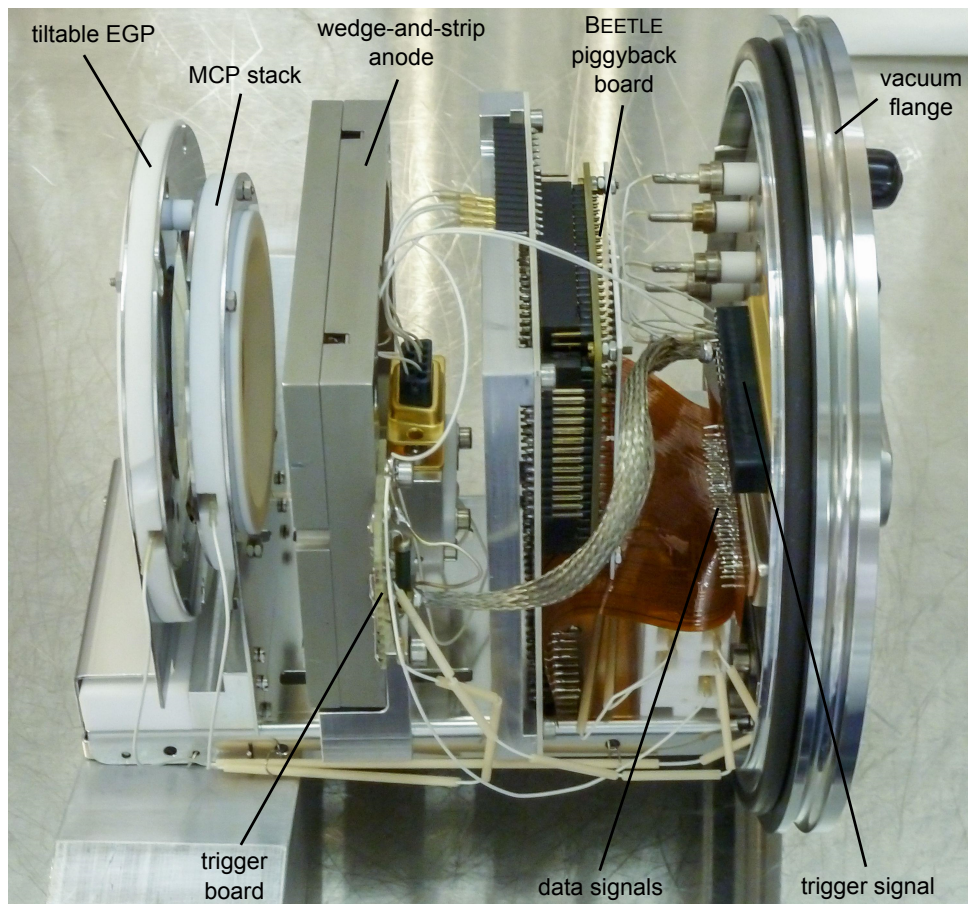
Figure 3.5: Picture of the fully assembled and equipped interior of the MCP test setup mounted on a vacuum flange. The tiltable EGP on the left is in its upper position in front of the MCP stack. An *ORFEUS* wedge-and-strip anode is mounted for first measurements; its four electrodes are connected to a Beetle chip, which is mounted on a piggyback board. The HV cabling is routed through ceramics tubes to avoid sparks. The lower Sub-D feed-through leads out the data signals, while the upper one is used for the trigger signal, which is coupled out from the MCP HV on a small dedicated board.

chamber. Fig. 3.5 gives an impression of the fully assembled and equipped MCP test setup that is fixed on a vacuum flange. The measured data are included in Pfeifer (2014).

4 Soft Proton Effects on Astronomical X-Ray Instruments

4.1 Context of the Studies

Satellites are exposed to various kinds of particle radiation: protons and electrons that are trapped in the Earth magnetic field, solar wind particles, and energetic particles of extrasolar origin, the cosmic rays. The radiation environment of a specific mission, i.e. particle types and spectra, depends strongly on the orbit and varies with the solar activity. The orbital dependence is illustrated in Fig. 4.1 that shows the South Atlantic Anomaly (SAA) – a region where the inner radiation belt reaches low altitudes due to the non-alignment of the rotation and the magnetic axes of the Earth. For astronomical X-ray observatories proton radiation is usually the major component to be assessed; its main effects on X-ray instruments are *degradation of the detector performance* and contribution to the *observational background.*

Protons deposit energy via ionization, also referred to as electronic stopping or TID (Total Ionizing Dose), and scattering on nuclei – nuclear stopping or NIEL (Non-Ionizing Energy Loss), which causes a displacement of lattice atoms and, therefore, creates vacancies. The plots in Fig. 4.2 show the range of protons in silicon and the contributions of ionization and nuclear stopping to the total stopping power. Protons with energies below $8\,\mathrm{MeV}$ are stopped within $500\,\mathrm{\mu m}$ of silicon, the maximum thickness of silicon sensors for X-rays. Accordingly, for this context the soft proton energy range is defined from a few keV up to several MeV. Soft protons are potentially more harmful than energetic protons, since the energy deposition per unit length is larger and the displacement damage is highly concentrated in a small volume around the stopping point. X-ray sensors cannot be shielded efficiently against this radiation without sacrificing the X-ray detection efficiency, particularly at low energies.

In silicon based X-ray sensors both interactions – ionization and nuclear stopping – can contribute to a degradation of the detection performance (Spieler, 2005). Ionization in an insulating
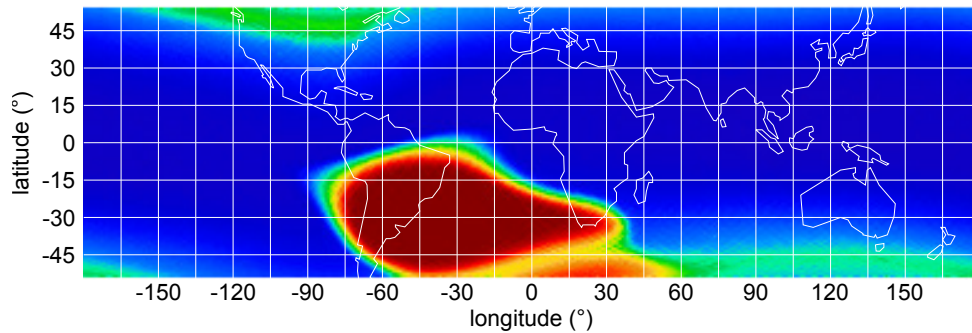
Figure 4.1: Map of the charged particle flux in about 580 km altitude measured by the *SAAD* (*South Atlantic Anomaly Detector*) aboard the X-ray satellite *ROSAT*. The red region indicates the SAA (South Atlantic Anomaly). The green bands at higher latitudes correspond to an enhanced particle flux near the Earth's auroral zones. (Courtesy of NASA/GSFC; Credit: S. L. Snowden)

layer, e.g. the SiO_2 surface passivation, can induce long lasting charges that distort the electric field in the detector. If positive holes drift to the Si-SiO_2 interface, dangling bonds can form at lattice mismatches or impurities, which increase the surface component of the leakage current. However, the performance loss due to ionization is usually exceeded by defects and vacancies created in the lattice structure of the silicon bulk, which increase the bulk leakage current and induce charge traps (Diebold et al., 2013a). The latter is particularly an issue in front-illuminated (FI) CCDs (Charge-Coupled Devices) that accumulate the charges produced by photon interactions in potential minima close to the detector surface (cf. Fig. 4.3). If charges are trapped during the readout shifting process, the energy of a photon event is underestimated (CTI – charge transfer inefficiency), while the subsequent re-emission might increase the apparent energy of another event. State-of-the-art back-illuminated CCDs are intrinsically more robust against soft proton radiation because the charge is accumulated at the shielded back, where the proton induced trap density is significantly lower (Diebold et al., 2014b).

A well-studied example of this kind of damage is the rapid CTI increase in the FI CCDs of the *ACIS* (*Advanced CCD Imaging Spectrometer*) instrument on the *Chandra X-Ray Observatory* (Weisskopf et al., 2003). The subsequent irradiation of a spare detector lead to the conclusion that orbital protons in the energy range of 100–200 keV have induced the damage (Lo and Srour, 2003). Even though this potential risk was known prior to the launch of *Chandra*, the flux on the detector had been underestimated in simulations due to the incorrect treatment of grazing incidence proton scattering on the X-ray mirror (Dichter and Woolf, 2003). Measurements in the low gain mode of the *EPIC-pn* (*European Photon Imaging Camera*) detector system aboard *XMM-Newton* confirmed this result (Kendziorra et al., 2000).

(a) Proton range in silicon projected on the surface normal

(b) Contribution of ionization (blue) and interaction with nuclei (red) to the total proton stopping power in silicon
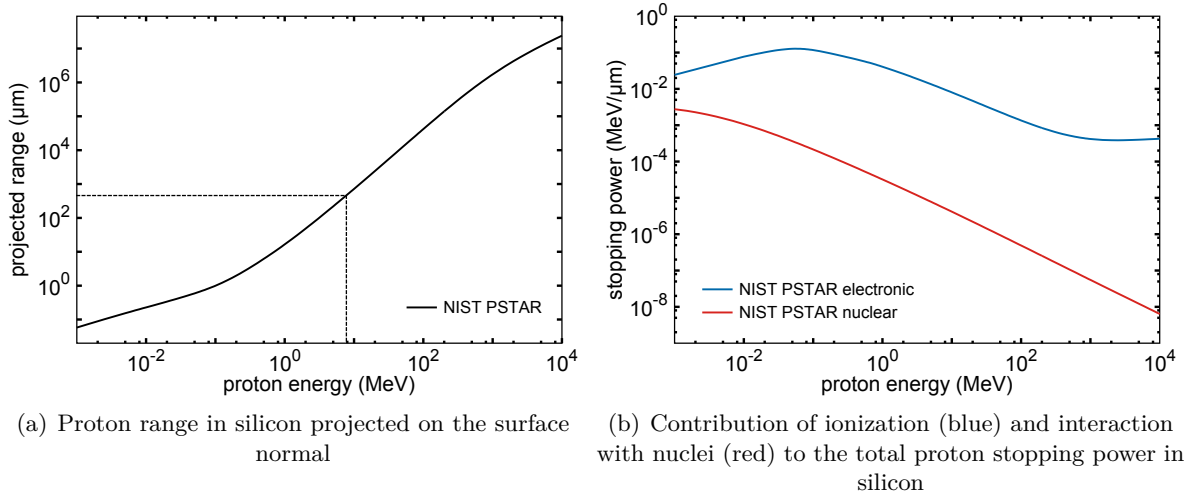
Figure 4.2: Plots of NIST PSTAR (Proton Stopping And Range) data. The left plot shows the range of protons in silicon, projected on the surface normal. The typical thickness of an X-ray detector is around 500 µm, which corresponds to a proton energy of about 8 MeV (indicated by the dashed lines). The plot on the right shows the contribution of ionization (blue) and scattering on nuclei (red) to the total stopping power.

The second effect of protons on X-ray observatories is the generation of instrumental background, either by direct interaction in the sensitive detector volume, eventually after previous energy loss in filters, insensitive sensor top layers, or during scattering, or by the creation of fluorescence lines in the surrounding material of the detector. While soft protons are the paramount contribution to the direct background, protons up to the highest energies mainly create fluorescence background. An accurate modeling of all background contributions is crucial to evaluate the scientific performance, i.e. the signal-to-noise ratio, of an X-ray instrument and thus constraining the detection limit for faint sources. Such studies were performed for instance for the *EPIC* detectors of *XMM-Newton* by using in-orbit data (Lumb et al., 2002; Kuntz and Snowden, 2008) as well as simulations (Tenzer, 2008).

4.2 Soft Proton Irradiation

In the following, the setup for soft proton irradiation as reported in Diebold et al. (2013a) (cf. Sec. 5.2) and Diebold et al. (2014a) (cf. Sec. 5.3) is concisely described and the irradiation campaigns for two future satellite missions are summarized. Even though the second of these missions, which is described in Section 4.2.3, is an Earth observation mission and not related to
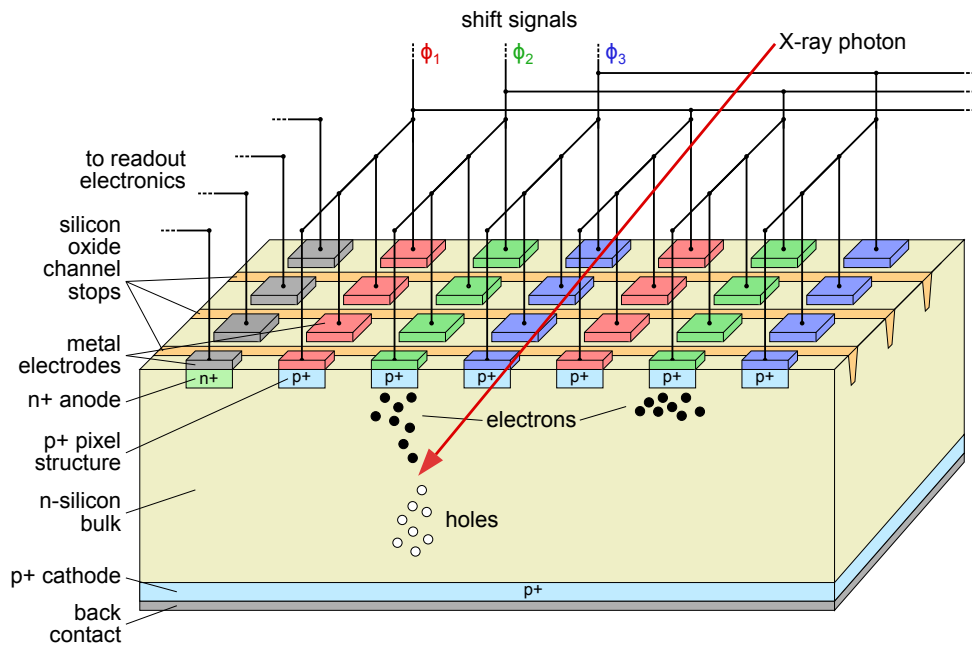
Figure 4.3: Principle of a front-illuminated CCD sensor. Each pixel is formed by three electrodes in a row; SiO_2 channel stops separate the rows. A negative voltage is applied to the back contact to fully deplete the silicon bulk. In acquisition mode the electric potential Φ_2 of the central electrode of a pixel (green) is slightly positive with respect to the adjacent electrodes (red, blue). The electron-hole pairs created by an X-ray photon interacting in the bulk are separated by the electric field and the electrons accumulate below the closest central electrode. During the readout the electrons are shifted sideways via an alternation of the potentials Φ_1, Φ_2, and Φ_3 to the respective anode. In that way, the charge signals of one row are subsequently transferred to the readout electrode.

astronomy, it has been included in this thesis to highlight the possibility for further additional applications of the developed setup.

4.2.1 Experimental Setup

The soft proton irradiation experiment has been set up at the Van de Graaff ion accelerator facility of the Institute for Physics of the University of Tübingen. A schematic diagram of the irradiation setup is presented in Fig. 4.4. Key components are several micrometers thick metal foils that degrade the energy of the proton beam from the accelerator and spatially widen the beam. The latter is crucial for a uniform irradiation of large targets, because even though the beam could also be widened via defocusing with the double quadrupole magnets installed at the beam line, the flux distribution on the irradiation plane would not be reproducible. Up to four
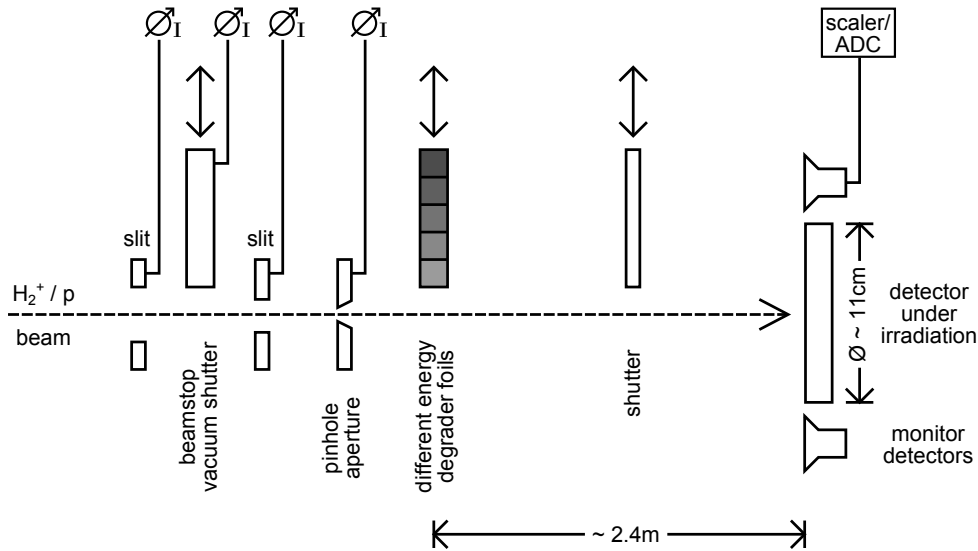
Figure 4.4: Schematic diagram of the irradiation setup. After passing through a pair of slits, a pinhole aperture reduces the beam current and assures a well-defined beam spot on an energy degrader foil. This metal foil with several micrometers thickness degrade and broaden the beam energy and widen the beam spatially. In a chamber at the end of the beam line up to four detectors surround the irradiation target to monitor the flux and the spectrum. (Diebold et al., 2013a)

different foils can be mounted on a linear manipulator, which allows changes without breaking the beam line vacuum and thus enables a quasi-continuous successive irradiation at different energies. The combinations of initial beam energy and foil material and thickness to achieve a required energy and flux distribution have been simulated by means of the TRIM[1] tool (Ziegler et al., 2010). Simulation results for reasonable combinations and a comparison to simulations with the GEANT4[2] toolkit (Agostinelli et al., 2003) as well as to measurements are included in Diebold et al. (2013a). A tail to lower energies in the measured spectra has been attributed to scattering at the inner walls of the beam line and to slit scattering in the pinhole and in the detector apertures. The former fraction could be efficiently reduced by installing two circular apertures downstream of the degrader foil. The issue of slit scattering in small circular apertures is addressed in detail in Diebold et al. (2014a), where Monte Carlo simulations by means of the GEANT4 toolkit to find an optimized aperture design are reported.

Silicon surface barrier (SSB) detectors are placed around the target to monitor the flux and the spectrum before and during irradiation. The flux uniformity has been determined prior to any irradiation by measuring with the SSB detectors at different positions on the target plane. A

---

[1]TRansport of Ions in Matter – `http://srim.org/`
[2]`http://geant4.cern.ch/`

key feature of the setup is a high flux uniformity over a large area. A typical distribution for an energy-foil combination that has been used for a detector irradiation and is presented in Diebold et al. (2013a) shows less than 3% variation over an area of $8 \times 8\,\mathrm{cm}^2$. The independent monitoring system allows early radiation hardness tests of X-ray detector prototypes when readout electronics are not yet available, as well as the irradiation of passive satellite components that are potentially vulnerable to soft proton radiation.

4.2.2 Irradiation of LOFT Detector Prototypes

The *Large Observatory For x-ray Timing*[3] (*LOFT*) (Feroci et al., 2014) was one of five candidates considered for the M3 mission of the Cosmic Vision program of the ESA. The design concept of the satellite is shown in Fig. 4.5. Since it had not been selected as the final M3 mission, it participates again in the competition for the M4 launch opportunity. *LOFT* features two instruments: the *Large Area Detector* (*LAD*) (Zane et al., 2014) with an unprecedented effective area of the order of $10\,\mathrm{m}^2$ at $8\,\mathrm{keV}$ and the *Wide Field Monitor* (*WFM*) (Brandt et al., 2014) which covers simultaneously one third of the sky accessible to the *LAD*. Both instruments will use Silicon Drift Detectors (SDDs) (Rachevski et al., 2014), because these are available with a large geometric area of about $70\,\mathrm{cm}^2$ and offer the unique combination of an excellent spectral resolution below $260\,\mathrm{keV}$ Full-Width at Half Maximum (FWHM), a short collection time of the order of $5\,\mathrm{\mu s}$, and a small area-to-mass ratio of about $1\,\mathrm{kg/m}^2$ (Del Monte et al., 2014a; Kushpil et al., 2006).

The principle of an SDD is shown in Fig. 4.6. A high voltage is applied to the cathodes via a voltage divider to deplete the n-silicon bulk and to generate a drift field with a large gradient of about $350\,\mathrm{kV/cm}$. If an X-ray photon interacts via the photoelectric or the Compton effect in the depleted n-silicon bulk, electron-hole-pairs are generated. The holes drift slowly to the cathodes and are absorbed, whereas the electrons follow the electric field in the silicon bulk to the segmented anodes. The connected readout electronics – charge preamplifier, shaping electronics, and ADCs – determine the total charge as a measure for the deposited photon energy and the charge distribution on the anodes. The latter is used to calculate the position of the X-ray interaction. While centroiding yields the position in the direction along the anodes, the width of the charge distribution is a coarse measure for the distance to the anodes. The accuracy of the latter is depending on the anode pitch, which is $970\,\mathrm{\mu m}$ for the *LAD* and $145\,\mathrm{\mu m}$ for the *WFM* SDDs (Del Monte et al., 2014b). The coded-mask principle of the *WFM* requires a

---

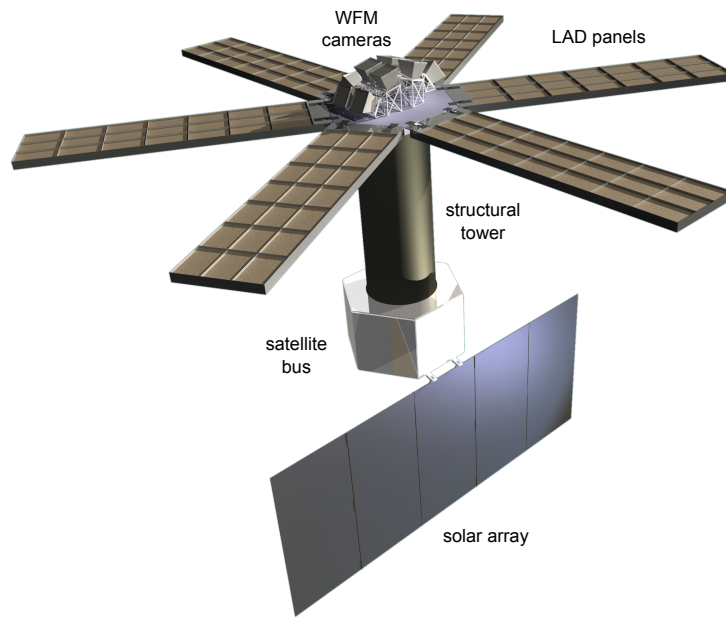[3]`http://www.isdc.unige.ch/loft/`

Figure 4.5: Design concept of the *LOFT* satellite. (Courtesy of the *LOFT* consortium)

two dimensional position resolution, while for collimating instruments such as the *LAD* position sensitivity is in principle not necessary.

The baseline orbit for *LOFT* is an equatorial low Earth orbit with an altitude of 550 km, for which the model of Petrov et al. (2009) for quasi-trapped proton fluxes can be used to estimate the soft proton fluence. Two SDD prototypes have been irradiated at the accelerator facility in Tübingen in two campaigns in 2012. The procedure and the applied energies and fluences of both campaigns are reported in Diebold et al. (2013a). However, a thorough long-term measurement of the radiation effects, particularly the time evolution of the leakage current, and the analysis of the results were not finished at the time of publication. A comprehensive analysis is still in progress and the topic of a forthcoming article. Some results for one of the sensor prototypes were published in Del Monte et al. (2014a) and are reprinted in Fig. 4.7. The measured increase of the leakage current was more than a factor of three smaller than predicted by the empirical formula of Segneri et al. (2009) and the annealing process, which was followed for about 117 days, progressed at a considerably lower rate than predicted by the model of Moll et al. (2002). The reasons for this discrepancies are unresolved up to now; the second irradiated sensor showed a similar result. However, the test results yield the prospect of a tolerable impact of the orbital soft proton radiation on the energy resolution of the *LOFT* silicon sensors during the mission lifetime. In order to mitigate radiation effects, the sensors are operated at a temperature below -10 °C (Del Monte et al., 2014b).
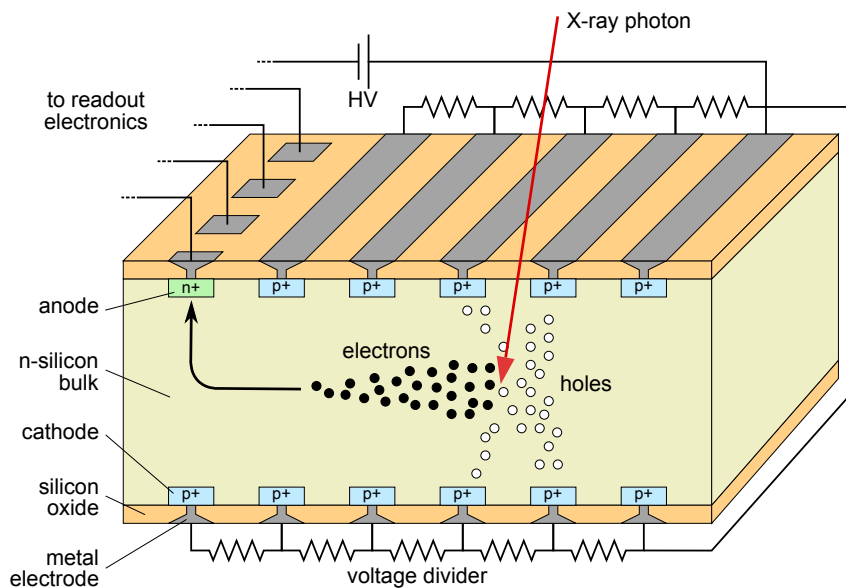
Figure 4.6: Principle of an SDD. A high voltage, applied to the cathodes via a voltage divider, depletes the n-silicon bulk and generates a drift field with a large gradient of about 350 kV/cm. X-ray photons that interact in the depleted region create electron-hole-pairs. While the positive holes are absorbed at the cathodes, the electrons drift in the central bulk region to the anodes at the edge of the sensor, which are connected to the readout electronics.

4.2.3 Irradiation of Coated Optics for ADM-Aeolus

ADM-Aeolus[4] (*Atmospheric Dynamics Mission*) (Stoffelen et al., 2005) is a planned Earth observation satellite within the Living Planet program of the ESA. The launch is currently scheduled for 2015. Fig. 4.8 shows an artist's impression of the satellite in its designated sun-synchronous near-polar orbit with 408 km altitude and an inclination of 97°. The payload is a direct detection Doppler wind lidar (*Aladin – Atmospheric LAser Doppler INstrument*), which will be used to measure wind profiles and to map atmospheric circulations. This instrument comprises a powerful infrared laser, an optical system with non-linear components to shift the wavelength into the near-UV, and a telescope for the detection of the scattered photons.

A critical part of the mission are the windows of the laser system, since these are exposed to high (soft) proton fluxes, particularly during transits of the SAA (cf. Fig. 4.1). In order to assess potential degradations of the optical properties of the fused-silica windows and, in particular, of the high-reflective (HR) and anti-reflective (AR) coatings during the mission time of three years, soft proton irradiations have been performed at the facility in Tübingen in November

---

[4]http://www.esa.int/Our_Activities/Observing_the_Earth/The_Living_Planet_Programme/Earth_ Explorers/ADM-Aeolus

(a) Measured and predicted leakage current

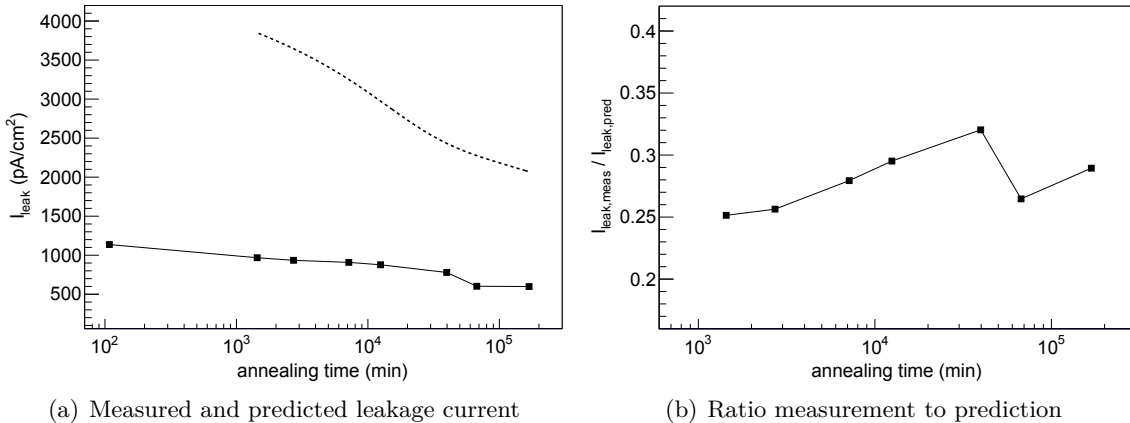(b) Ratio measurement to prediction

Figure 4.7: Time evolution of the leakage current of a *LOFT* SDD prototype after soft proton irradiation. In the left panel the measured leakage currents (data points, connected by straight lines) are compared with the prediction (dashed line) according to the models of Segneri et al. (2009) and Moll et al. (2002). The ratio between the measured data and the prediction is shown in the right plot. (Del Monte et al., 2014a, replotted)

2013. The orbital fluences have been estimated by means of the web-based SPENVIS[5] software package. The nominal and the applied fluences for the chosen proton energies of 150 keV and 1.4 MeV are listed in Tab. 4.1. Three fields of $6 \times 6 \, cm^2$ have been irradiated on an HR and an AR coated window sample with 50.8 mm diameter, respectively. Impressions of the shiftable aluminum aperture to define the fields and a mounted optics sample surrounded by the monitor detectors are presented in Fig. 4.9.

The properties of the irradiated samples have been investigated with laser induced damage (LID) tests at the Institute of Technical Physics of the DLR[6] in Stuttgart. These measurements yielded no significant difference between the irradiated and the shielded areas on both samples. However, since the latency between the irradiation and the LID tests was of the order of several weeks, annealing effects could account for the absence of damages. A second irradiation campaign, at which higher proton fluences are applied and the damage is measured quickly after the irradiation, is under consideration.

---

[5]Space Environment Information System – `https://www.spenvis.oma.be`
[6]German Aerospace Center (German: Deutsches Zentrum für Luft- und Raumfahrt)

Figure 4.8: Artists impression of the *ADM-Aeolus* satellite in orbit. (Courtesy of ESA)

Table 4.1: Nominal and applied soft proton fluences Φ_{nom} and Φ_{app} on HR and AR coated optics samples for the *ADM-Aeolus* mission.

Beam energy (keV)	Φ_{nom} (cm^2)	$\Phi_{\mathrm{app,HR}}$ (cm^2)	$\Phi_{\mathrm{app,AR}}$ (cm^2)
150	$3.4 \cdot 10^{10}$	$3.5 \cdot 10^{10}$	$3.4 \cdot 10^{10}$
150	$1.7 \cdot 10^{11}$	$1.7 \cdot 10^{11}$	$1.7 \cdot 10^{11}$
1400	$7.5 \cdot 10^{8}$	$9.9 \cdot 10^{8}$	$7.4 \cdot 10^{8}$
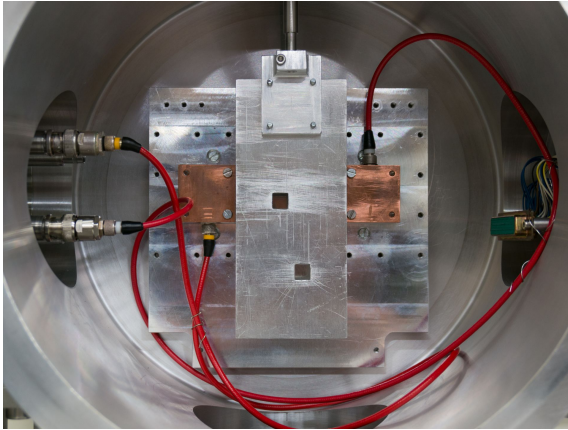
(a) Optics irradiation setup
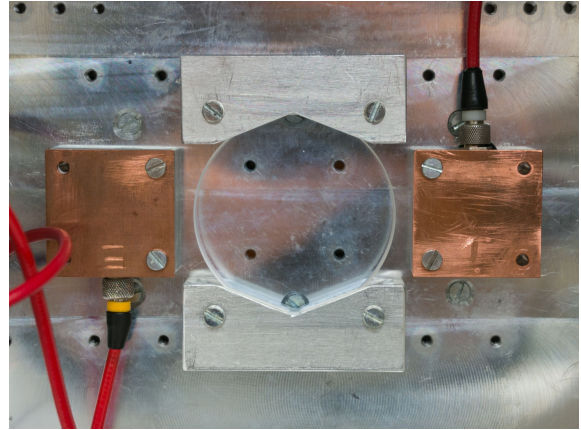
(b) Mounted optics sample

Figure 4.9: Pictures of the irradiation setup for the *ADM-Aeolus* coated optics samples. On the left picture the target chamber with the shiftable aperture to define the square irradiation fields is shown. A mounted sample surrounded by two monitor detectors is visible on the right picture.

4.3 Grazing Angle Soft Proton Scattering on X-Ray Mirrors

In this section, the experimental setup for grazing incidence proton scattering is described and measurements with samples of mirror shells for *eROSITA* are summarized. A brief introduction to the *eROSITA* instrument is included as well as a discussion of the measurement results. Test measurements that have been acquired during the setting up of the experiment are included in Diebold et al. (2014a) (cf. Sec. 5.3), preliminary scattering results have been reported in Diebold et al. (2014b), while a comprehensive description of the experiment along with the results of a full set of measurements can be found in Diebold et al. (2015) (cf. Sec. 5.4).

4.3.1 Focusing X-Ray Optics

The concept of focusing X-rays via two successive grazing incidence reflections goes back to Wolter (1952) and was initially proposed for microscopy. The principle of the Wolter type-I combination of a paraboloid and a hyperboloid mirror, which is usually realized or at least approximated in modern X-ray telescopes, is shown in Fig. 4.10. In order to enlarge the effective area several mirror shells with different diameters and the same focal length are nested in dense assemblies – from four shells of highest quality in the *Chandra X-ray Observatory* optics up to more than 100 in the *NuSTAR* hard X-ray telescope (Madsen et al., 2014). Fig. 4.11 shows a fully assembled X-ray mirror module of the *eROSITA* instrument (cf. Sec. 4.3.3).

As stated in Sec. 4.1, the focusing efficiency of the Wolter-type optics for soft protons was underestimated before the described degradation of the FI CCDs of the *Chandra X-ray Observatory* was discovered. After this discovery but prior to the launch of *XMM-Newton*, grazing incidence soft proton scattering measurements on samples of its mirrors and gratings were performed at the Cambridge Accelerator for Materials Science at the Harvard University. The results were reported in Rasmussen et al. (1999) and compared to GEANT4 simulations in Nartallo et al. (2000). Due to the pressure of time the measurements covered only the small part of the parameter space essential for a rough assessment of the proton flux on the *XMM-Newton* cameras. Therefore, a new experimental setup to extend the energy range and the angular coverage as well as for tests of new mirror materials and coatings was demanded.
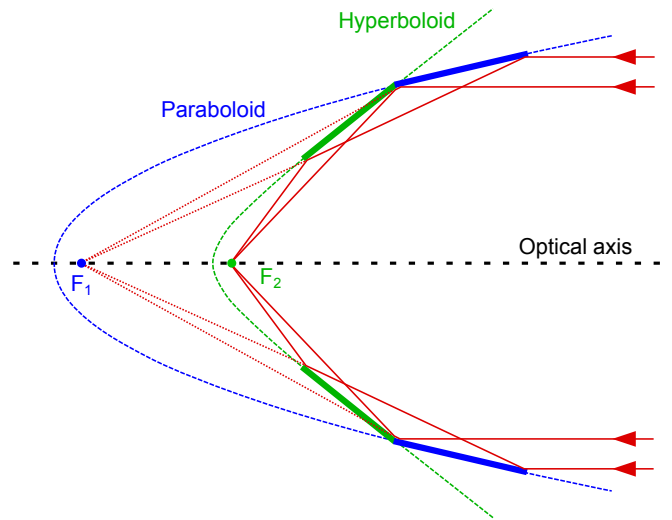
Figure 4.10: Sketch of the course of beam through Wolter type-I optics. The radiation entering from the right (red lines) is reflected twice: first on the parabolic part of the mirror (blue) to the focal point F_1 and secondly at the hyperbolic part (green) to F_2.
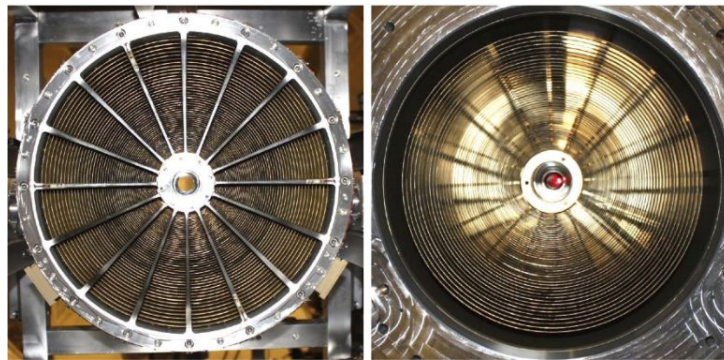

Figure 4.11: Pictures of a fully assembled X-ray mirror module of the *eROSITA* instrument (cf. Sec. 4.3.3). It consists of 54 nested Wolter type-I shells. The left picture shows the paraboloid entrance side; the hyperboloid exit side is displayed on the right. (Burwitz et al., 2014)

4.3.2 Experimental Setup

The soft proton scattering experiment is basically an upgrade of the irradiation setup described in Sec. 4.2. A schematic diagram of the modified setup is presented in Fig. 4.12. Downstream of the pinhole aperture and the degrader foil a collimator has been installed. The apertures are designed according to the optimized design in Diebold et al. (2014a) and have diameters of 1.0 mm at the entrance and 0.3 mm at the exit. The collimator directs a part of the widened beam from the foil on the target that is mounted on a tiltable table. The tilt angle of the target
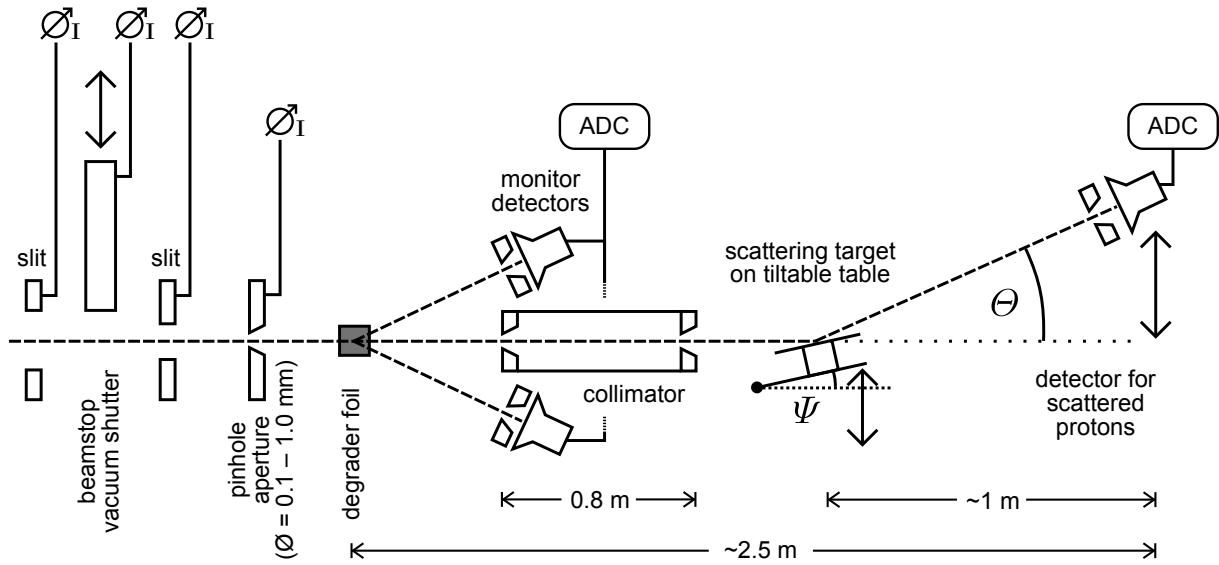
Figure 4.12: Schematic diagram of the grazing angle scattering setup. Two slits are used to verify the alignment of the proton beam with the setup. A pinhole aperture reduces the beam current and ensures a well-defined beam spot on the metal degrader foil. This foil spatially widens the beam to provide flux to the monitor detectors. A collimator focuses a part of the widened beam on the target, which is mounted on a tiltable table to allow a change of the incidence angle Ψ. The scattering angle Θ is defined via the position of the detector at the end of the beam line. (Diebold et al., 2015)

table defines the incidence angle Ψ with a precision of about 0.01°. The scattered protons are measured via a shiftable SSB detector at the end of the beam line. Scattering angles Θ up to 4.5° are currently possible.

The challenge of determining the scattering efficiency, either absolute or relative, is the precise measurement of the proton flux incident on the target. Since inevitable variations of the current and direction of the beam lead to fluctuations of the incident flux, a monitoring system is crucial. The solution has been found in the use of monitor detectors that are mounted peripheral at the collimator entrance, where they are exposed to the widened beam behind the foil. The ratio of flux on the monitor detectors to the flux incident on the target is constant for each combination of beam energy and foil material and thickness. This ratio has been determined for all proton energies that are used by determining the flux at the target with an SSB detector mounted directly at the collimator exit as well as before and after measurements with the shiftable SSB detector at Θ = 0°.

The slits upstream of the setup and all apertures are aligned by means of a theodolite. While Θ can be calculated from the known distance between target and detector and the shift of the
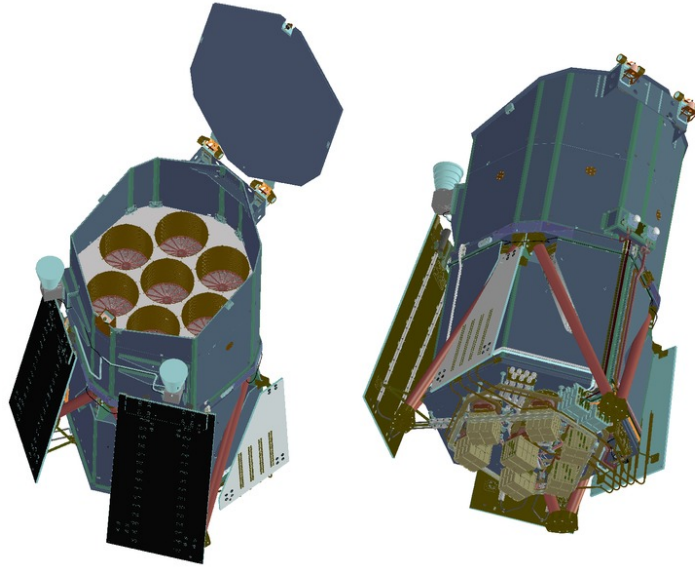
Figure 4.13: Design study of the *eROSITA* instrument for the *SRG* satellite. The top view shows the seven Wolter type-I mirror assemblies below the open lid. The plates on the sides of the instrument are radiators connected to the seven CCD cameras that are visible in the bottom view. (Courtesy of the Max Planck Institute for Extraterrestrial Physics)

detector with respect to the $\Theta = 0°$ position, Ψ is calibrated with a laser that can be inserted in the beam line upstream of the collimator. The laser beam, aligned to the collimator axis, is reflected on the target mirror and the position of the scattered beam is determined with the shiftable SSB detector. The condition for specular reflection $\Psi = \Theta/2$ is used for the calibration. The laser is used as well for the fine adjustment of the orientation of the target mirror and the position of the SSB detector.

4.3.3 eROSITA X-Ray Mirror Targets

eROSITA[7] (extended ROentgen Survey Instrument with a Telescope Array) (Predehl et al., 2014) will be the main instrument of the Russian *SRG* (Spectrum-Roentgen-Gamma) mission which is scheduled for a launch in 2016. The satellite will operate in an orbit around the Lagrangian point L2 of the Earth-Sun-system to perform an all-sky survey in X-rays up to 10 keV. *eROSITA* features seven Wolter type-I telescopes, each consisting of 54 nested mirror shells (cf. Fig. 4.11). Fig. 4.13 gives an impression of the instrument design.

---

[7]`http://www.mpe.mpg.de/eROSITA`

The targets for the scattering measurements reported in Diebold et al. (2015) were two samples of 10 cm and 12 cm length that were cut from an *eROSITA* spare mirror shell. Three proton energies were selected for the measurements to cover the range of interest in which an enhanced scattering efficiency was reported: 250 keV, 500 keV, and 1 MeV. Despite the fact that energies down to a few keV would be of interest, particularly for the analysis of direct proton background in astronomical observations, the currently used SSB detector has a lower threshold of about 100 keV. The sets of measurements cover incidence Ψ angles from 0.3° up to 1.2° and scattering angles Θ in the range of 0.5° to 4.1°. $\Psi < \Theta$ combinations for which the detector is obscured by the mirror were not measured.

4.3.4 Discussion of the Experimental Results

For all measured combinations of proton energy, incidence angle, and scattering angle both the scattering efficiency and the most probable energy loss have been determined. The differential scattering efficiency is given as the ratio of detected protons to the number of incident protons and normalized to the solid angle covered by the detector. This value is independent of the dimensions of the experimental setup and, therefore, suitable for a comparison to other experiments and simulations. Since the beam after the degrader foils is not monoenergetic any more, the most probable energy loss has been determined by fitting incident and scattered spectra with Gaussians and calculating the shift of the peak. All experimental results are plotted in Diebold et al. (2015); examples of the measured scattering efficiencies and the energy loss are presented in Figs. 4.14 and 4.15.

A comparison of the present efficiency results to the data in Rasmussen et al. (1999) obtained with an *XMM-Newton* mirror sample revealed significant discrepancies for the higher energies, at which the present efficiencies are up to a factor of four larger. However, only six data points of the previous measurement are available and have been considered. The discrepancy might – at least partially – be accounted to the different methods to determine the incident flux. In the former setup, the target current was integrated and converted to the number of elementary charges. This number was taken as the number of incident protons, which rises two possible error sources: first, only absorbed protons are counted, which only yields a good approximation if the integral scattering efficiency is large, and second, the impacting beam on the target releases secondary electrons – so-called delta-electrons. While the first issue leads to an overestimation of the scattering efficiency, the increase of the measured current by the second effect yields an apparently lower efficiency. The strengths of both issues depend on the beam energy and could not be measured in the former experiment. Future studies of these issues are planned
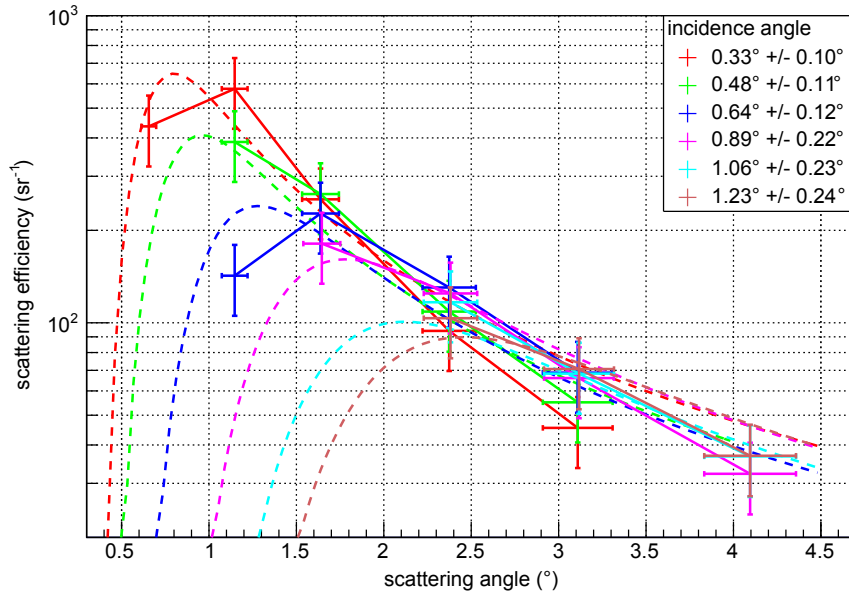
Figure 4.14: Scattering efficiency results for a proton energy of 500 keV. The values are normalized to the solid angle of the detector. The given errors account for counting statistics as well as uncertainties of the solid angle and the incidence and scattering angles. The individual data points for each incidence angle are connected by straight lines. The dashed lines are calculated by means of the Firsov description. (Diebold et al., 2015)

with the present setup. Therefore, the insulation of the target and the installation of a delta-electron repulsion grid are intended. These improvements cannot just be used to determine the strength of the mentioned effects, even more they might allow to estimate the integral scattering efficiency.

Furthermore, the measured data has been compared to TRIM simulations (cf. Fig. 4.16). The simulations give for all parameters lower efficiencies than experimentally measured. While the agreement at larger scattering angles is still reasonable, either within the errors or at most up to 10% off, the deviations towards low scattering angles are increasing and reach up to a magnitude difference. This is pronounced for lower energies and for larger incidence angles. The comparison yields the individual parameter thresholds at which the simulation stops to be reliable. For a further evaluation of the TRIM accuracy, measurements of the off-axis flux are planned, for which at least one additional detector will be mounted laterally offset with respect to the main detector.

The theoretical description of the distribution of scattering angles as function of the incidence angle by Firsov (1967) was proposed as model for proton scattering in X-ray mirrors and implemented in GEANT4 by Lei et al. (2004). The integral scattering efficiency, which is needed to
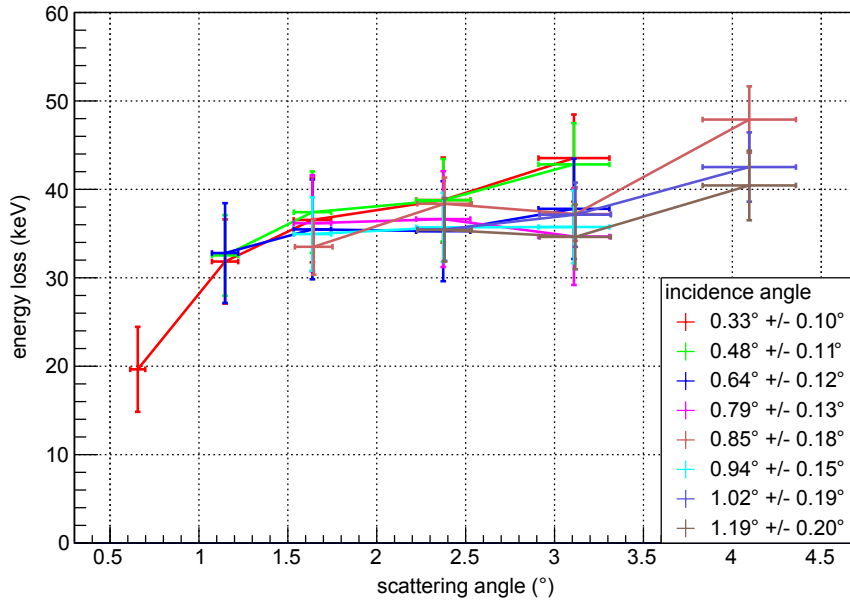
Figure 4.15: Most probable energy loss for a proton energy of 500 keV. The values have been calculated by subtracting the mean energy of the scattered spectra from the incident energy. All these values have been obtained by Gaussian fits to the main peak of the spectra. The individual data points for each incidence angle are connected by straight lines. (Diebold et al., 2015)

calculate the differential efficiency for a certain scattering angle, is not measured in the current experimental setup. Therefore, to allow a comparison, the integral of the theoretical curve for each measured incidence angle was normalized on the integral of the data, which was obtained by linearly interpolating between the data points. As shown in Fig. 4.14, within the errors, the Firsov curves are a good approximation of the data, even though the measured efficiencies decrease slightly steeper towards larger scattering angles.

The scattering description by Firsov uses the model of surface plasmons to derive the angular distribution of ions scattered at glancing angles. The idea for plasmons – quantized "plasma" excitations in a dense electron gas – leads back to Pines and Bohm (1952) and Bohm and Pines (1953). Since the Firsov description does not consider energy loss, independent of the incident energy a narrow Gaussian distributed around 3 keV was assumed in the GEANT4 implementation of Lei et al. (2004). This value originates from the scattering measurements on extensively prepared planar aluminum samples reported in Winter et al. (1997). However, the presently measured data show considerably larger energy losses that increase with the incident energy and the scattering angle (cf. Fig 4.15). The discrepancy could be explained by the different target materials and the different surface conditions.
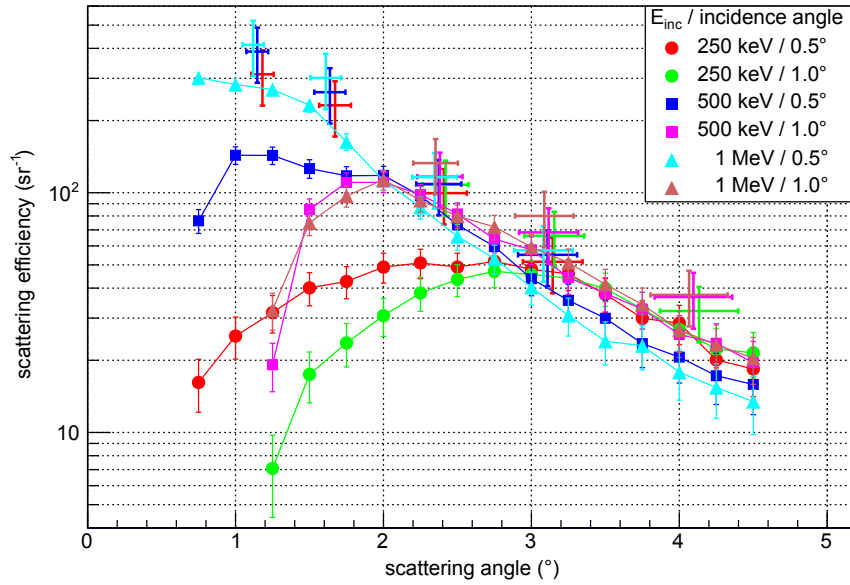
Figure 4.16: Scattering efficiency results of TRIM simulations, each with 10 million protons. Angular cuts and an energy cut below 100 keV have been applied to match the acceptance angle and the energy threshold of the detector in the experimental setup. The individual data points of one parameter set are connected by straight lines. Included are the experimental data points of the measurement sets that correspond best to the parameters of the simulations (drawn in the respective color). (Diebold et al., 2015)

Furthermore, preliminary results reported in Diebold et al. (2014b) that were measured without degrader foil indicated an increase of the scattered spectra just above the detection threshold of 100 keV, but this finding is not significant and may be attributed to electronic noise. Since the current setup cannot be used to study the efficiencies for the generation of direct proton background on CCD detectors, future improvements are under discussion to exchange the SSB detectors for a detection system with a considerably lower threshold, e.g. a CCD, a micro-calorimeter (array), or an electrostatic or magnetic analyzer with a microchannel plate readout.

5 Publications

5.1 UV MCP Detectors for WSO-UV: Cross Strip Anode and Readout Electronics

UV MCP Detectors for WSO-UV:
Cross Strip Anode and Readout Electronics

Sebastian Diebold, Jürgen Barnstedt, Stephan Hermanutz, Christoph Kalkuhl,
Norbert Kappelmann, Marc Pfeifer, Thomas Schanz, Klaus Werner
Institute for Astronomy and Astrophysics
Kepler Center for Astro and Particle Physics
University of Tübingen
72076 Tübingen, Germany
Email: diebold@astro.uni-tuebingen.de

Abstract—The main instrument of the WSO-UV satellite covers the wavelength range of 102 - 176 nm and 174 - 310 nm with two high resolution echelle spectrographs. The essential requirements for the associated detectors are high quantum efficiency, solar blindness, and single photon detection. To achieve this, we are developing microchannel plate (MCP) detectors in sealed tubes. It is planned to use cesium activated gallium nitride as semitransparent photocathode, a stack of two microchannel plates in chevron configuration, and a 33 mm × 44 mm cross strip anode with 64 horizontal and 64 vertical electrodes. This type of anode requires a lower gain of the MCPs ($\approx 10^6$) compared to other types of anodes. Therefore, it extends the expected lifetime of the detectors to about five to ten years.

The challenge for the use of a cross strip anode onboard the WSO-UV satellite is the combination of contradictory constraints on the readout electronics: On the one hand it should be able to handle a maximum count rate of $3 \cdot 10^5 \, \mathrm{s}^{-1}$ with a spatial resolution better than 15 μm. On the other hand the power consumption is limited to about 8 W. One feasible solution is the so-called Beetle chip. This chip provides 128 input channels with charge-sensitive preamplifiers and shapers. It stores the sampled data temporarily in a ring buffer and multiplexes it to four analogue readout channels. The output is then digitized by four ADCs and processed in a radiation hard FPGA, which also contains the space-wire interface to the satellite bus.

I. INTRODUCTION

A. WSO-UV Mission Overview

The World Space Observatory - Ultraviolet (WSO-UV) [1] is an international astronomical observatory, designed to provide future access to the 100 - 300 nm spectral range. The importance of this mission gets obvious, regarding the major impact UV observations have had on modern astronomy together with the fact, that no other UV mission is planned for the near future, i.e. the post-HST era.

WSO-UV is a multinational project under Russian leadership with contributions from Spain and Ukraine. The Institute for Astronomy and Astrophysics of the University of Tübingen (IAAT) will provide detectors for this mission. In combination with Radioastron and SpectrXG it is part of the Russian Spectrum Series. All satellites of this series use the Russian *NAVIGATOR* platform as satellite bus. The launch of WSO-UV is scheduled for 2016 and the minimum mission time is 5 years.

The observing time will be divided into a Core Program (CP), a Funding Bodies Program (FP), and Open Time (OT). The main scientific goals of the CP will be the study of galaxy formation to determine the diffuse baryonic content in the Universe and its chemical evolution, physics of accretion and outflow, and extrasolar planetary atmospheres and astrochemistry in the presence of strong UV radiation fields.

B. Instrumentation on WSO-UV

WSO-UV possesses a 1.7 m Ritchey-Chretien telescope with 17 m focal length and a field of view of 30′. The required pointing stability of about 0.1″ will be achieved with three fine guidance sensors.

The main focus of the mission is on spectroscopy. Therefore, three spectrographs are mounted in the instrument compartment between mirror and satellite bus (cf. Fig. 1): two high-resolution echelle spectrographs (ES) with a resolution $R \approx 50000$, *VUVES* for the VUV band (102 - 176 nm) and *UVES* for the UV band (174 - 310 nm), along with a low-resolution *Long Slit Spectrograph* (*LSS*, $R \approx 1000$, 102 - 310 nm). The echelle spectrographs were developed in a collaboration between IAAT and ISAS Institute for Analytical Science, Berlin, under the name *HIRDES* (cf. Fig. 2) [2]. They are specifically designed to be equipped with microchannel plate (MCP) detectors. In addition to the spectrographs, an imaging instrument, the *Imaging and Slitless Spectroscopy Instrument for Surveys* (*ISSIS*) [3], is placed in the focal plane of the telescope.

II. DETECTORS FOR WSO-UV

Both echelle spectrographs (*VUVES* and *UVES*) utilize two redundant MCP detectors. The LSS is designed for the use of two MCP detectors, one for the VUV and one for the UV wavelength range.

A. Detector Requirements

The size of the echelle spectra at the detector surface is 30 mm in main dispersion direction and 40 mm in cross dispersion direction. Therefore, the active area for a circular detector needs to be 50 mm in diameter. The minimal required spatial resolution is 30 μm in main dispersion direction to
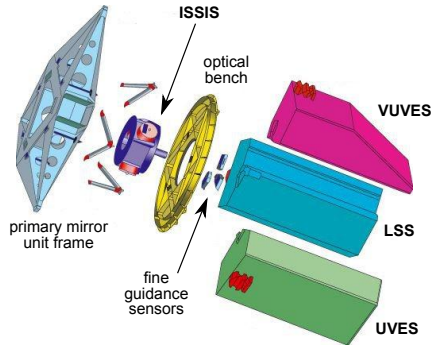
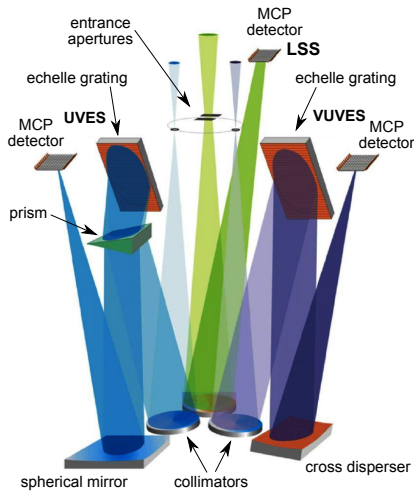Fig. 1. Sketch of the WSO-UV instrument compartment

Fig. 2. Optical layout of the two channels of *HIRDES* and the *LSS*. UV photons enter the instruments through apertures in the focal plane. For the *UVES* an echelle grating is combined with a prism, the *VUVES* uses a combination of an echelle grating and a cross disperser. The *LSS* design shown here is preliminary. All MCP detectors are mounted on the upper side close to the optical bench.

distribute one optical resolution element on three electronic pixels. Nevertheless, the goal is to achieve 15 μm. In this case, the spectral resolution is only limited by the optics. In cross dispersion direction the resolution has to be in the same order of magnitude, but it is less critical.

Both echelle spectrographs are by design very efficient, since they have a minimum number of optical elements and use high reflective coatings. Therefore, the detectors must feature a high quantum efficiency to obtain spectra of faint stars in an acceptable time frame. A critical issue in this context is solar blindness of the detectors, otherwise the background caused by straylight is defining the lower limit of the count rate, and sets a lower threshold for the faintness of possible sources. Furthermore, single photon detection is required to compensate for the jitter of the spacecraft during a long time exposure. A slit monitor records the precise position of the spacecraft. This
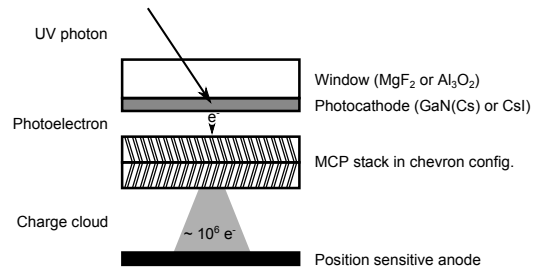

Fig. 3. Principle of a semitransparent UV MCP detector

information combined with a timestamp for each event gives the possibility to rearrange the photons afterwards and correct the blurring effect.

The detectors have to be capable of handling a maximum count rate of $3 \cdot 10^5 \, \mathrm{s}^{-1}$. This requirement rather aims at a short detector dead time, than at observing bright objects which will induce such high rates. A neutral density filter has been foreseen for the observation of bright sources.

There are two additional requirements which come into conflict with the ones named before: a long detector lifetime and a low power dissipation. A lifetime of at least 5 years, more likely 10 years, is necessary for achieving the planned mission lifetime. The degradation rate of MCPs is depending on the extracted charge, and therefore, assuming a constant count rate, on the gain [4], [5]. From this it follows that the detector design has to ensure that the needed gain to achieve the required resolution has to be as low as possible [6].

The power dissipation of a single detector including the front-end electronics is limited to 8 - 10 W. This value arises from the limit which was set on thermal distortions of the spectrograph structure. This constraint makes it difficult to develop front-end electronics for the position sensitive anode we would like to use (cross strip anode, cf. II-B3), which in turn would help to operate the detector with low gain.

B. Detector Concept

To be able to fulfill the previously mentioned requirements, some improvements and further developments of existing UV MCP detectors have to be made. Two photocathode modes are possible for MCP detectors. For the opaque mode the photocathode is deposited on the upper side of the first MCP. Detectors of this type are referred to as open face detectors because they have no entrance window. MCP detectors in which the photocathode is coated on the inner side of a UV transparent window (so-called semitransparent mode) are sealed tube detectors. The functional principle of this kind of detectors is illustrated in Fig. 3. A cross-sectional view of our detector design is presented in Fig. 4.

1) Photocathode: To achieve a high quantum efficiency, the proper material and a high quality of the photocathode are crucial. As gallium nitride (GaN) seems to be very promising for this application [7], we develop in collaboration with the Karlsruhe Institute of Technology (KIT) a semitransparent
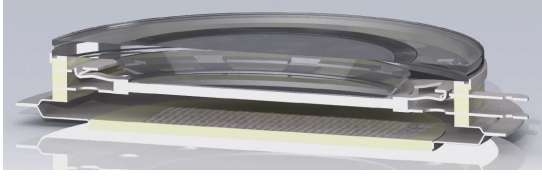
Fig. 4. CAD drawing of our detector design in cross-sectional view. The tube diameter is about 8 cm with a diameter of the active area of 5 cm. The gap between photocathode and MCP stack is minimized to a few hundred micrometers and the distance between MCP stack and anode is less than 1 cm. Two MCPs with a thickness of about half a millimeter are placed directly on top of each other.
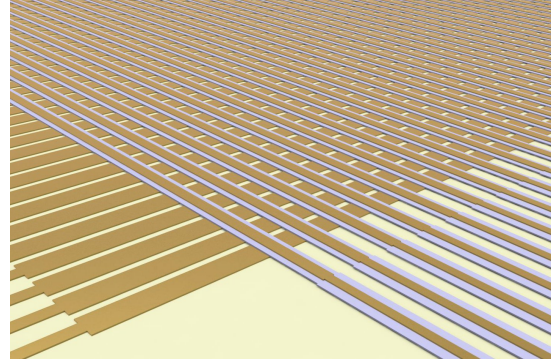

Fig. 5. CAD drawing of the XS anode. The electrodes of the bottom layer are about twice as wide as the ones on top to get approximately the same uncovered surface. The top and bottom electrodes are seperated by an insulating layer.

cesium activated GaN photocathode. For the UV band detector a thin layer of poly-crystaline GaN will be coated on a quartz or sapphire window. We study the possibility of using the same type of GaN photocathode for the vacuum-UV wavelength range, too. In this case a magnesium diflouride substrate is necessary because this material is transparent down to about 110 nm. Therefore, the lower wavelength limit would be increased by some nanometers but the gain in quantum efficiency and the advantage of having just one detector design compensate for this disadvantage. Another option which would cover the whole VUV band is to coat cesium iodide in opaque mode directly on the first MCP. This is not possible for GaN because the growing temperature for this material ($> 350\,^\circ$C) exceeds the maximum temperature MCPs can tolerate.

First GaN samples have been produced in Karlsruhe, successfully transported under high vacuum conditions to Tübingen, and activated with cesium [8]. Currently our collaboration partners in Karlsruhe work on an improved doping of the samples, while we build a setup to measure the quantum efficiency (QE) and compare it to a calibrated NIST photodiode to get the absolute QE.

2) MCPs: Photoelectrons from the photocathode are accelerated by a high voltage towards the MCP stack. Across the MCPs, porous glass plates with microscopic channels and a high resistive surface, a voltage of about 1 kV per MCP is applied. When an electron impinges on a channel wall it creates secondary electrons that are again accelerated. In this way a charge avalanche forms. Our detectors will have a chevron stack of two MCPs with an active diameter of 50 mm. The gain of the MCPs is adjustable via the applied high voltage. We aim at reducing it as much as possible without degrading the spatial resolution.

3) Anode: The use of a cross strip (XS) anode [9] is planned for the detection of the charge cloud from the MCPs. This type of anode reduces the required gain compared to formerly used wedge-and-strip anodes, resistive anodes, and delay-line anodes [10]. The size of the XS anode will be 33 mm by 44 mm. This is slightly larger than the echelle spectrum to avoid edge effects. On this rectangular area a grid of 64 horizontal and 64 vertical electrodes is arranged, all isolated and with about equal uncovered surface (cf. Fig. 5). The manufacturing of the XS anode is done in an industrial process similar to the production of hybrid circuit boards

printed on ceramics. There will be a gap between the MCP stack and the XS anode to allow the charge cloud to spread. This is crucial for the use of this type of anode, as a calculation of the charge cloud center is only possible if the charge is distributed in each direction on three or more strips. The goal is to achieve a subsampling factor of 32. In this case the resolution would be 2048 by 2048 pixels, which corresponds to a pixel size of about 15 μm by 20 μm.

The challenge for the use of a XS anode is the fact, that 128 charge preamplifiers, shapers, and ADCs are needed for the readout. This is not possible on a satellite. The required space would be large, the power consumption and dissipation would exceed the requirements, and a system with this level of complexity is fault-prone. Additionaly the resolution would depend strongly on the precise equalization of all channels. To solve all these problems we study the use of a 128 channel preamplifier ASIC, the Beetle chip.

III. BEETLE CHIP

The Beetle chip was developed by the Max-Planck-Institute for Nuclear Physics in Heidelberg as a multi-purpose readout chip for the LHCb experiment at CERN, Geneva [11], [12]. This chip is not yet space qualified but it has been sucessfully tested for radiation hardness up to 130 Mrad total dose.

A. Functionality and Performance

The chip has 128 input channels, each equipped with a charge sensitive preamplifier and a pulse shaper (CR-RC). After this first stage the pulses are sampled and temporarily stored in an analogue pipeline which acts as a ring buffer. This pipeline is implemented as a switched capacitor array with 187 storage cells. The nominal sampling rate is equal to the clock rate of the chip. The nominal operating clock frequency of the Beetle is 40 MHz but it was successfully tested for stable operation in the range 20 - 100 MHz.

Two modes are possible to trigger a readout, internal or external. To provide the possibility of internal triggering the

Beetle chip has a comparator stage in between the shaper and the pipeline.

To reduce the complexity and the number of ADCs, the Beetle chip multiplexes 32, 64, or all 128 channels on one output channel. This is done by serializing the analogue data. For the readout of the XS anode the 32 to 1 mode will be used. The readout time is 900 ns for an operating frequency of 40 MHz. This time includes a 100 ns analogue header which contains operational parameters of the chip. In this configuration four ADCs are sufficient to digitize the differential current signal output.

The peaking time of the Beetle chip can be adjusted in some range and is also depending on the input capacitance C_{inp}. Using the nominal front-end settings the minimal peaking time is 21.0 ± 0.5 ns with a rise time of 12.5 ± 0.3 ns for $C_{inp} = 3.0$ pF. Values for higher input capacitances and the pulse shapes of the Beetle front-end can be found in [12]. The equivalent noise charge is approximately $550\,e^- + 50\,e^-/\text{pF} \cdot C_{inp}$.

The power consumption of the Beetle chip is 5.21 ± 0.04 mW/ch at a clock rate of 40 MHz and without using the internal trigger. Therefore, the total power dissipation falls short of 0.7 W. Combined with the possibility of using only four ADCs this leads to an economic readout with low power dissipation. In addition we study the possibility for our application to run the Beetle chip with a lower than the nominal clock rate.

The chip has a small digital part which holds a bidirectional I²C-interface. This interface is used to set the control registers of the chip and read operation parameters.

B. Detector Readout Scheme

In Fig. 6 a process chart of the detector readout scheme is shown. The Beetle continuously samples the values at the 128 inputs and holds them temporarily in the storage pipeline. A readout will be triggered internally or, more likely, externally by monitoring the current at the output of the high voltage supply. When a photoelectron is multiplied by the MCPs, the output current increases. After a trigger occurred five samples before and five samples after the event are output and digitized by four low power ADCs.

The digital data are processed in a radiation hard FPGA. Its main task is to calculate the x- and y-position of the center of the charge cloud, attach the total charge of the event and a timestamp. After the calculation, these four values per event are sent to the Instrument Control Unit via a space-wire interface. The FPGA also controls the Beetle chip via I²C.

C. Laboratory Tests

To test the applicability of the Beetle chip for our detector front-end electronics we got several chip samples, one of them on a so-called Beetle daughter board. This board, which was also developed and built by the MPI for Nuclear Physics, Heidelberg, can hold two Beetle chips. It provides a fan-in to bond and connect up to 12 input channels.
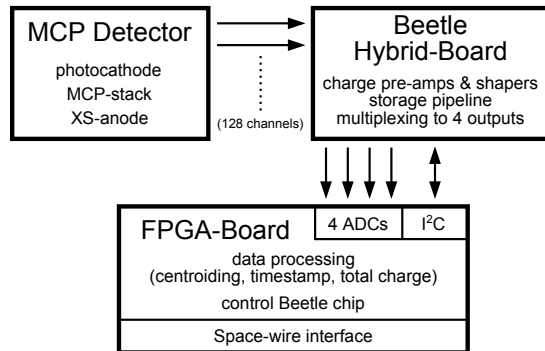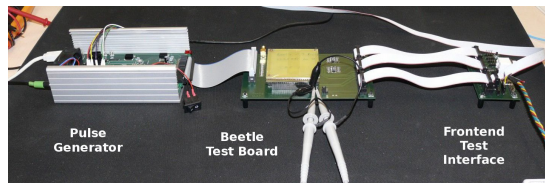

Fig. 6.   Detector readout scheme

Fig. 7.   Pulser test setup

We developed a simple mother board on which the daughter board can be stacked and connected to a pulse generator. This pulse generator, based on a FPGA and controlled via USB from a PC, was specifically designed for testing the Beetle chip. It simulates the signals we expect from the XS anode. This test setup (cf. Fig. 7) gave us the possibility to study the behaviour of the chip, e.g. systematic offsets and gain differences of different channels. Analog output signals from the Beetle output channels 1 and 4 are shown in Fig. 8 (input channels 1 to 32, signal on 18 and 20) and Fig. 9 (input channels 97 to 128, signal on 119 and 127). The Beetle was operated with 20 MHz for this measurement. One can clearly see the fixed offset pattern on channel 4 that is not present on channel 1. This is characteristic for the Beetle version 1.3. A migration to chip version 1.5, in which this effect is minimized, is planned for the near future. Up to now all measurements show good agreement with the chip specifications and give us confidence that the Beetle chip can be used for the readout of a XS anode.

Currently we set up a vacuum chamber for the scrubbing and burn-in of MCPs (cf. Fig. 10). For the burn-in procedure a special electron generator MCP (EGP) is used. This EGP provides a homogeneous electron current when high voltage is applied. To check the MCPs between burn-in steps a mechanism tilts the EGP so that the MCPs can be illuminated through a quartz window. In this configuration the setup can be used to test the XS anode together with the front-end electronics under realistic conditions. A mask with tiny structures placed in front of the MCPs will give us the possibility to check the spatial resolution of the system.
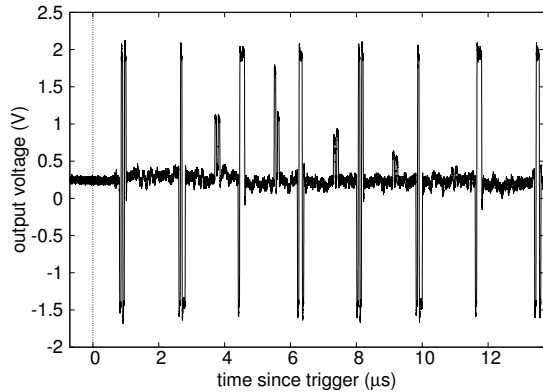
Fig. 8. Output channel 1 (input channels 1 to 32) of the Beetle chip. Input from the pulser on channels 18 and 20. The frequent large pulses mark the beginning of a readout cycle, in which one storage cell of each of the 32 channels is output. Beetle clock frequency was 20 MHz, therefore a readout cycle takes 1.8 μs.
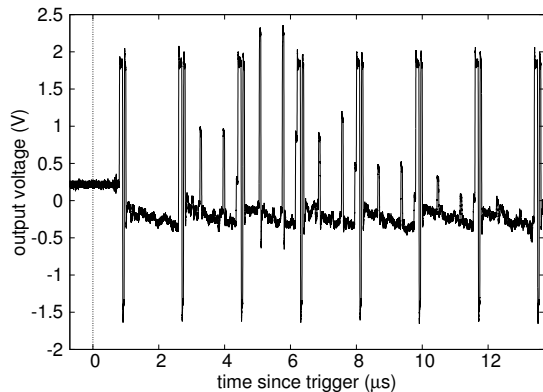

Fig. 9. Output channel 4 (input channels 97 to 128) of the Beetle chip. Input from the pulser on channels 119 and 127. Parameters are the same as in Fig. 8. The fixed offset pattern on this output channel is characteristic for the Beetle version 1.3. For the final readout version 1.5 will be used.

IV. Conclusion

Up to now all our measurements in combination with the published data of the Beetle chip are promising for its applicability in the front-end electronics for the readout of the XS anode of our UV MCP detectors. The next step is to test the chip in a simplified version of the front-end electronics in our MCP test setup with a wedge-and-strip-anode (WSA). As soon as we have a XS anode available, we will proceed this study with an advanced version of the front-end electronics. This will give us then a reliable value of the spatial resolution we can achieve with our detector and electronics design.
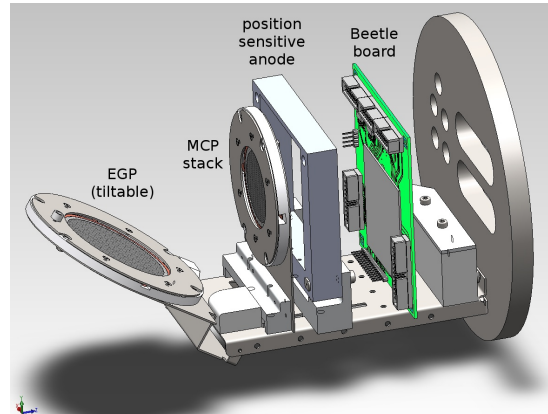
Acknowledgment

Fig. 10. CAD drawing of the MCP burn-in setup. This setup provides the possibility to test the XS anode together with the front-end electronics.

References

[1] K. Werner, B. Shustov, M. Sachkov, A. I. Gómez de Castro, M. Huang, N. Kappelmann, G. Zhao, *WSO-UV - Ultraviolet Mission for the Next Decade* AIP Conference Proceedings, Volume 1135, pp. 314-317, 2009.

[2] K. Werner, J. Barnstedt, W. Gringel, N. Kappelmann, H. Becker-Roß, S. Florek, R. Graue, D. Kampf, A. Reutlinger, C. Neumann, B. Shustov, A. Moisheev, E. Skripunov, *HIRDES - The High-Resolution Double-Echelle Spectrograph for the World Space Observatory Ultraviolet (WSO/UV)* Adv. in Space Research, Volume 41, pp. 1992-1997, 2008.

[3] M. Sachkov, *UV observations of sdB stars and prospects of WSO-UV mission for such studies* Astrophys. Space Sci., Vol. 329, pp. 261-266, 2010.

[4] G. W. Fraser, *X-Ray Detectors in Astronomy* Cambridge University Press, Cambridge, 1989.

[5] D. J. Sahnow, C. Oliveira, A. Aloisi, P. E. Hodge, D. Massa, R. Osten, C. Proffitt, A. Bostroem, J. B. McPhate, S. Bélande, S. N. Osterman, S. V. Penton *Gain sag in the FUV detector of the Cosmic Origins Spectrograph* Proc. of SPIE, Vol. 8145, 2011.

[6] O. Siegmund, A. Tremsin, J. Vallerga, J. McPhate, *Microchannel plate cross-strip detectors with high spatial and temporal resolution* Nucl. Instr. Meth. A, Vol. 610, pp. 118-122, 2009.

[7] O. H. W. Siegmund, A. S. Tremsin, J. V. Vallerga, J. B. McPhate, J. S. Hull, J. Malloy, A. M. Dabrian, *Gallium Nitride Photocathode Development for Imaging Detectors* Proc. of SPIE, Vol. 7021, 2008.

[8] S. Diebold, J. Barnstedt, H.-R. Elsener, P. Ganz, S. Hermanutz, C. Kalkuhl, N. Kappelmann, M. Pfeifer, D. Schaadt, T. Schanz, O. Tanirah, K. Werner, *MCP detector development for WSO-UV* Proc. of SPIE, Vol. 8443, 2012.

[9] A. S. Tremsin, O. H. W. Siegmund, J. V. Vallerga, J. S. Hull, R. Abaid, *Cross-Strip Readouts for Photon Counting Detectors With High Spatial and Temporal Resolution* IEEE TNS, Vol. 51, No. 4, pp. 1707-1711, 2004.

[10] Oswald H. W. Siegmund, Anton S. Tremsin, John V. Vallerga, Jeffrey S. Hull, *Cross Strip Imaging Anodes for Microchannel Plate Detectors* IEEE TNS, Vol. 48, No. 3, pp. 430-434, 2001.

[11] S. Löchner, M. Schmelling, *The Beetle Reference Manual - chip version 1.3, 1.4 and 1.5* - Max-Planck-Institute for Nuclear Physics, Heidelberg, Germany, 2006.

[12] S. Löchner, *Development, Optimisation and Characterisation of a Radiation Hard Mixed-Signal Readout Chip for LHCb* Dissertation, Ruperto-Carola University of Heidelberg, Germany, 2006.

5.2 A setup for soft proton irradiation of X-ray detectors for future astronomical space missions

A setup for soft proton irradiation of X-ray detectors for future astronomical space missions

Sebastian Diebold [a,*], Philipp Azzarello [b], Ettore Del Monte [c], Marco Feroci [c], Josef Jochum [a],
Eckhard Kendziorra [a], Emanuele Perinati [a], Alexandre Rachevski [d], Andrea Santangelo [a],
Christoph Tenzer [a], Andrea Vacchi [d], Gianluigi Zampa [d], Nicola Zampa [d]

[a] Kepler Center for Astro and Particle Physics, Universität Tübingen, Sand 1, 72076 Tübingen, Germany
[b] ISDC Data Centre for Astrophysics, University of Geneva, Switzerland
[c] INAF/IASF Istituto di Astrofisica Spaziale e Fisica Cosmica, Rome, Italy
[d] INFN Istituto Nazionale di Fisica Nucleare, Sezione di Trieste, Italy

ARTICLE INFO

ABSTRACT

Protons that are trapped in the Earth's magnetic field are one of the main threats to astronomical X-ray observatories. Soft protons, in the range from tens of keV up to a few MeV, impinging on silicon X-ray detectors can lead to a significant degradation of the detector performance. Especially in low earth orbits an enhancement of the soft proton flux has been found. A setup to irradiate detectors with soft protons has been constructed at the Van-de-Graaff accelerator of the Physikalisches Institut of the University of Tübingen. Key advantages are a high flux uniformity over a large area, to enable irradiations of large detectors, and a monitoring system for the applied fluence, the beam uniformity, and the spectrum, that allows testing of detector prototypes in early development phases, when readout electronics are not yet available.

Two irradiation campaigns have been performed so far with this setup. The irradiated detectors are silicon drift detectors, designated for the use on-board the *LOFT* space mission.

This paper gives a description of the experimental setup and the associated monitoring system.

1. Introduction

Protons impinging on solid-state detectors on-board astronomical X-ray observatories pose a severe threat and can degrade the X-ray detection performance or even lead to a detector failure [1]. Soft protons in the energy range 0.1–1 MeV are stopped near the detector surface, where they produce ionization, and, in particular, displacement damage. They are potentially more harmful than energetic particles, which are not stopped inside the detector, because the deposited energy is larger, and the radiation effects are concentrated in a small volume around the stopping point.

Ionization near the detector surface generates electron–hole-pairs in the field oxide (SiO_2). Some of the holes drift towards the SiO_2/Si interface, where they create silicon dangling bonds. This leads to an increase of the surface component of the leakage current, whereas lattice defects increase the bulk leakage current. Consequences are a degradation of the energy resolution, and an enlarged charge transfer inefficiency (CTI) in front-illuminated CCDs (charge coupled devices). One well-studied example is the sudden increase in the CTI of the *Chandra ACIS* front-illuminated CCDs during the first month of operation [2].

High proton fluxes occur during the passage through the Van Allen radiation belts and in near-equatorial low earth orbits, where protons are trapped in the geomagnetic field. X-ray detectors can easily be reached by soft protons through collimator holes and the openings of coded-masks. In X-ray observatories that use Wolter type optics, soft protons are funneled through the X-ray mirror shells and focused onto the detectors in the focal plane [1,3].

To study the effect of soft proton radiation on a particular detector, and to estimate the performance degradation during the mission, irradiation setups at accelerator facilities are necessary. The usual procedure is the evaluation of the total ionizing dose (TID) and the non-ionizing energy loss (NIEL) that will occur during the mission, e.g. by performing a Monte Carlo simulation with the expected orbital fluence and spectral distribution. TID and NIEL are then reproduced in the laboratory with one or two proton energies and the representative fluence. An experimentally more complicated but physically straightforward approach is an irradiation with a reproduction of the orbit spectrum by composing it successively from several Gaussian spectra.

* Corresponding author. Tel.: +49 7071 29 78609; fax: +49 7071 29 3458.
E-mail address: diebold@astro.uni-tuebingen.de (S. Diebold).

Both procedures are possible with the setup presented in this paper, even though the composition of the orbit spectrum could be problematic for high fluences due to annealing of the damages during the irradiation. Annealing is a thermal rearrangement process of lattice atoms, and can restore the detector performance up to the initial values. Since radiation damages anneal much faster at room temperature than at the typical operating temperatures of X-ray detectors (~ -20 °C), this effect has to be considered.

In this contribution we discuss a setup for the irradiation of X-ray detectors with soft protons that has been constructed at the Van-de-Graaff accelerator facility of the Physikalisches Institut of the University of Tübingen. In particular, this setup is designed to reproduce the soft proton spectrum below 1 MeV in low earth orbits (cf. Section 2). Section 3 briefly introduces the accelerator facility and gives a description of the experimental setup. Details of the monitoring system are presented in Section 4. Up to now, the setup has been used in two irradiation campaigns to test the changes in the surface leakage current of a prototype of the silicon drift detector (SDD) for the *LOFT* (Large Observatory For x-ray Timing) [4] space mission (cf. Section 5).

2. Soft proton flux in low earth orbit

A flux enhancement of soft protons has been found in the near-equatorial region at altitudes up to $\sim$1300 km. These soft protons could evolve via a double charge-exchange mechanism from the interaction of energetic protons with neutral atoms in the upper atmosphere (thermo- or exosphere) [5]. A number of consistent measurements of this phenomenon show proton energies from $\sim$10 keV to several MeV (cf. Fig. 1). A combined analysis of these measurements is described in [6]. It is proposed that two parameter sets, for quiet and disturbed conditions of the geomagnetic field, fit the experimental data best. The reported flux has been used to determine the dimensions of the irradiation setup, so that the fluence for a typical five year space mission can be applied in a reasonable time between some minutes and a few hours.
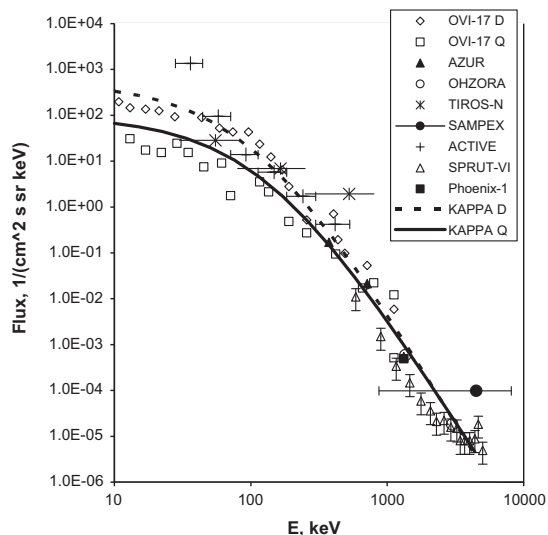
Fig. 1. The energy spectrum of protons in the near-equatorial region according to the data of several experiments [6]. The measured spectrum was fitted using parameter sets for periods of quiet (solid line) and disturbed (dashed line) geomagnetic activity.

3. Irradiation setup

3.1. Accelerator facility

The irradiation setup has been constructed at the accelerator facility of the Physikalisches Institut of the University of Tübingen. The accelerator is a single ended 3 MV Van de Graaff (HVEC Model KN), that can provide light ion beams with energies ranging from $\sim$700 keV to currently 2.4 MeV. The reduced upper limit, compared to the design voltage, is due to an insufficient portion of sulfur hexafluoride (SF_6) in the protective gas, resulting in a lowered dielectric strength. It is planned for the near future to increase the portion of SF_6, so that 3 MeV can be reached. The lower limit of the beam current is of the order of a microampere.

The terminal voltage is measured with a generating voltmeter [7]. The calibration of this voltmeter has been confirmed by measuring the γ rate of the reaction $^{27}Al(p,\gamma)^{28}Si$, which has a sharp resonance in the cross-section at 992 keV, with a NaI(Tl) detector [8].

Four different gases are available for the ion source: hydrogen, deuterium, helium, and ^{13}C-enriched CO_2. The radio-frequency plasma source ionizes the selected gas only to the charge state 1+. If hydrogen is ionized, an equilibrium between protons and H_2^+ arises. An analyzing magnet with a deflection angle of 95° allows to select the desired ions. By splitting H_2^+ with a thin foil or on the target, protons with half the nominal energy are obtained [9] (the same applies for deuterium). As H_2^+ and deuterons have the same charge-to-mass ratio, a momentum separation in the analyzing magnet is not possible, and therefore, the molecular hydrogen beam is contaminated with $\sim$1% deuterons. For this reason, the use of a proton beam is favored and metal energy degrader foils are used to lower the proton energy appropriately.

Several combinations of rotary vane pumps and turbomolecular pumps are distributed along the beam line to reach a pressure in the 10^{-6} mbar regime. This low pressure is especially necessary to avoid coating of the degrader foils with carbon during long duration irradiations, as the residual gas contains a certain amount of hydrocarbons. These molecules are cracked by the proton beam and free carbon is produced, that is then deposited on all surfaces, including the metal foils. Although the growth rate is small, the carbon layer alters the transmission properties of the foil and should be avoided. A beam stopper and a vacuum shutter in front of the foils give access to the experimental setup without venting the whole beam line, which would require a shut down of the accelerator. It takes about 1 h to re-establish the vacuum in the experimental setup.

3.2. Experimental setup

The facility possesses six beam lines; number 3 is currently used for the irradiation setup. The beam line, including the position and opening of the slits and the position of the detector chamber, has been aligned with a theodolite. The beam can be bent and shifted in parallel with various dipole magnets and focused with two double quadrupoles.

A schematic of the irradiation setup is presented in Fig. 2, and the actual implementation at the accelerator facility is shown in Fig. 3. First of all, the incoming proton beam passes through two slits. These slits are rectangular apertures, consisting of four isolated parts. From each of these parts a current signal can be tapped, which is used to align the beam position by comparing the signals from opposite slit parts. A straight beam in the center of the beam line is obtained if all opposite currents of the two slits are equal. The openings have been adjusted to $\sim 4 \times 4$ mm^2 (first slit) and $\sim 3 \times 3$ mm^2 (second slit).
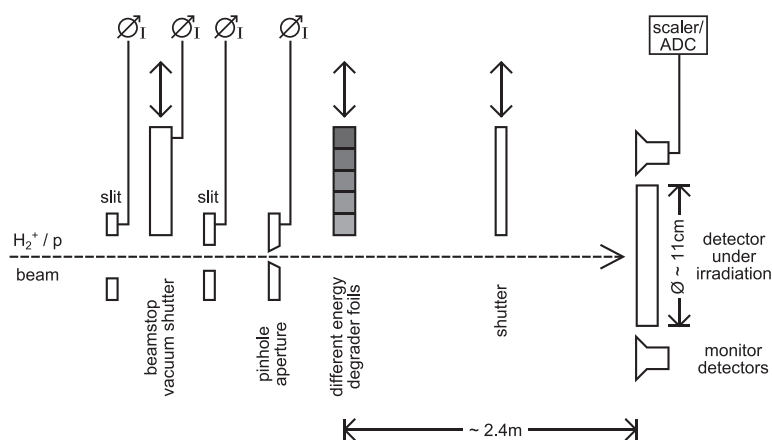
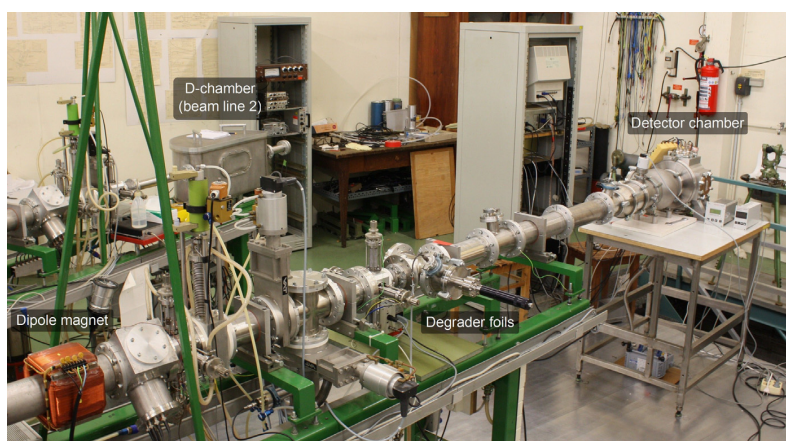**Fig. 2.** Schematic of the irradiation setup.

Fig. 3. Picture of the irradiation setup. The beam is coming in from the left where the last dipole magnet is visible. The black bar in the center is the linear manipulator on which the holder for the degrader foils is mounted. The detector chamber is located 2.4 m downstream of the degrader foils, on the far right of the picture. The D-shaped chamber in the background (beam line 2) has been used for calibrating the monitor detectors and for measuring foil thicknesses.

A pinhole aperture with a circular opening assures a well defined beam spot on the degrader foil, and further reduces the beam current. Tests have shown that for low fluxes (10^3–5×10^5 cm^{-2} s^{-1}) an aperture with 0.1 mm is suitable. If fluxes of more than ~5×10^5 cm^{-2} s^{-1} are required, the diameter must be enlarged accordingly. The aperture is made of copper, isolated from the beam line, and electrically connected to a vacuum feed-through, so that the current on the aperture can be monitored. The pinhole has a 45°-chamfer on the downstream (detector chamber) side to minimize the probability of small angle scattering inside the aperture, which would introduce a beam component with lower energy.

3.3. Degrader foils

Thin metal foils with some micrometer thickness degrade and broaden the beam energy and widen the beam spatially. The energetic and spatial broadening is due to straggling. Four different foils can be fixed on a holder. The holder itself is mounted on a linear manipulator to allow a quick change of the foil without breaking the vacuum, e.g. for an irradiation with different energies, or to compose a spectrum similar to the in-orbit spectrum.

For the selection of foil material, foil thickness, and beam energy to obtain a certain proton spectrum and spatial distribution, simulations with the TRIM[1] Monte Carlo code (part of the SRIM[2] package [10]) have been carried out. The TRIM output lists energy and exit angle with respect to the foil normal for each transmitted proton. A software toolchain for the analysis of the simulations has been implemented. Since only protons with an exit angle of ≤1.8° can directly reach the detector chamber, an angular cut is applied to the simulation data. Without this cut the spectra are shifted to lower energies because of the contribution of protons which have been undergoing a larger energy transfer. The distribution of exit angles is used to estimate the flux uniformity in the detector chamber. As a consistency check, some of the foil–beam energy combinations have been simulated also by means of the Geant4 framework [11], using the Livermore low energy electromagnetic physics list. The deviation in the mean energy is for most parameter combinations within 10% of the TRIM output, and therefore within the expected accuracy. An interesting finding is that Geant4 systematically produces a lower mean energy and a

---

[1] Transport and Range of Ions in Matter.
[2] Stopping and Range of Ions in Matter.

Table 1
Selection of typical simulation results for energy degrader foils, obtained with TRIM and Geant4. The values for mean energy and FWHM are derived from fitting the simulated spectra with Gaussian distributions.

E_{beam} (keV)	Foil	$E_{mean,TRIM}$ (keV)	$E_{FWHM,TRIM}$ (keV)	$E_{mean,Geant4}$ (keV)	$E_{FWHM,Geant4}$ (keV)
1010	6 µm Cu	208	71	181	89
2300	18 µm Cu	820	115	781	130
1010	12 µm Al	308	54	290	68
1010	14 µm Al	120	75	116	111

broader spectrum than TRIM, but both values lie within systematic uncertainties of the detector calibration and foil thickness. A selection of these simulation results is presented in Table 1. A typical spectrum and angular distribution simulated with TRIM is shown in Fig. 4.

If the mean energy of the transmitted protons is larger than ~100 keV, the spectra are very close to Gaussian distributions, independent of the foil parameters and the beam energy. For a given foil the spread in energy and exit angle is maximal if the beam energy is just above the transmission threshold, and decreases steadily with increasing beam energy. Straggling effects are larger in high-Z materials than in low-Z materials. This means that spectra with similar spectral width and angular distribution (flux uniformity) but different mean energies can be obtained by using low-Z materials for low proton energies and high-Z materials for high proton energies.

The thicknesses of foils from two different manufacturers have been measured by means of Rutherford Backscattering Spectrometry (RBS). A beam of monoenergetic protons is targeted on the foil and two surface barrier detectors record the energy of backscattered protons. These detectors are placed at angles of 150° and 165° with respect to the incoming beam. If the beam energy is sufficient, e.g. ≥1800 keV for 6 µm Cu, the spectrum shows a box-shaped feature, the so-called RBS box (cf. Fig. 5). The width of this RBS box can be converted to the foil thickness. The significance of the method is dependent on the detector calibration and the stopping power data for the foil material. The typical error is 2–5%. The SIMNRA[3] code has been used to analyze the RBS spectra [12].

Not only the thickness but also the surface roughness can be determined with RBS by examining the slope of the low energy edge of the RBS box. This edge is always less steep than the high energy edge because of straggling, where a steeper slope indicates a smoother surface. An example of the surface roughness deviation between the two foil manufacturers is represented in the backscattering spectra in Fig. 5. A foil with higher surface roughness produces a broader spectrum for transmitted protons while maintaining the same mean energy.

3.4. Measured proton spectrum

The beam line between the foils and the detector chamber has a diameter of 10 cm. Since this setup is intended for the irradiation of detectors larger than that, the last 1 m of the beam line has been enlarged to 15 cm diameter. Test measurements have shown that the Gaussian shape of the proton spectra, obtained from simulations, is well reproduced except for a low energy tail (cf. Fig. 6(a)). This tail arises because a fraction of protons with exit angles larger than 1.8° are scattered from the inner walls of the beam line onto the irradiation plane. They contribute with a fraction of up to 20% to the spectrum measured in the detector chamber. As a

consequence, two 2 mm aluminum apertures are inserted between the foils and the detector chamber, one with an opening of 3.6 cm at a distance of 59 cm from the foils and a second one with 8.4 cm diameter at 137 cm. These apertures define a cone with an opening angle slightly smaller than the 3.6° defined by the beam line geometry. The fraction of protons with lower energies is drastically reduced to about 4% (cf. Fig. 6(b)). Geant4 simulations show that these 4% arise mostly from the pinhole and the detector aperture (cf. Section 4).

4. Beam monitoring

Up to four silicon surface barrier (SSB) detectors can be used to monitor the proton flux and spectrum, and for the measurement of the beam uniformity. Copper apertures define the effective area of each detector. An aluminum board on the backside of the detector chamber provides various mounting possibilities: either peripheral to monitor the fluence during an irradiation, or at the position of the detector (before an irradiation) to determine the offset from the center and to obtain a beam uniformity map (cf. Fig. 7). In order to correct for dead-time effects of the data acquisition, a pulser signal is added to the signals of the monitor detectors and, simultaneously, given on a separate scaler. The acquisition efficiency is obtained by comparing the number of counts from the pulser in the spectra of the monitor detectors to the scaler value.

Since a perfect reproduction of the beam properties is very challenging, it is crucial to measure the actual proton flux just before an irradiation. If necessary, the beam intensity can be adjusted by changing the extraction voltage of the ion source or by (de-) focusing the beam. In order to shield the test detector during this measurement, a 2 mm thick aluminum plate can be placed in front with a rotation manipulator, leaving just the monitor detectors exposed to the beam.

4.1. Flux monitoring and homogeneity

The most critical parameter for a precise flux measurement is the determination of the openings of the copper apertures in front of the monitor detectors, since they define the effective detector areas. The diameters have been measured by using an x–y-table with µm−position accuracy and an attached microscope with cross hairs. This method determines the effective area to about 2%, which poses the limit on the precision of an absolute flux measurement.

For the measurement of the beam uniformity the 2% precision would only yield an upper limit, since for most useful combinations of foil parameters and beam energy the predicted non-uniformity from TRIM simulations is also of the order of a few percent. Significant measurements become possible by comparing the effective areas of the different detectors. This has been achieved by measuring the rate on two detectors, which are mounted symmetrical to the beam line center, then exchanging the positions and measuring the rate again. The error of this method has been determined to be about 0.3% by repeating some of the measurements.

During a homogeneity measurement the positions of two detectors are altered while two detectors remain at fixed positions. The rates of the moved detectors are then normalized to the mean rate of the fixed ones, to address the problem of fluctuations in the beam current. As an example, a homogeneity map for a beam energy of 2.3 MeV and an 18 µm copper foil is shown in Fig. 8. The flux deviation over an area of 8×8 cm^2 is less than 3%. Such a high uniformity over this large area is a real advantage of the presented setup.

---

[3] SIMulation code for Nuclear Reaction Analysis.
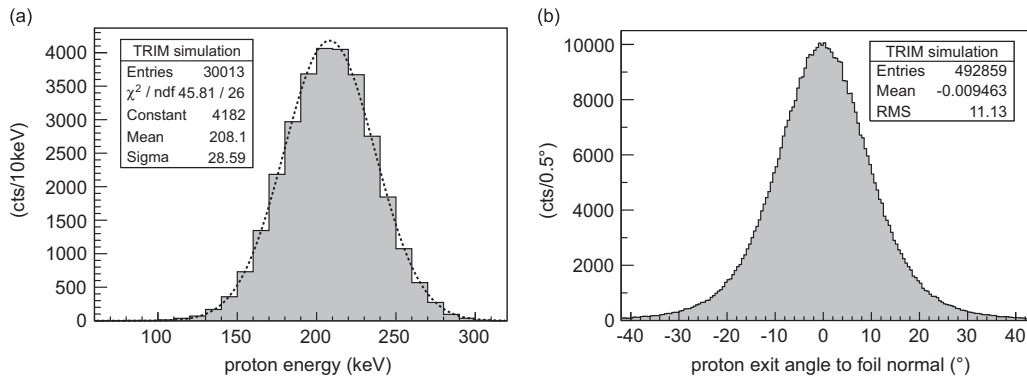
Fig. 4. Results from a TRIM simulation with 1010 keV beam energy and a 6 μm Cu foil. An angular cut of 3° has been applied to the energy spectrum. The dotted line is a Gaussian fit to the spectrum. (a) Simulated energy spectrum, (b) simulated angular distribution.
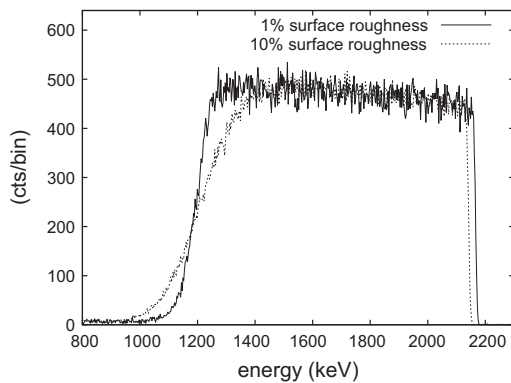
Fig. 5. RBS spectra of Cu foils with a nominal thickness of 6 μm from different manufacturers. Beam energy 2.3 MeV, scattering angle 150°. The size of the RBS box is a measure for the foil thickness. The slope of the low energy edge is dependent on the surface roughness. A steeper edge indicates lower roughness.

4.2. Spectrum monitoring

In order to reduce the dependence on simulations for the applied proton spectra the monitor detectors have been energy calibrated. Since SSBs have an insensitive layer on the front for the electric contact, a calibration with an alpha source, e.g. 5.5 MeV alphas from ^{241}Am, could not be downscaled to the energy range of interest. The lowest proton energy available from the accelerator is 350 keV if a molecular hydrogen beam is used, but the beam current is by far too large to point it directly on a SSB.

The only reasonable possibility for a calibration is the use of backscattered protons from known targets. For this purpose, the SSBs have been mounted in the D-shaped chamber at beam line 2 that has been used for the RBS measurements (cf. Fig. 3). The electronics configuration including all cabling remains the same as in the irradiation setup. The only difference is the use of a different vacuum feed-through, which could introduce a slight change in the capacitance between detector and preamplifier. One by one the SSBs have been calibrated with four different known targets. ^{13}C, aluminum, copper, and gold targets are easily available and cover a wide energy range of backscattered protons without the need for changing the beam energy (cf. Table 2). To determine the ADC channel-to-energy mapping, the positions of the high energy edges of the spectra are used. An example of the calibration is presented in Fig. 9.

A consistency check has been performed by measuring the proton spectrum in the irradiation setup with four detectors that have been calibrated with this method. The largest energy offset between two detectors is less than 12 keV. This indicates an accuracy of the calibration that is more than suitable for the measurement of energy spectra for irradiation purposes.

5. Irradiation of SDDs for *LOFT*

The described setup has been used so far for two irradiation campaigns, in which prototypes of the detectors that will be used on-board *LOFT* have been tested for radiation hardness. In the following, a brief introduction of the *LOFT* project is given and the approach for the irradiation campaigns is presented.

5.1. LOFT mission overview

LOFT is a newly proposed space mission, which was recently selected by ESA as one of five candidates for the M3 mission of the Cosmic Vision program. These five mission concepts compete for a launch opportunity in the early 2020s. The scientific focus of *LOFT* is to answer fundamental questions about the motion of matter orbiting close to the event horizon of a black hole and the state of matter in neutron stars [4].

The satellite will operate in a near-equatorial low Earth orbit (~600 km altitude, $< 5°$ inclination). It will be equipped with two scientific instruments: the *Large Area Detector* (*LAD*) [14] and the *Wide Field Monitor* (*WFM*) [15]. The *LAD* covers a geometric area of ~18 m^2 that leads to an unprecedented effective area of ~10 m^2 at 8 keV X-ray energy. The narrow field-of-view (FOV) of $< 1°$ is defined by novel microcapillary plate X-ray collimators. Complementary to the *LAD* is the *WFM*, a coded mask instrument with a large FOV that covers about 1/3 of the sky. Its main purpose is to provide sources for the *LAD* and to catch transient and bursting events.

Both instruments use the same solid-state detector, a slightly modified version of the Silicon Drift Detector (SDD), which was originally developed for *ALICE* at the *LHC* at CERN and is now implemented in its inner tracking system [13]. This detector offers a small mass-per-area ratio (~1 kg m^{-2}) and an energy resolution of 260 eV at 6 keV. For X-ray detection the thickness of the sensitive layer has been increased from 300 μm to 450 μm. The main difference between the *LAD* and the *WFM* SDDs is the anode pitch (~1 mm for the *LAD*, ~0.15 mm for the *WFM*).

(a)

(b)
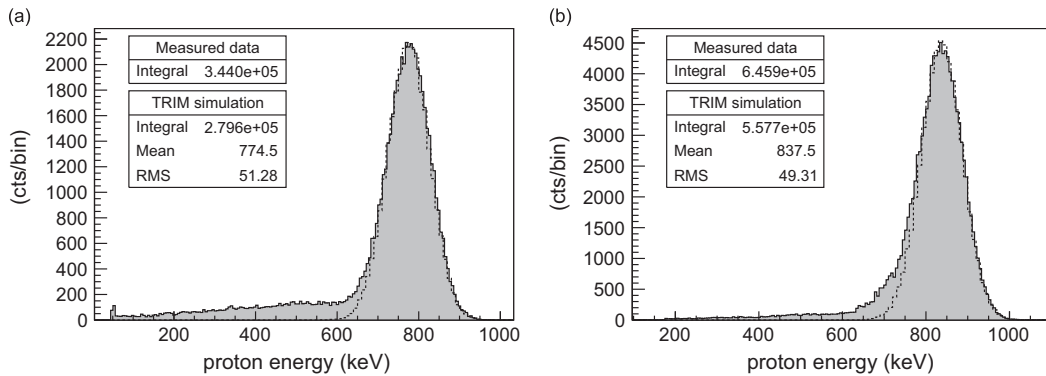
**Fig. 6.** Comparison of the spectrum with and without anti-scatter apertures. Both are measured with an 18 μm Cu foil. The beam energy is about 2.3 MeV, but slightly different for the two measurements, resulting in a shift of the mean energy. The dotted lines represent TRIM simulations with appropriate energies. In the spectrum with anti-scatter apertures the main peak shows an exponential decay at the low energy edge. This is due to forward scattering in the unsensitive top layers of the silicon surface barrier detectors. It is present in the spectrum without anti-scatter apertures as well but barely visible. (a) Without anti-scatter apertures and (b) with anti-scatter apertures.
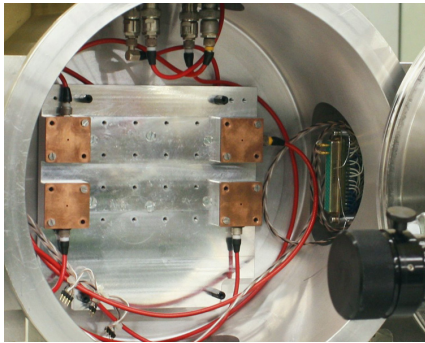
Fig. 7. Picture of the detector chamber (25 cm inside diameter) with four SSB detectors at the peripheral monitor positions. Various mounting possibilities around the center allow a measurement of the flux uniformity and a determination of the offset to the peripheral positions. Copper apertures define the effective areas of the SSBs.
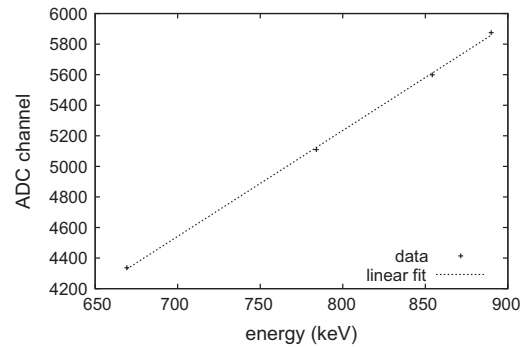
Fig. 9. Calibration of one of the monitor detectors with 165° backscattered protons from ^{13}C, Al, Cu, and Au targets. The beam energy is 908 keV. The parameters from the linear fit are used for the calibration of the spectra measured in the irradiation setup.
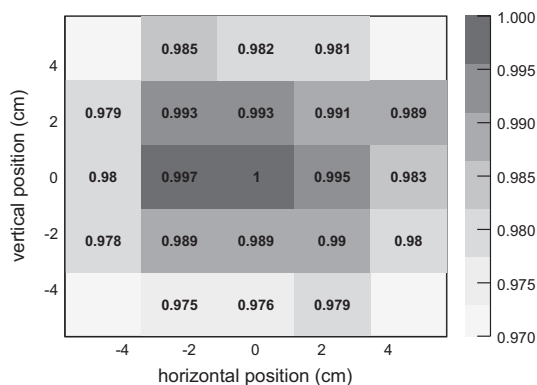
Fig. 8. Measured flux homogeneity map for 2.3 MeV beam energy and an 18 μm Cu foil. The given values are normalized to the center of the beam.

5.2. Irradiation campaigns

Up to now, two irradiation campaigns for *LOFT* SDD prototypes have been carried out with the setup in Tübingen, the first in June 2012, and the second in December 2012. The goal was to determine the degradation of the energy resolution by soft protons during the proposed mission time of 5 years. Further irradiations with more energetic protons (~50 MeV) have been carried out at other facilities.

The irradiated SDDs have half the size of the final version, and a different anode pitch on each side. A picture of one of the detector prototypes is shown in Fig. 10. During irradiation, a bias voltage of 30 V has been applied. The fluence calculation takes into account that the LAD and the WFM have different solid angles, and different materials (optical filters, debris shields, etc.) are placed in front of the detectors.

Since readout electronics are not available yet, the detector characterization is limited to a measurement of the leakage current before and after irradiation. Nevertheless, the combination of the leakage current measurement and additional information, which is gained from the measurement of test structures (gated diodes and MOS capacitors) that are placed in the detector corners, yields a well founded statement on the radiation hardness. A publication that presents the results of the soft proton irradiation campaigns together with the results of other irradiations is in preparation. In the following Sections 5.2.1 and 5.2.2 the irradiation procedures are described, and the nominal and the applied fluences are summarized.

Table 2
Values for the high energy edge of 165° backscattered protons from different target materials for 908 keV beam energy. Without changing the beam energy, a range of more than 200 keV is covered.

Target material	Proton energy (keV)
^{13}C	669.2
Al	784.0
Cu	854.3
Au	889.9
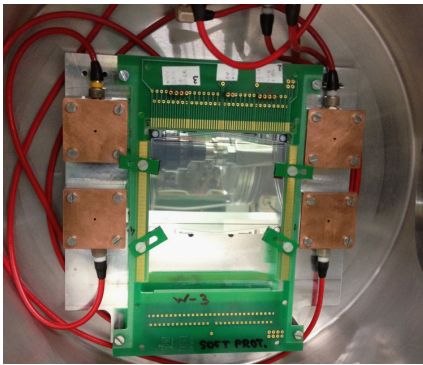
Fig. 10. Picture of a *LOFT* detector prototype on a printed circuit board (PCB), mounted in the irradiation chamber with four monitor detectors around. The connectors on the upper part of the PCB have been used to bias the SDD and test structures around the SDD during the irradiation.

Table 3
Nominal fluences Φ_{nom} and applied fluences Φ_{app} of the four irradiation steps of the first irradiation campaign. The nominal fluences are calculated for 208 keV and 820 keV, while during the irradiation 300 keV and 838 keV have been used. The total nominal dose corresponds to 2.0 times the orbital NIEL for the WFM, and to 14.9 times the orbital NIEL for the LAD.

Irradiation step	$\Phi_{nom,208\ keV}$ (cm^{-2})	$\Phi_{app,300\ keV}$ (cm^{-2})	$\Phi_{nom,820\ keV}$ (cm^{-2})	$\Phi_{app,838\ keV}$ (cm^{-2})
1	3.50×10^6	3.38×10^6	7.85×10^5	9.53×10^5
2	3.50×10^6	3.44×10^6	7.85×10^5	6.51×10^5
3	–	–	2.40×10^7	2.24×10^7
4	1.10×10^5	1.36×10^5	4.28×10^7	4.34×10^7
Total	7.11×10^6	6.96×10^6	6.84×10^7	6.74×10^7

5.2.1. First preliminary irradiation campaign

In the first campaign two proton energies were used: 300 ± 33 keV to maximize ionization in the insulating field oxide on the SDD surface, and ~838 ± 52 keV, because it is the maximal energy available for a uniform flux distribution. The fluence has been applied in four steps with intermediate measurements of the I–V-curves of the gated diodes, and leakage current measurements before and after the entire irradiation. The fluence for each step is selected to reach a defined NIEL for the WFM and the LAD: in Step 1 half the NIEL expected for the LAD is reached, Step 2 increases the NIEL to the orbital value for the LAD, Step 3 reaches approximately the orbital NIEL for the WFM, and finally Step 4 increases the NIEL to twice the orbital value for the WFM. The irradiations were performed on three sequential days and the irradiation durations for the individual steps ranged from several seconds to more than 10 min. The nominal fluences have been calculated for slightly lower energies (208 keV and 820 keV) than the ones applied. The nominal and the applied fluences of each step are listed in Table 3.

Table 4
Nominal fluences Φ_{nom} and applied fluences Φ_{app} for the two SDD prototypes used in the second irradiation campaign (Prototype 1 is the same detector that has been used in the first campaign). The nominal fluences correspond to 10 times the orbital NIEL expected for the WFM (74.5 times LAD).

SDD prototype	$\Phi_{nom,838\ keV}$ (cm^{-2})	$\Phi_{app,838\ keV}$ (cm^{-2})
1	3.59×10^8	3.73×10^8
2	3.59×10^8	3.62×10^8

5.2.2. Second irradiation campaign

For the second campaign two SDD prototypes from different development stages have been irradiated. Prototype 1 is the same detector that has been used in the first campaign. Meanwhile, the induced radiation damages have annealed. The second SDD is the latest prototype for *LOFT*. The irradiation procedure was simplified compared to the first campaign by using just one proton energy (838 ± 53 keV) and applying the total fluence in only one step. Since the fluence was calculated to induce ten times the orbital WFM NIEL, the flux has been increased as much as possible to minimize the duration, and, therefore, avoid annealing effects during the irradiation. Both detector prototypes have been irradiated on the same day and each irradiation took less than half an hour. The nominal and applied fluences for the two detectors are given in Table 4.

6. Conclusions

A setup for the irradiation of solid-state detectors with soft protons has been constructed at the accelerator facility of the University of Tübingen. It has already proven its applicability for radiation hardness tests of X-ray detectors for future space missions.

The monitoring system with silicon surface barrier detectors enables the test of new detector prototypes under orbital radiation conditions, even in early development phases when readout electronics are not yet available. The applied methods for the energy calibration and the determination of the effective areas of the monitor detectors show consistent results. The contribution of small angle scattered protons is effectively reduced with additional apertures. Another key advantage of the setup is the high beam uniformity with a flux deviation of less than 3% over an area of 8×8 cm^2. Therefore, the setup is especially suitable for the irradiation of large detectors up to diameters of about 14 cm.

Two irradiation campaigns for the *LOFT* project have been carried out so far, in which the desired fluences have been reached within a few percent. A publication that presents the results of these campaigns together with the results of other irradiations of *LOFT* detector prototypes is in preparation. Further applications of the setup for *LOFT* detector prototypes are likely, and the setup is available for the irradiation of other solid-state detectors as well, e. g. the *SVOM*[4] CCDs or the CdZnTe detectors that are intended for the use on-board *MIRAX*.[5]

Underway is a modification and extension of the irradiation setup that will give the possibility to measure small angle reflection rates of soft protons under grazing incidence. The scattering targets will be X-ray mirror shells, like the ones used on *eROSITA*.[6] The goal is to achieve an energy and angular resolution that is sufficient to constrain the underlying physical process. The results will be beneficial for simulations of soft proton background and detector damage on X-ray observatories with focusing Wolter-type optics.

---

[4] Space-based multi-band astronomical Variable Objects Monitor.
[5] Monitor e Imageador de RAios-X.
[6] extended ROentgen Survey with an Imaging Telescope Array.

Acknowledgments

References

[1] P. Nieminen, R. Nartallo, E. Daly, H.D.R. Evans, J. Sørensen, F. Lei, P.R. Truscott, S. Giani, Low-energy proton effects on detectors on X-Ray astronomy missions, in: Conference Proceeding of CHEP 2000, Padova, ID. A130, 2000.
[2] D.H. Lo, J.R. Srour, IEEE Transactions on Nuclear Science NS-50 (6) (2003) 2018.
[3] B. Aschenbach, Grazing incidence reflection and scattering of MeV protons, in: Proceedings of SPIE, vol. 6688, ID. 66880I, 2007.
[4] M. Feroci, et al., Experimental Astronomy 34 (2) (2012) 415.
[5] J. Moritz, Zeitschrift für Geophysik 38 (4) (1972) 701.
[6] A.N. Petrov, O.R. Grigoryan, N.V. Kuznetsov, Advances in Space Research 43 (2009) 654.
[7] R.B. Brown, D. Powers, Nuclear Instruments and Methods in Physics Research Section A 151 (1978) 377.
[8] P. Kump, V. Ramí£ak, P. Rupnik, M. Vakselj, Nuclear Instruments and Methods in Physics Research Section A 112 (1973) 489.
[9] J.W. Butler, C.M. Davisson, Nuclear Instruments and Methods in Physics Research Section A 149 (1978) 183.
[10] J.F. Ziegler, M.D. Ziegler, J.P. Biersack, Nuclear Instruments and Methods in Physics Research Section B 268 (2010) 1818.
[11] S. Agostinelli, et al., Nuclear Instruments and Methods in Physics Research Section A 506 (2003) 250.
[12] M. Mayer, SIMNRA User's Guide 6.05, Max-Planck-Institut für Plasmaphysik, Garching, 2009.
[13] A. Rashevsky, V. Bonvicini, P. Burger, S. Piano, C. Piemonte, A. Vacchi, Nuclear Instruments and Methods in Physics Research Section A 485 (2002) 54.
[14] S. Zane, et al., A large area detector proposed for the large observatory for X-ray timing LOFT, in: Proceedings of SPIE, vol. 8443, ID. 84432F, 2012.
[15] S. Brand, et al., The LOFT wide field monitor, in: Proceedings of SPIE, vol. 8443, ID. 84432G, 2012.

5.3 A Facility for Soft Proton Irradiation and Instrument Testing for Future Space Missions

A Facility for Soft Proton Irradiation and Instrument Testing for Future Space Missions

Sebastian Diebold, Josef Jochum, Eckhard Kendziorra,
Emanuele Perinati, Andrea Santangelo, and Chris Tenzer

Kepler Center for Astro and Particle Physics, Universität Tübingen,
Sand 1, Tübingen, Germany
Phone: +49 7071 29 78609   Fax: +49 7071 29 3458
Email: diebold@astro.uni-tuebingen.de

Abstract—Orbital soft protons (from tens of keV to a few MeV) can seriously degrade the performance of astronomical X-ray detectors. An irradiation setup for large detectors as well as passive satellite components has been constructed at the accelerator facility of the University of Tübingen. The experimental setup and recent applications are briefly described. Simulations and measurements of an improved aperture design are presented in detail.

Modifications of the irradiation setup to enable measurements of the small angle scattering efficiency of Wolter-type X-ray mirror shells are underway. Details of the implementation and the current status are given.

I. INTRODUCTION

Protons impinging on solid-state detectors on-board astronomical X-ray observatories pose a severe threat to the detector quality, since they can degrade the X-ray detection performance – e.g. energy resolution, position resolution, and sensitivity – or even lead to a detector failure. Soft protons in the energy range between tens of keV and several MeV are potentially more harmful than energetic minimal ionizing particles (MIPs), because the energy deposition is larger and the damages are concentrated in a small volume around the stopping point [1]. A well-studied example of this kind of damage is the sudden increase in the charge transfer inefficiency (CTI) of the *Chandra ACIS* front-illuminated CCDs during the first month of operation [2].

Low Earth orbits can provide efficient shielding from energetic particles, as long as the inclination is small enough ($<5°$) to avoid the South Atlantic Anomaly (SAA). Nevertheless, in these near-equatorial low Earth orbits an enhancement of the soft proton component has been reported [3].

Especially solid-state detectors of X-ray observatories are vulnerable to this type of radiation, since they are directly reachable through collimator holes and openings of coded masks. Experimental tests are necessary to study the effects of soft protons on X-ray detectors for future missions, in order to find an optimized radiation hard design and to estimate the performance degradation throughout the mission duration. A setup for such irradiations has been constructed at the Van-de-Graaff accelerator facility of the University of Tübingen. It provides a high flux uniformity over a large area, and the monitoring system for the applied spectrum and fluence allows tests of detector prototypes without readout electronics, as well as irradiations of passive satellite components.

Even in the case of X-ray observatories with focusing Wolter-type optics, where the detectors are shielded from direct radiation, a high flux of soft protons has been observed at the focal plane [4]. Since multiple Rutherford scattering cannot explain the measured rates [5], different funneling mechanisms have been proposed [6], [7] (chronology in [8]). Experimental studies are rare and cover only a small part of the parameter space (a few experimental results are reported in [9]). Therefore, a modification of the irradiation setup is underway to enable small angle scattering measurements of soft protons under grazing incidence. It will be used to test X-ray mirror shells for existing and future space instruments. The goal is further to pinpoint the physical process responsible for the enhanced funneling rates and to provide input to tune simulation codes.

Section II briefly summarizes the irradiation setup and its applications (more details in [10]). Section II-B gives a detailed description of simulations to improve the design of apertures with small openings $<1\,\mathrm{mm}$. Recent modifications of this setup to enable small angle scattering measurements are presented in Section III.
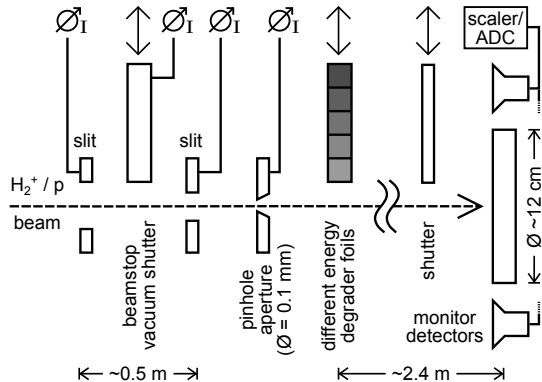
Fig. 1. Schematic of the irradiation setup. Two slits are used to check the alignment of the incoming beam. A pinhole aperture reduces the beam current before the beam is degraded and spatially widened with thin metal foils. Peripheral mounted detectors monitor fluence and spectrum at the irradiation plane. During flux adjustment a shutter shields the central region while leaving the monitor detectors uncovered.

II. Soft Proton Irradiation Setup

A scheme of the irradiation setup is presented in Fig. 1. The incoming beam from the accelerator passes through two slits. Various dipole magnets allow bending and parallel shifting of the beam, and by equalizing the currents on opposite slit parts the beam can be centered and aligned parallel to the beam line. A pinhole aperture with a diameter of 0.1 mm reduces the beam current to obtain fluxes in the range 10^3–$5 \cdot 10^5$ cm^{-2}s^{-1} on the detector plane.

Irradiations can either be performed with quasi-monoenergetic spectra, that produce the same NIEL (non-ionizing energy loss) and TID (total ionizing dose) as expected under orbital radiation conditions, or the expected orbit spectrum can be composed by irradiating with several Gaussian spectra in succession. Although the latter method is physically straightforward, the long irradiation durations (up to a few hours) can lead to significant annealing of the introduced damages during the irradiation.

A. Degrader Foils

Since 500 kV is currently the lowest stable terminal voltage of the accelerator, degrader foils with a few µm thickness reduce and broaden the beam energy, and also widen the beam spatially. Four different foils can be mounted on a linear manipulator, to allow a change without breaking the vacuum.

TRIM [11] simulations are used to find appropriate combinations of foil material, thickness, and beam en-

Fig. 2. Comparison of the former aperture design (a) to the improved one (b), where the chamfer does not reach the upstream side. This minimizes energy degradation since soft protons cannot penetrate around the opening any more.

ergy to obtain a certain proton spectrum with a sufficient flux uniformity across the irradiation plane. Highly uniform flux distributions can be achieved in the energy range from below 100 keV to about 1 MeV. Irradiations with higher energies are possible by sacrificing flux uniformity.

Measured proton spectra after the foils are close to Gaussian distributions, as expected from simulations. A tail to lower energies that arises because of small angle scattering at the inner walls of the beam line could be efficiently reduced with two additional apertures. These are mounted between the foils and the detector chamber, and leave just a cone with an opening angle slightly smaller than the 3.6° defined by the beam line geometry.

B. Aperture Design

Nevertheless, a small fraction of protons remains shifted to lower energies. Monte Carlo simulations by means of Geant4 [12] show, that this fraction arises because protons penetrate the pinhole and detector apertures close to the openings. This is possible because a 45°-chamfer on the downstream side is milled through the entire material thickness (cf. Fig. 2 (a)). The chamfer effectively reduces slit scattering, but for small aperture diameters of the order of 100 µm the size of the penetrable circular disc around the opening is comparable to the open area. This leads to a considerable fraction of additionally scattered, and thus degraded, protons (see spectra in [10]).

An improved aperture design has been simulated, in which the chamfer does not reach the upstream side but stops 200 µm above (cf. Fig. 2 (b)). Fig. 3 shows simulated proton and delta-electron tracks for 1000 incoming 1 MeV protons impinging on 100 µm apertures. It can be seen that the improved design strongly reduces beam widening, as well as the fraction of delta-electrons in forward direction. In Fig. 4 the corresponding spectra are presented, each obtained for 20,000 simulated protons impinging on a circular area 200 µm in diameter and centered on the aperture opening. The overall spectrum is marked by black symbols. The dark gray bars indicate the fractions of protons with an exit angle <3°, while the
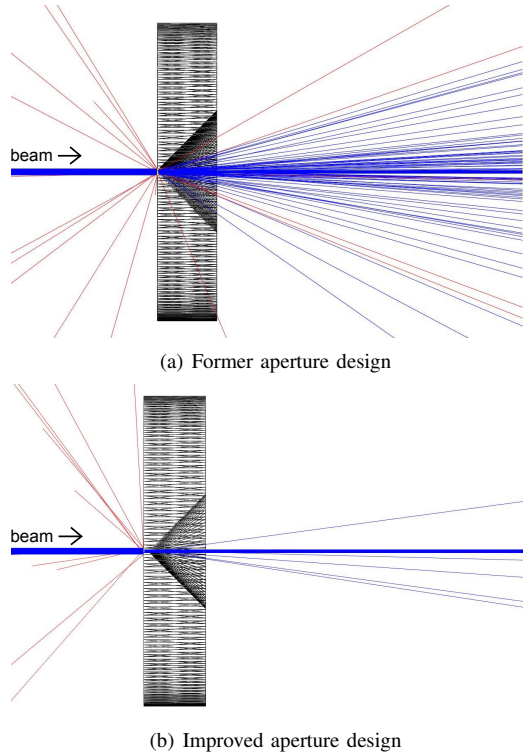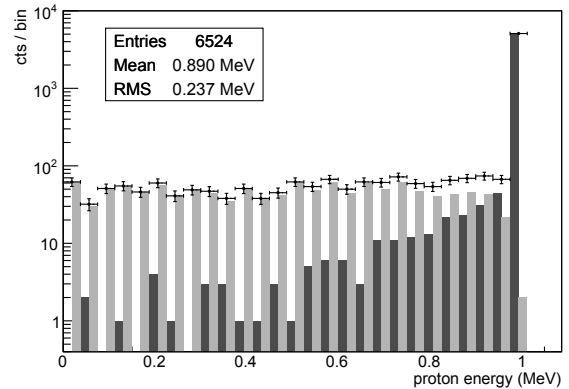
(a) Former aperture design

(b) Improved aperture design

Fig. 3. Visualization of Geant4 Monte Carlo simulations. 1000 1 MeV protons impinging on 100 μm apertures have been simulated. The blue lines represent proton tracks, while the tracks of delta-electrons are colored in red. The improved design strongly reduces beam widening, as well as delta-electrons in forward direction.

(a) Former aperture design

(b) Improved aperture design

Fig. 4. Proton spectra from Geant4 Monte Carlo simulations. 20,000 1 MeV protons impinging on 100 μm apertures have been simulated. The black symbols mark the overall spectra. The dark gray bars indicate the fractions exiting in forward direction (<3°), while the light gray bars contain the remaining protons. The former aperture design introduces additional beam degradation and widening, whereas these effects are minimized in the improved design.

light gray bars contain the remaining protons that have been scattered to larger angles. The latter fraction can be disregarded when considering the application as pinhole aperture, because in that case these protons are absorbed in the beam line and thus do not reach the irradiation chamber. In general, the improved apertures considerably reduce the fraction of degraded and deflected protons compared to the former design.
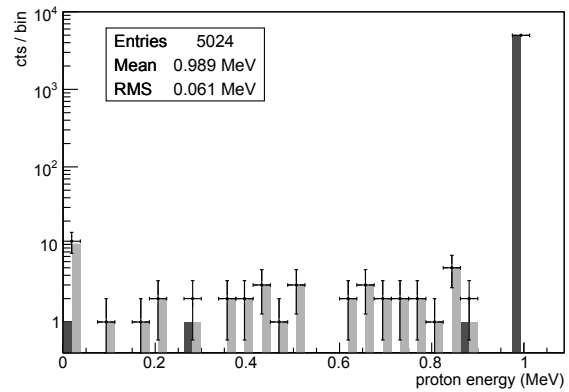
An example of a spectrum measured with an improved 100 μm pinhole is given in Fig. 5. The deviation between measurement and TRIM simulation is almost completely due to the finite energy resolution of the detector (~15 keV FWHM). The improved apertures are particularly important for the small angle scattering setup described in Section III.

C. Beam Monitoring

A monitoring system for the applied fluence, the flux uniformity, and the proton spectrum has been set up. This system makes irradiations of new detector prototypes possible, for which readout electronics are not yet available, as well as irradiations of passive satellite components. Up to four silicon surface barrier (SSB) detectors are used for the monitoring. The backside of the detector chamber provides various mounting possibilities for the SSBs, peripheral to monitor the fluence during an irradiation, or around the center to measure the flux uniformity and the offset between different positions prior to an irradiation (cf. Fig. 6). A movable aluminum plate shields the center of the irradiation chamber during setting up the beam, while leaving the monitor detectors uncovered.
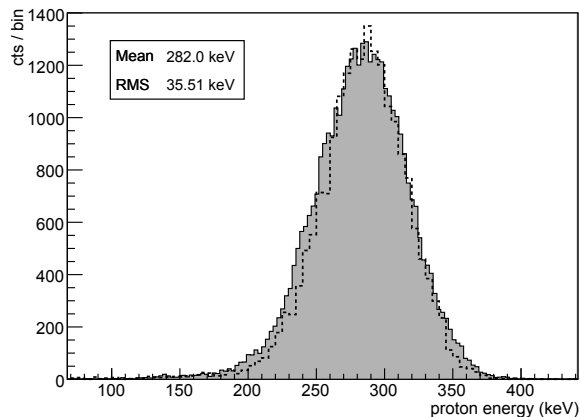
Fig. 5. Measured proton spectrum. The mean energy of 282 keV was achieved by degrading a 1055 keV proton beam with a 6 μm copper foil. The dashed line represents a TRIM simulation. The small deviation between measurement and simulation is mostly due to the finite energy resolution of the detector.

Fig. 6. Picture of the detector chamber (25 cm diameter) during the second irradiation campaign for *LOFT* SDD prototypes. An SDD (7.2×5.6 cm^2) is fixed on a PCB and mounted in the center. Two SSB detectors are mounted peripheral to monitor the applied spectrum and fluence. Their effective areas are defined by copper apertures.

1) Fluence monitoring and flux uniformity: The critical parameter for the precision of flux and fluence measurements is the determination of the effective area of the monitor detectors. The diameters of the apertures have been measured by using an x-y-table with μm position accuracy and a microscope with cross-hairs. An accuracy of about 2% for the absolute effective area has been reached. Thus, 2% is the limit for absolute fluence determination. Relative flux measurements at different positions across the irradiation plane showed deviations as small as a few percent.

2) Spectrum monitoring: For the monitoring of the applied spectra, an energy calibration of the SSBs is necessary. This has been achieved by calibrating with backscattered protons from known targets. The calibration of the beam energy has been checked before by measuring the gamma rate around the sharp 992 keV resonance of the reaction ^{27}Al(p,γ)^{28}Si. The largest measured energy offset between two detectors in the irradiation setup is 12 keV. The measured spectra of degraded beams are consistent with simulations (cf. Fig. 5).

D. Applications

1) LOFT SDD prototypes: LOFT (*Large Observatory For x-ray Timing*) [13] is a proposed astronomical space mission that is currently in the assessment phase. It competes with four other projects for a launch opportunity in the early 2020s in the frame of ESA's Cos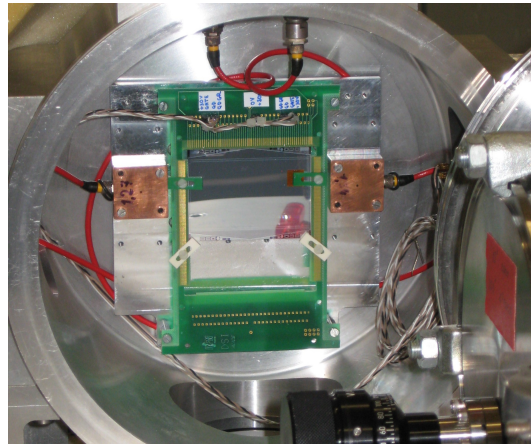mic Vision program. It will be equipped with two scientific instruments, the *Large Area Detector* (*LAD*) [14] and the *Wide Field Monitor* (*WFM*) [15]. Both will use the same detector, a slightly modified version of the Silicon Drift Detector (SDD) that is installed in the inner tracking system of *ALICE* [16] at the *LHC* (*Large Hadron Collider*).

The proposed orbit for *LOFT* is a near-equatorial low Earth orbit (~600 km altitude, <5° inclination). Therefore, the potential degradation of the SDDs by soft protons has to be studied. In 2012 two irradiation campaigns have been performed with SDD prototypes for *LOFT* (cf. Fig. 6). Both campaigns were successful and the desired fluences have been reached within the accuracy of the monitoring.

2) ADM-Aeolus window coatings: The setup is certainly not limited to tests of X-ray detectors. *ADM-Aeolus* (*Atmospheric Dynamics Mission*) [17] is a future Earth observation mission within ESA's Living Planet program. Its objective is to acquire wind profiles on a global scale using an active Doppler wind lidar instrument called *ALADIN* (*Atmospheric LAser Doppler INstrument*).

Windows with special (anti-) reflective coatings are developed for this mission to achieve optimal transmission and reflection efficiency. To determine the effect of orbital soft protons on the properties of these coatings, an irradiation campaign is scheduled for October 2013. Intention of the test is to study the effect of protons that stop within the coatings with thicknesses below 1.5 μm.
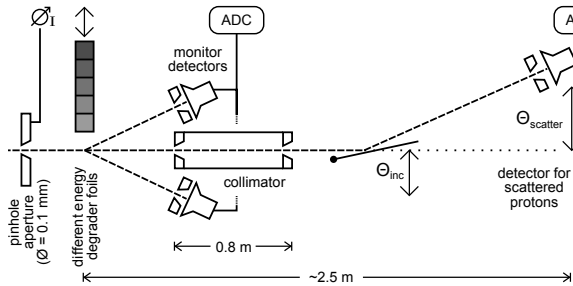
Fig. 7. Scheme of the small angle scattering setup. Components left of the pinhole aperture are arranged in the same way as in the irradiation setup (cf. Fig. 1). A collimator cuts out a part of the widened beam in direction of the scattering target, which is mounted on a tiltable table. To normalize the measured proton rates to fluctuations in the beam current, two monitor detectors are placed besides the collimator entrance.
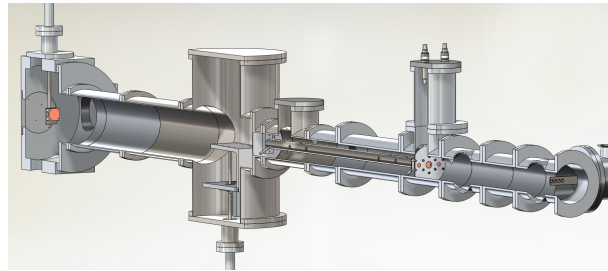

Fig. 8. CAD drawing of the small angle scattering setup in cross sectional view. Beam direction is from right to left. The degrader foils are at the far right. The collimator with the monitor detectors is installed in front of the scattering chamber that contains a tiltable target table. A detector for the scattered protons is mounted at the end of the beam line.

Therefore, protons in the energy range 100–200 keV will be applied.

III. SMALL ANGLE SCATTERING SETUP

The irradiation setup is currently modified to enable rate and energy measurements of soft protons that are scattered under grazing incidence at Wolter-type X-ray mirror shells. The requirements for this experiment are derived from Geant4 simulation results in [8]. Main challenges are the adjustment of incident and scattering angle with a precision $<0.1°$ and the accurate determination of these angles, as well as the normalization of the measured scattering rate to fluctuation of the beam current.

A. Experiment Design

A scheme of the scattering setup is shown in Fig. 7, a CAD model cross section in Fig. 8. Note that the beam direction in the scheme is from left to right, while in the cross section it is reversed.

The configuration upstream of the degrader foils is the same as for the irradiation setup (cf. Fig. 1). Again, thin foils degrade the beam energy and widen the beam spatially. A collimator with a length of 80 cm and openings smaller than 1 mm cuts out a part of the widened beam in the direction of the scattering target. The use of the improved aperture design described in Section II-B is crucial for this application to obtain an undisturbed narrow proton beam. Apertures around the collimator openings shut the remaining space between the collimator and the beam line. In the scattering chamber, the target – e.g. an X-ray mirror shell – is mounted on a tiltable table. The tilt angle of the table

with respect to the collimator axis is adjustable via a linear manipulator with 10 μm position accuracy. It is also possible to remove the target completely from the course of beam. An SSB detector to measure the scattered protons is mounted on a similar manipulator at the end of the beam line.

For the adjustment of the collimator openings in-line with the pinhole aperture and the detector for scattered protons a theodolite is used, which is positioned behind the end of the beam line. A laser, inserted after the degrader foils and shining through the collimator, is used to determine the zero position and incident and scattering angle. Visible light increases the noise of the SSB detector. This increase can be quantized with an RMS voltmeter. Since the high quality surface of X-ray mirrors provides a good reflectivity for visible light, the angles can be determined by measuring the position of the reflected laser beam and combining the result with geometrical measurements of the setup. An accuracy and reproducibility of incident and scattering angle well below $0.1°$ can be achieved.

Fluctuations in the beam current can be as large as 50%. These are due to the limited stability of the ion source and the bending magnets and, in particular, to a continuous spatial wobbling of the beam. To correct for that, two additional detectors mounted besides the collimator entry monitor the incoming beam. A calibration can be obtained by removing the target and comparing the rates on the monitors with the rate in forward direction. This method yields a considerable advantage in determining the flux on the target to the conventional method of removing the target and tapping the electrical current from a Faraday cup every now and then.
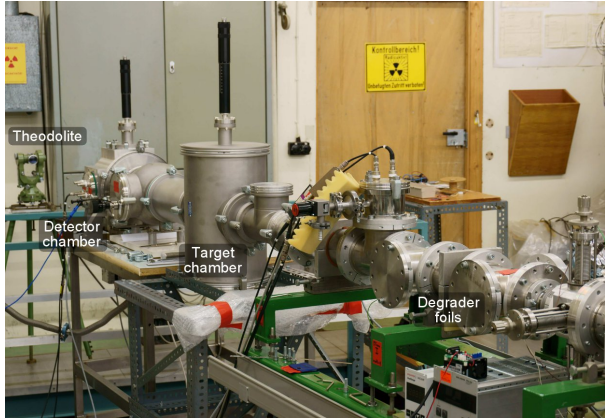
Fig. 9. Picture of the small angle scattering setup. The collimator and all detectors are in place, just the tiltable target table remains to be installed. The theodolite behind the end of the beam line is used to align the beam line and the apertures.
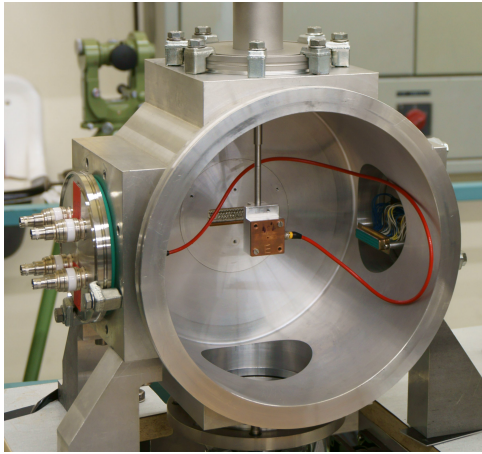

Fig. 10. Picture of the inside of the detector chamber. An SSB detector with a copper aperture is mounted on a linear manipulator.

B. Current Status

The actual implementation at the beam line is shown in Figs. 9 and 10. The collimator with exchangeable apertures and mountings for the monitor detectors is in place and the target chamber is installed as well as all detectors. The tiltable target table remains to be installed, as well as guides to improve the horizontal position stability of the detector for scattered protons.

Preliminary beam tests are very promising and show that the mechanical adjustment by means of the theodolite and the zero position determination with the laser work well. Relatively large apertures with 1 mm diameter
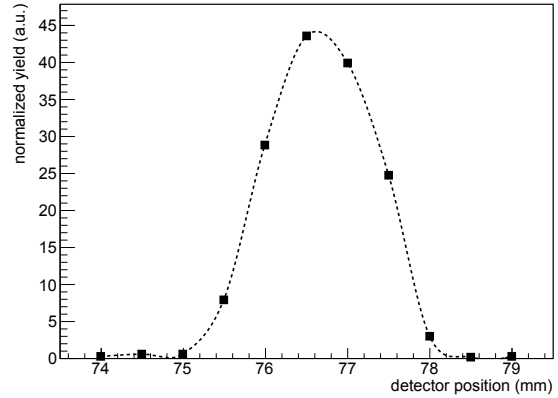
Fig. 11. Results of a preliminary beam test without a target. The yield is normalized to the monitor detectors. The width of the peak of ~1 mm represents the diameters of collimator and detector apertures.
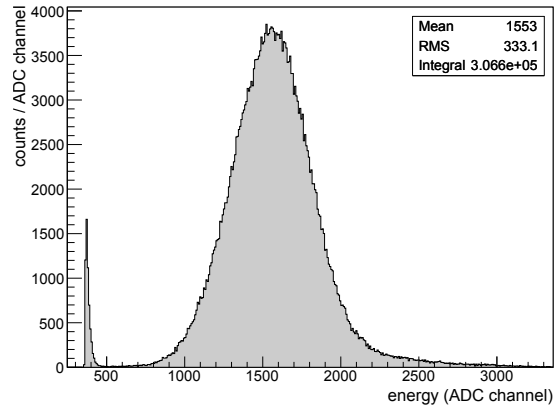
Fig. 12. Spectrum measured during a preliminary beam test at the 77 mm position. The mean proton energy is ~350 keV. The steep rise around ADC channel 400 is due to detector noise.

for the collimator and in front of the detectors have been used. The result for protons with ~350 keV mean energy (1030 keV beam energy, 12 µm aluminum degrader) are shown in Fig. 11. The width of the peak of ~1 mm represents the aperture diameters. Smaller apertures with 0.3 and 0.1 mm diameter are currently tested. Exemplarily, the spectrum measured at the 77 mm position (cf. Fig. 11) is presented in Fig. 12. The detector has not yet been calibrated.

C. Prospects

First targets for the scattering experiment will be parts of mirror shells for *eROSITA* (*extended ROentgen Survey with an Imaging Telescope Array*) [18]. *eROSITA* is the main instrument on the Russian *SRG* mission (*Spektrum-Roentgen-Gamma*) and consists of

seven Wolter-I telescope modules, providing a total effective area of ~1500 cm^2 at 1.5 keV photon energy.

IV. Conclusions

The setup for soft proton irradiations at the accelerator facility of the University of Tübingen provides a high flux uniformity of the order of 2% over an area of 8×8 cm^2. This makes it suitable for irradiations of large format detectors up to 12 cm diameter. An independent monitoring system allows early testing of new detector prototypes, when readout electronics are not yet available, as well as irradiations of passive space components. The setup has proven its applicability in two irradiation campaigns for *LOFT* SDD prototypes. Tests of window coatings for *ADM-Aeolus* are scheduled, and the setup is available for further applications.

A considerable improvement in the aperture design for small openings <1 mm has been achieved. Monte Carlo simulations by means of Geant4 indicate a strong reduction of beam degradation and deflection for the new design. Measured proton spectra are now in best agreement with TRIM simulations.

The construction of an experimental setup to measure soft proton small angle scattering under grazing incidence is almost finished. Preliminary measurements to test the methods for alignment and flux normalization show promising results. First application will be the study of the small angle scattering efficiency of X-ray mirror shells for *eROSITA*.

In addition to the proton experiments, a deuterium gas target is currently tested and optimized at the same facility. It will be used to produce monoenergetic neutrons of a few MeV via the d-d fusion reaction, in order to study the neutron radiation hardness of silicon detectors for accelerator experiments and space missions. In space neutrons are produced by highly energetic cosmic rays via spallation. An NE213 liquid scintillation detector, a long counter, and activation foils are used to monitor flux and applied fluence. The goal is to reach a neutron flux >10^8 cm^{-2}s^{-1}.

References

[1] P. Nieminen et al., "Low-Energy Proton Effects on Detectors on X-Ray Astronomy Missions", Conference Proceeding of CHEP 2000, Padova, Id. A130, 2000.

[2] D. H. Lo, J. R. Srour, "Modeling of proton-induced CCD degradation in the Chandra X-ray observatory", IEEE Trans. Nucl. Sci., Vol. 50, Iss. 6, pp. 2018–2023, 2003.

[3] A. N. Petrov et al., "Creation of model of quasi-trapped proton fluxes below Earth's radiation belt", Adv. Space Res., Vol. 43, pp. 654–658, 2009.

[4] E. Kendziorra et al., "The effect of low energy protons on the performance of the EPIC pn-CCD detector on XMM-Newton", Proc. SPIE, Vol. 4140, pp. 32–41, 2000.

[5] B. K. Dichter, S. Woolf, "Grazing Angle Proton Scattering: Effects on Chandra and XMM-Newton X-ray Telescopes", IEEE Trans. Nucl. Sci., Vol. 50, Iss. 6, pp. 2292–2295, 2003.

[6] F. Lei et al., "Update on the use of Geant4 for the Simulation of low-energy protons scattering off X-ray Mirrors at grazing incidence angles", IEEE Trans. Nucl. Sci., Vol. 51, Iss. 6, pp. 3408-3412, 2004.

[7] B. Aschenbach, "Grazing Incidence Reflection and Scattering of MeV Protons", Proc. SPIE, Vol. 6688, Id. 66880I, 2007.

[8] V. Fioretti, "Background minimization issues for next generation hard X-ray focusing telescopes", PhD Thesis, University of Bologna, 2011.

[9] R. Nartallo et al., "Radiation Environment Induced Degradation on Chandra and Implications for XMM", ESA Report, 2000.

[10] S. Diebold et al., "A setup for soft proton irradiation of X-ray detectors for future astronomical space missions", Nucl. Instrum. Methods Phys. Res., Sect. A, Vol. 721, pp. 65–72, 2013.

[11] J. F. Ziegler et al., "SRIM - The stopping and range of ions in matter (2010)", Nucl. Instrum. Methods Phys. Res., Sect. B, Vol. 268, pp. 1818–1823, 2010.

[12] S. Agostinelli et al., "Geant4 - a simulation toolkit", Nucl. Instrum. Methods Phys. Res., Sect. A, Vol. 506, pp. 250–303, 2003.

[13] M. Feroci et al., "The Large Observatory for X-ray Timing (LOFT)", Exp. Astron., Vol. 34, Iss. 2, pp. 415–444, 2012.

[14] S. Zane et al., "A large area detector proposed for the Large Observatory for X-ray Timing (LOFT)", Proc. SPIE, Vol. 8443, Id. 84432F, 2012.

[15] S. Brand et al., "The LOFT wide field monitor", Proc. SPIE, Vol. 8443, Id. 84432G, 2012.

[16] A. Rashevsky et al., "Large area Silicon Drift Detector for the ALICE experiment", Nucl. Instrum. Methods Phys. Res., Sect. A, Vol. 485, pp. 54–60, 2002.

[17] A. Stoffelen et al., "The Atmospheric Dynamics Mission For Global Wind Field Measurement", Bull. Amer. Meteor. Soc., Vol. 86, pp. 73–87, 2005.

[18] N. Cappelluti et al., "eROSITA on SRG: a X-ray all-sky survey mission", Proc. WFXT meeting, 2010.

5.4 Soft proton scattering efficiency measurements on x-ray mirror shells

Soft proton scattering efficiency measurements on x-ray mirror shells

Sebastian Diebold[1] · **Chris Tenzer**[1] · **Emanuele Perinati**[1] · **Andrea Santangelo**[1] ·
Michael Freyberg[2] · **Peter Friedrich**[2] · **Josef Jochum**[3]

Abstract In-orbit experience has shown that soft protons are funneled more efficiently through focusing Wolter-type optics of X-ray observatories than simulations predicted. These protons can degrade the performance of solid-state X-ray detectors and contribute to the instrumental background. Since laboratory measurements of the scattering process are rare, an experiment for grazing angles has been set up at the accelerator facility of the University of Tübingen. Systematic measurements at incidence angles ranging from 0.3° to 1.2° with proton energies around 250 keV, 500 keV, and 1 MeV have been carried out. Parts of spare mirror shells of the *eROSITA* (extended ROentgen Survey with an Imaging Telescope Array) instrument have been used as scattering targets. This publication comprises a detailed description of the setup, the calibration and normalization methods, and the scattering efficiency and energy loss results. A comparison of the results with a theoretical scattering description and with simulations is included as well.

✉ S. Diebold
diebold@astro.uni-tuebingen.de

[1] Institute for Astronomy and Astrophysics, Kepler Center for Astro and Particle Physics, University of Tübingen, Sand 1, 72076 Tübingen, Germany

[2] Max Planck Institute for Extraterrestrial Physics, Giessenbachstrasse 1, 85748 Garching, Germany

[3] Physics Institute Tübingen, Kepler Center for Astro and Particle Physics, University of Tübingen, Auf der Morgenstelle 14, 72076 Tübingen, Germany

1 Introduction

Astronomical X-ray satellites are exposed to various kinds of particle radiation: trapped protons and electrons, solar wind particles, and energetic particles of extrasolar origin. Although the radiation environment is highly variable and depends strongly on the orbit, usually protons have the largest impact on the mission. The effects of proton radiation on the performance of X-ray instruments can be sub-divided into two classes: degradation of the detector performance and contribution to the background of astronomical observations – either via direct interaction with the detector, or, more likely, via the production of secondary particles and fluorescence in the surroundings of the detector. Therefore, detailed studies of the expected proton flux at the detector location enable not only an assessment of possible radiation damages, moreover they are crucial to evaluate the scientific performance of an instrument, i.e. the signal-to-noise ratio.

Since irradiation tests of completely assembled X-ray instruments are hardly feasible, Monte Carlo based radiation transport codes are used to simulate the interactions of the orbital radiation with the spacecraft and the scientific instrumentation. Nowadays most simulation codes and toolkits are evolved to such an extent that uncertainties of the orbital radiation models tend to limit the accuracy. Nevertheless, the treatment of soft proton scattering at grazing incidence angles, as it occurs for Wolter-type focusing X-ray mirrors, is still a matter of discussion. The problem of soft proton funneling has been discovered shortly after the launch of the *Chandra X-ray Observatory* [1] in 1999, when a surprisingly rapid degradation of the front-illuminated CCDs (charge coupled devices) of the *ACIS* instrument occurred [2]. Measurements with *XMM-Newton* [3], which was launched six months after *Chandra*, showed a soft proton flux more than a factor of three larger than expected from simulations [4]. In the following years, the scattering description for grazing angles by Firsov [5], which is based on the surface plasmon model, has been implemented in the GEANT4 toolkit[1] [6] to solve the discrepancy [7]. Nevertheless, experimental data with X-ray mirrors for validation are still rare. So far only one experiment, performed at the accelerator facility of the Harvard University, has been measuring soft proton scattering on X-ray mirrors [8, 9], but it was carried out under enormous time pressure between the discovery of the *Chandra* incident and the launch of *XMM-Newton*. Therefore, it covered only the parameter space that was relevant to assess possible degradation of the *XMM-Newton* instruments.

Since the scattering of soft protons from the orbital environment is an issue for future missions as well, the lack of experimental data has driven the construction of a new setup to measure grazing angle scattering efficiencies of soft protons over a wide range of parameters and, as a secondary goal, to determine the energy loss. It is based on a previous irradiation setup [10] that has been used to study the effects of soft proton radiation on detector prototypes for the *LOFT* (Large Observatory For x-ray Timing) space mission [11]. The intention of the scattering measurements is,

---

[1] http://geant4.cern.ch

on the one hand, to validate the application of the Firsov description to X-ray mirrors as well as the use of the TRIM code[2] [12] for this purpose and, on the other hand, to generate input parameters for a ray tracing code currently under development to simulate the propagation of soft protons through X-ray telescopes [13]. All results presented within this publication have been obtained with parts of spare mirror shells of the *eROSITA* (extended Roentgen Survey with an Imaging Telescope Array) instrument [14]. *eROSITA* features seven Wolter type-I X-ray telescopes, each consisting of 54 nested mirror shells. It is the main instrument of the *SRG* (Spectrum-Roentgen-Gamma) satellite, which is scheduled for a launch in 2016 and will be placed in an orbit around the Lagrangian point L2 of the Earth-Sun-system to perform an all-sky survey. Since it will be the first X-ray telescope operating at L2, where the (soft) proton flux has not been measured so far, it represents also a pathfinder for future X-ray missions at L2, e.g. *ATHENA* (Advanced Telescope for High-ENergy Astrophysics) [15].

A comprehensive description of the scattering experiment and the calibration methods is given in Section 2. In Section 3 the measurement procedure and parameters are explained, while the results are presented and discussed in Section 4. Section 5 concludes with a summary and an outlook on the application of the results as well as on future measurements.

2 Experimental setup

2.1 Accelerator facility

The scattering setup for grazing angles has been implemented at the ion accelerator facility of the University of Tübingen. The accelerator is a 3 MV single-ended Van de Graaff (HVEC KN-3000), capable of producing light ion beams in the energy range of 400 keV–2.5 MeV. The beam energy is determined by measuring the terminal voltage with a generating voltmeter (GVM) [16]. The GVM itself is calibrated via measuring the yield of resonant nuclear reactions and threshold reactions while scanning the terminal voltage [17]. The beam current is adjustable from a few nanoampere up to several tens of microampere.

The ions are produced in a radio frequency ion source within the high voltage terminal. An analyzing magnet bends the beam by 95° to remove contaminations from ionized residual gas and partially ionized molecules via momentum separation. This analyzer is also used to stabilize the terminal voltage on the 10^{-3} level by feeding back the beam position after the 95°-bend to the voltage regulation system.

The facility features six beam lines, selectable via a switching magnet. Various dipole magnets are distributed along the beam lines to bend and shift the beam. Two pairs of double quadrupole magnets per beam line allow to refocus the beam. An overview of the small angle scattering setup installed at the end of beam line 3 is given in Fig. 1.

---

[2]Part of the SRIM package; http://www.srim.org
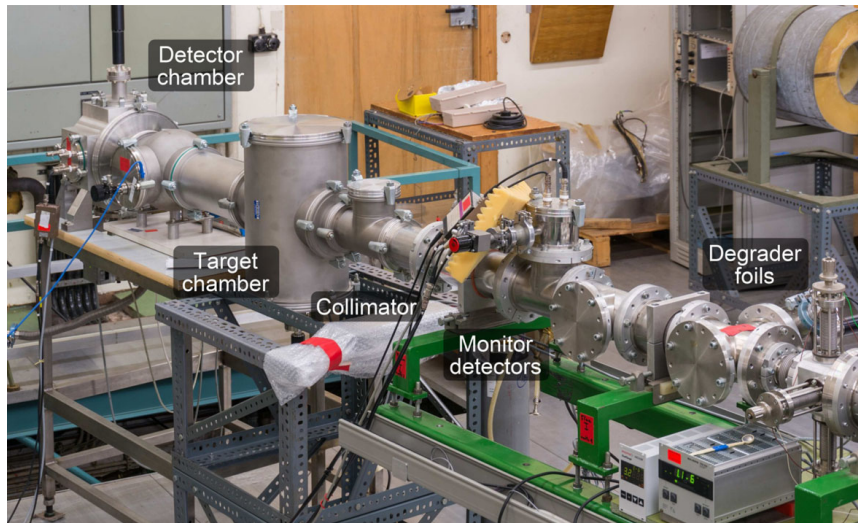
Fig. 1 Overview of the scattering experiment at beam line 3 of the accelerator facility of the University of Tübingen. The beam direction is from the right hand side, where the last slit is visible, through the collimator in the center to the detector chamber on the far left. The scattering target is mounted in the chamber downstream of the collimator. Degrader foils widen the beam spatially to provide flux to two detectors at the collimator entry, which monitor the incident proton flux

2.2 Beam line setup

A schematic of the setup is presented in Fig. 2, while the CAD model in cross-sectional view in Fig. 3 provides an insight into the implementation. Two angles are used in the following to describe the scattering geometry: the incidence angle Ψ, defined between mirror surface and incident beam, and the scattering angle Θ, which is the angle of the detector position with respect to the incident beam.

The proton beam enters the setup through a pair of slits, separated about 50 cm. Each of these slits consists of four adjustable copper parts that form a rectangular aperture. The individual parts are electrically isolated to allow the tapping of currents. The proton beam is well aligned with the setup when the currents on all opposite slit parts are equal.

A pinhole aperture reduces the incoming beam current and, therefore, the rates on the detectors. Depending on the actual measurement configuration, typical diameters are 0.1–1.0 mm to prevent excessive pile-up while keeping measurement durations reasonable. As well as all other apertures in the setup, the pinhole is made of copper and has a chamfer on the downstream side to minimize scattering inside the aperture. Different geometries have been studied by means of Monte Carlo simulations with the GEANT4 toolkit. The results have been incorporated in the actual design and can be found in [18].

The main experimental challenge is the determination of the incident particle flux during a scattering measurement. The beam intensity is subject to unavoidable fluctuations, which arise from variations of the terminal voltage and the yield of the ion source as well as, on longer timescales, from a drifting of the magnetic fields of the
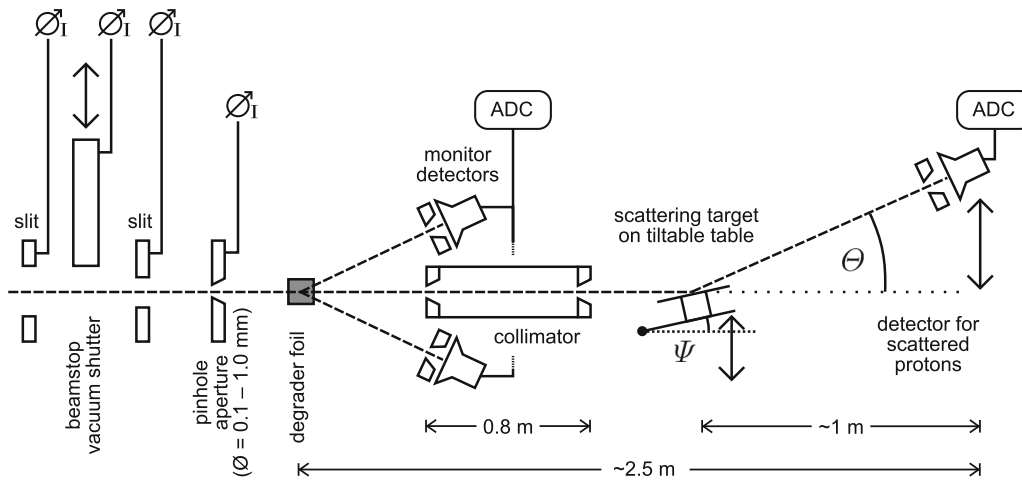
Fig. 2 Schematic of the small angle scattering setup. Two pairs of slits are used to verify the alignment of the proton beam with the setup. A pinhole aperture reduces the beam current and ensures a well-defined beam spot on the metal degrader foil. The foil spatially widens the beam to provide flux to the monitor detectors. A collimator focuses a part of the widened beam on the target, which is mounted on a tiltable table to allow a change of the incidence angle Ψ. The scattering angle Θ is defined by the position of the detector at the end of the beam line

bending magnets. In order to normalize the measured scattering rates, monitor detectors are placed peripheral to the beam. A metal degrader foil of a few micrometers thickness is mounted downstream of the pinhole aperture to widen the beam spatially, providing a constant fraction of flux to these detectors. The ratio of target flux to the readings of the monitor detectors is determined in dedicated measurements. Since the monitors are mounted relatively close to the degrader and the flux of the widened beam decreases with distance, rather small 60 μm apertures in front of the detectors limit the rate to restrict the pile-up fraction to about 1 %. The overall accuracy of determining the target flux via off-axis monitor detectors is estimated from different measurements to be within ±10 %. An additional advantage of the degrader
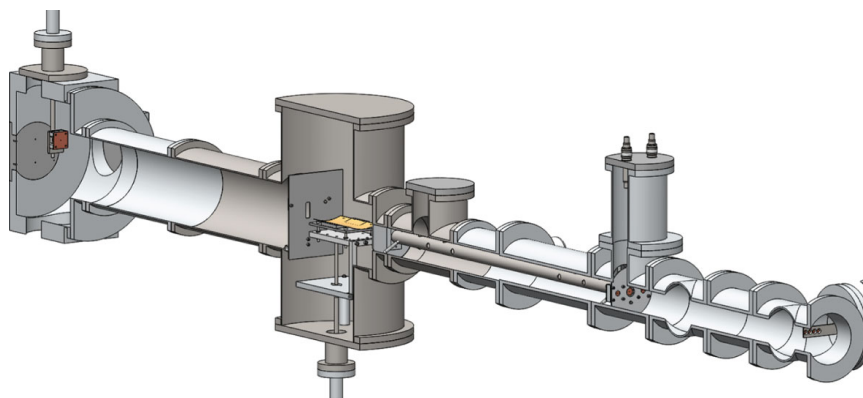
Fig. 3 A CAD model of the scattering setup in cross-sectional view showing, from right to left, the degrader foils on a movable holder, the collimator with the monitor detectors around the entrance, the tiltable target table, and the shiftable detector for scattered protons at the end of the beam line

foils is the reduction of the beam energy, which makes energies below the lower limit of the accelerator accessible, whereas the drawback is a spectral broadening up to a few tens of keV.

In between the monitor detectors the entrance of a 78 cm long collimator is located, which directs a part of the widened beam to the scattering target. During the measurements, aperture sizes of 1.0 mm at the entrance and 0.3 mm at the exit of the collimator have been used. This combination limits the maximum opening angle to 0.1° (1.7 mrad), providing a reasonable trade-off between transmitted flux and angular precision. The open space around the collimator tube is almost completely blocked at both ends with 2 mm aluminum plates to absorb bypassing protons that have been scattered at the inner walls of the beam line (cf. Fig. 4a). Instead of the second aluminum plate, a detector can be mounted temporarily on the exit of the collimator to determine the ratio of transmitted flux to the flux on the monitors in order to normalize the subsequent measurements (cf. Fig. 4d).

(a) Collimator exit   (b) Target mounting

(c) Shiftable detector   (d) Detector at the collimator exit
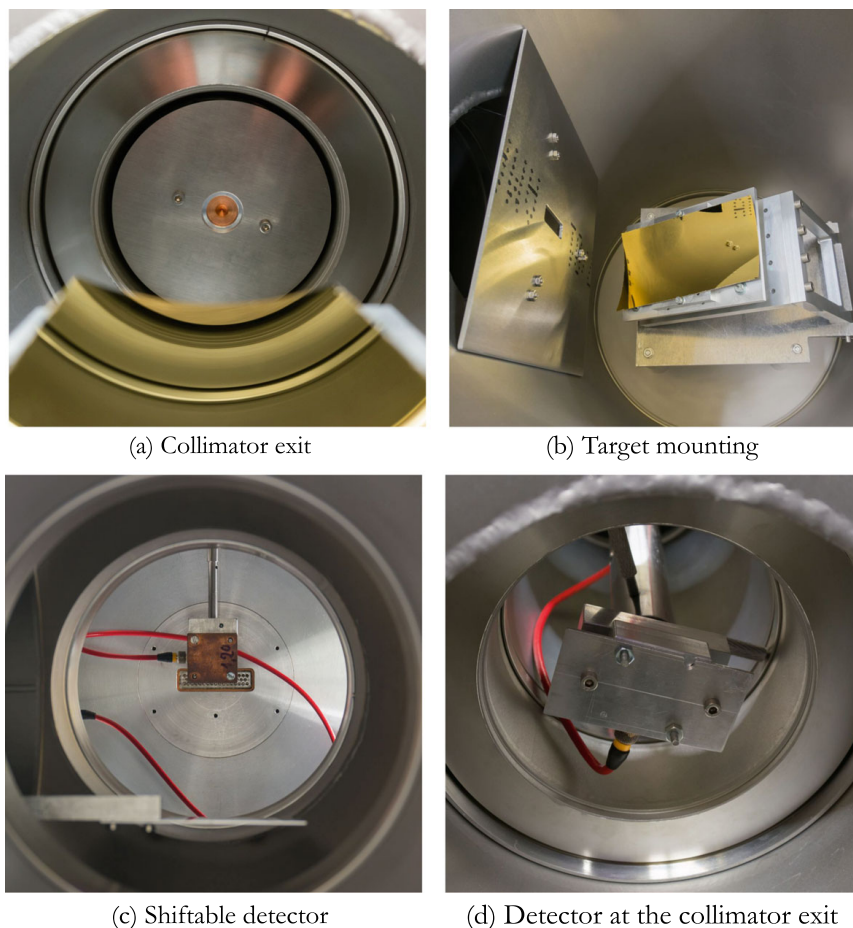
Fig. 4 From top left to bottom right: Close-ups of the collimator exit that is surrounded with an aluminum plate to absorb bypassing protons; the tiltable target table with a part of an *eROSITA* mirror shell and the aluminum sheet with a slit at the chamber exit, absorbing protons that have been scattered to larger angles; the movable detector for scattered protons at the end of the beam line; a detector mounted temporarily at the collimator exit to measure the transmitted proton flux

The scattering target, i.e. a part of an X-ray mirror shell, is mounted on a tiltable table with a length of 120 mm (cf. Fig. 4b). Its height can be regulated via setscrews to adapt to different mirror geometries and thicknesses. Since the mirrors are curved, they are fixed with two screws on movable wedges that support them sideways. The screws have been tightened with minimal force to avoid any deformation of the mirror. The tilt angle, i.e. the incidence angle Ψ, is controlled via a linear manipulator from below. The precision of the manipulator of 0.01 mm determines the theoretical precision of the tilt angle to 0.006° (0.1 mrad). The tilting axis is several centimeters below the beam, allowing to remove the target from the course of beam for a determination of the primary beam position on the detector plane.

An aluminum sheet to reduce the flux of protons, which have been scattered at the inner walls of the beam line, is installed downstream of the target chamber (cf. Fig. 4b). It leaves just a slit of 3 cm height and 1 cm width. A comparison of the proton background with and without this sheet shows a background reduction by about a factor of 50, which means a decisive increase of the signal to background ratio in a typical measurement scenario.

At a distance of 933 mm to the center of the target table a detector is mounted on a linear manipulator of the same type as used for the mirror tilting (cf. Fig. 4c). The detector is vertically shiftable up to 75 mm from the beam line center without shadowing effects, which corresponds to a maximal scattering angle Θ of about 4.5° (80 mrad). A 1.2 mm aperture defines the solid angle Ω to about 1.3 μsr with respect to the mirror center. The diameter of this aperture has been determined by means of an x-y-table with micrometer position accuracy and an attached microscope with cross-hairs; the error of this method has been estimated to ±0.1 mm.

2.3 Scattering targets

The mirror shells of the *eROSITA* telescope consist of nickel substrates with a 50 nm thick gold layer coated on the inner surface. This composition is quite similar to the *XMM-Newton* mirrors, except that their gold layer has a thickness of 150–200 nm. However, TRIM simulations conducted within this work showed that this difference does not affect the grazing angle proton scattering significantly. The substrate thicknesses of the *eROSITA* mirrors range from 540 μm for the outer shells to 200 μm for the inner ones. For the scattering measurements, two samples have been cut from an *eROSITA* spare mirror (shell 25, 270 μm substrate thickness) by means of a wire cutter. This method has been selected after the study of various alternatives because it leads to a minimum of debris particles on the samples and affects the gold coating only very close to the edges. The sizes of the samples differ slightly: the larger one has a trapezoid shape with a length of 12 cm (cf. Fig. 4b), the smaller one is almost rectangular with a length of about 10 cm. Although all results presented within this publication have been obtained with the larger sample, data from the smaller one have been used to cross-check for consistency.

The mirror samples have been handled with care to avoid damage or contamination of the surface and minimal strain has been applied for the mounting to prevent deformations. However, the samples have not been kept under clean room conditions;

dust particles on the surface have been removed regularly before closing the target chamber by spraying with nitrogen. A few small scratches have been present on the surface, but not in the central region where the proton beam has been scattered.

2.4 Proton detectors

Silicon surface barrier (SSB) detectors with 8 mm sensitive diameter are used for the detection of the scattered protons and as monitor detectors. These SSBs feature a detection efficiency of almost 100 % and an energy resolution around 10–20 keV. The maximal count rate is limited by the shaping time of the spectroscopic amplifiers; typically rates of up to $2 \cdot 10^5 \, \text{s}^{-1}$ can be achieved without sacrificing the spectral resolution.

The low energy threshold, above which proton events can be unambiguously identified, is defined by the thermal noise level and the level of electromagnetic noise that is picked up by the detectors and the readout electronics. Although noise levels well below 80 keV could be reached in the scattering setup, the trigger threshold has been set to about 100 keV to account for an increase at high rates.

The signals of all three detectors are digitized by a fourfold peak-sensing ADC (analog-to-digital converter). In order to correct for dead time, a pulser signal is split and input on the fourth ADC channel as well as on a scaler. The fraction of pulses registered by the ADC compared to the scaler value gives the conversion efficiency for all ADC channels.

An energy calibration of the SSBs has been performed in the scattering chamber of beam line 2 by measuring backscattered protons from different known targets. Before the calibration, the incident beam energy has been determined via the 992 keV resonance of the $^{27}\text{Al}(p, \gamma)^{28}\text{Si}$ reaction. The complete calibration procedure is described in detail in [10]; the accuracy is estimated to be within ± 10 keV.

2.5 Alignment and angular calibration

The alignment of all apertures in the course of beam, i.e. the slits, the pinhole aperture, and entrance and exit of the collimator, is performed with a theodolite that is placed behind the end of the beam line. In order to allow the alignment procedure, the detector chamber has a flange on the back side and all apertures can be removed.

As described in Section 2.2, the incidence angle Ψ and the scattering angle Θ are adjusted via linear manipulators, necessitating a conversion between the manipulator readings and the angles. The scattering angle can be calculated from the geometry of the setup, if the manipulator position corresponding to $\Theta = 0°$ is known, whereas the incidence angle needs to be calibrated. Furthermore, the entire incident flux encounters the mirror only within a certain range of incidence angles, depending on the height of the target table. The limits need to be determined, since a measurement of the scattering efficiency is only meaningful within this range.

Since the X-ray mirror targets reflect visible light and the SSB detector is sensitive to it as well, a 445 nm solid-state laser is used for the calibration. The device is sufficiently compact to be inserted into the beam line after the pinhole. The position and orientation of the laser is adjusted via setscrews until the transmitted intensity through

the collimator is maximized. After the $\Theta = 0°$ position of the detector is determined, the mirror is shifted in the course of beam. The position at which the primary beam is completely blocked corresponds to the minimal incidence angle. Successively, the tilt of the mirror is increased and the position of the reflected beam measured with the detector. The corresponding angles are calculated via the condition $\Psi = \Theta/2$ for specular reflection. During the calibration, the proper positioning of the mirror is checked as well. Therefore, the measured laser intensity is observed while slightly shifting the detector perpendicular to the manipulator direction. If the mirror surface, where the beam is reflected, is not aligned perpendicular to the manipulator direction, the reflected laser spot drifts away from the detector with increasing incidence angle. In this case, the mirror position is changed accordingly and the calibration procedure is repeated. This procedure has been iterated until any observable drift has vanished.

As an example, laser calibration data for one of the *eROSITA* mirror samples is shown in Fig. 5. The first data point at a mirror manipulator position of 66.0 mm marks the point at which the mirror blocks completely the primary laser beam. There-after, the correlation with the detector position is linear up to a manipulator reading of 66.7 cm, where a shift of the reflected beam is visible. This shift appears because the beam starts to hit the front of the mirror sample and marks the maximal mirror angle for this setting.

3 Measurement parameters and procedures

3.1 Proton energies and spectra

Three proton energies have been selected for the scattering measurements: 250 keV, 500 keV, and 1 MeV. This range covers, as far as experimental constraints allow, the
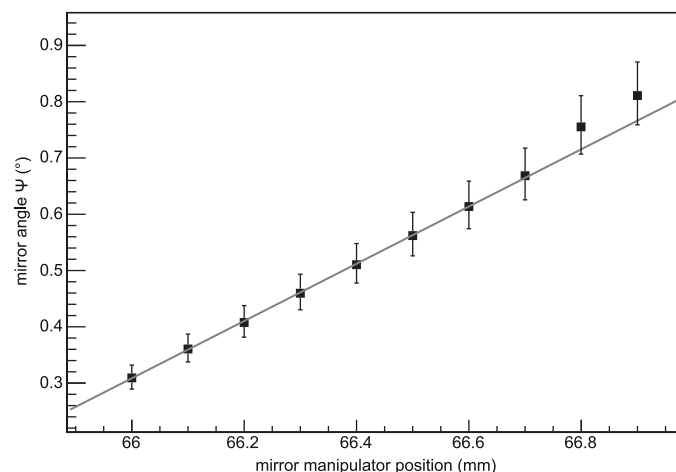
Fig. 5 Plot of the laser calibration data for one of the *eROSITA* mirror samples. The grey line is a linear fit to the data from 66.0 to 66.7 mm. The points of larger positions are shifted because the incident beam hits the front of the mirror sample. This marks the maximal incidence angle for a meaningful measurement of the scattering efficiency

energies for which an enhanced funneling efficiency has been measured in orbit. Energies lower than 250 keV are not reasonable in the current setup considering the 100 keV detection threshold of the SSBs and a possible energy loss of several tens of keV. Combinations of initial beam energy, degrader material, and foil thickness to obtain the mentioned energies are derived from simulations by means of the TRIM code. Table 1 lists the combinations finally used, together with mean energy and FWHM that have been derived by fitting a Gaussian to the main part of the measured spectra (cf. Fig. 6). The Gaussian shape arises from straggling in the degrader foil and, to a smaller extend, from the finite energy resolution of the SSB detector. The low energy tails visible in the 500 keV and 1 MeV spectra are mostly due to slit scattering and contain at maximum 1 % of the total flux. Dedicated low flux measurements with a smaller pinhole aperture show that up to about 5 % of the counts in a spectrum of the incident beam are pile-up; a high energy tail above the Gaussian peak is not present in the data. Since pile-up is unavoidable when detecting the incident beam directly under typical measurement conditions, an energy threshold cut has been applied and all recorded events above the threshold have been counted twice. The same procedure has been applied in the analysis of the scattering data.

Although the mean energy incident on the target E_{inc} shifts within ± 20 keV between individual measurements, the nominal energies are given in the following for the sake of convenience. The deviation does not affect the results of the efficiency measurements; in the analysis of the energy loss it has been accounted for.
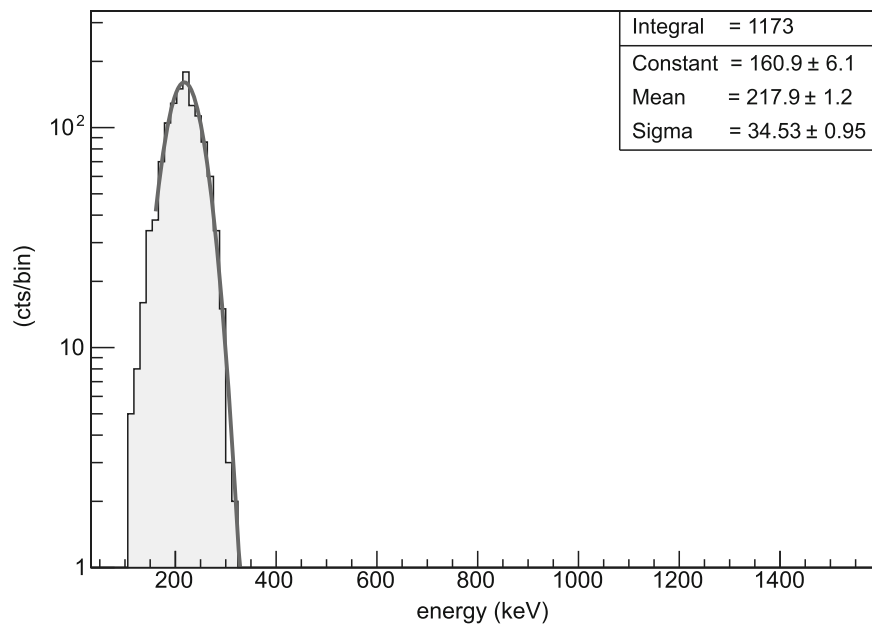
3.2 Scattered proton spectra

Examples of scattered proton spectra at mean incidence and scattering angles are given in Figs. 7, 8 and 9 for the three incident energies. Almost all acquired spectra contain at least 1000 counts. While for the calculation of the scattering efficiency only the integrals have been considered, Gaussians have been fitted to determine the position of the main peak for a calculation of the mean energy loss ΔE by a comparison with the incident spectrum. In order to account for a possible drift of the primary beam energy, the incident spectra have been measured frequently during a set of measurements.

Table 1 List of the beam energy and degrader combinations used for the scattering measurements. The spectral parameters of the exiting beam have been determined by fitting Gaussians to the main part of the measured spectra (cf. Fig. 6)

Beam energy (keV)	Degrader material and thickness	Mean energy (keV)	FWHM (keV)
1030	6 μm Cu	245	76
1180	6 μm Cu	477	70
1550	6 μm Cu	977	64
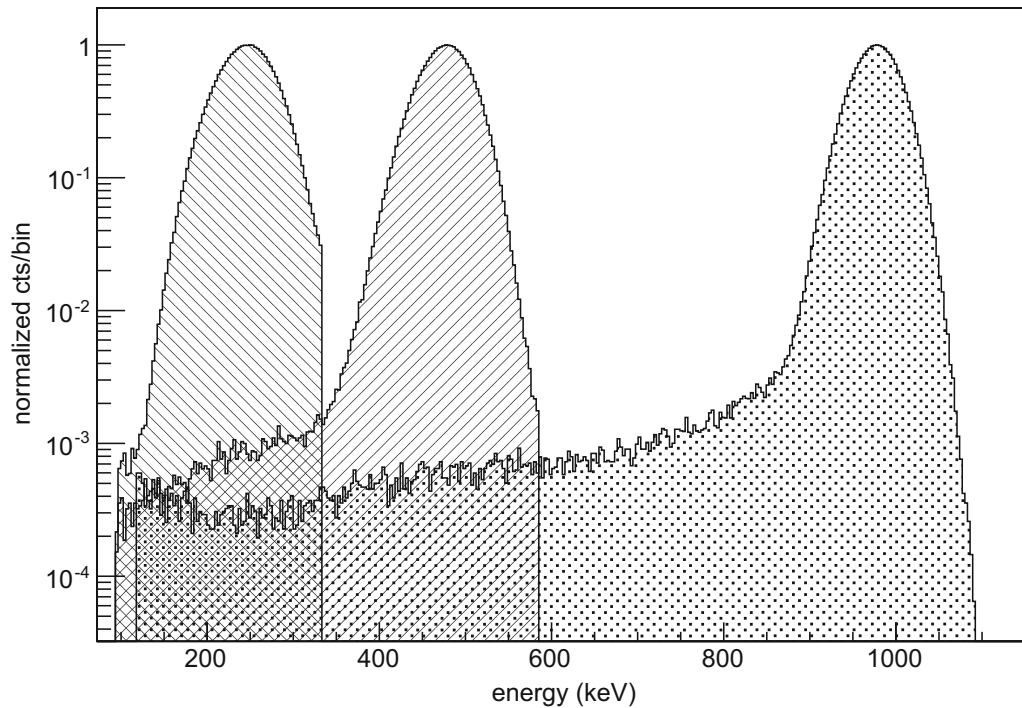
Fig. 6 Overlay of the incident proton spectra, recorded with the detector at the end of the beam line. The spectra are centered around 245 keV, 477 keV, and 977 keV. The low energy tails are mostly due to slit scattering. Pile-up has been removed by applying an energy threshold cut

Fig. 7 Spectrum of scattered protons for $E_{inc} = 246.7$ keV, incidence angle $\Psi = 0.67° \pm 0.11°$, and scattering angle $\Theta = 1.67° \pm 0.11°$. The mean energy loss has been determined by fitting a Gaussian to the main peak (grey line) and comparing the position with a Gaussian fit to the incident spectrum

Integral =	1189
Constant =	161.8 ± 6.0
Mean =	457.4 ± 1.1
Sigma =	34.92 ± 0.90
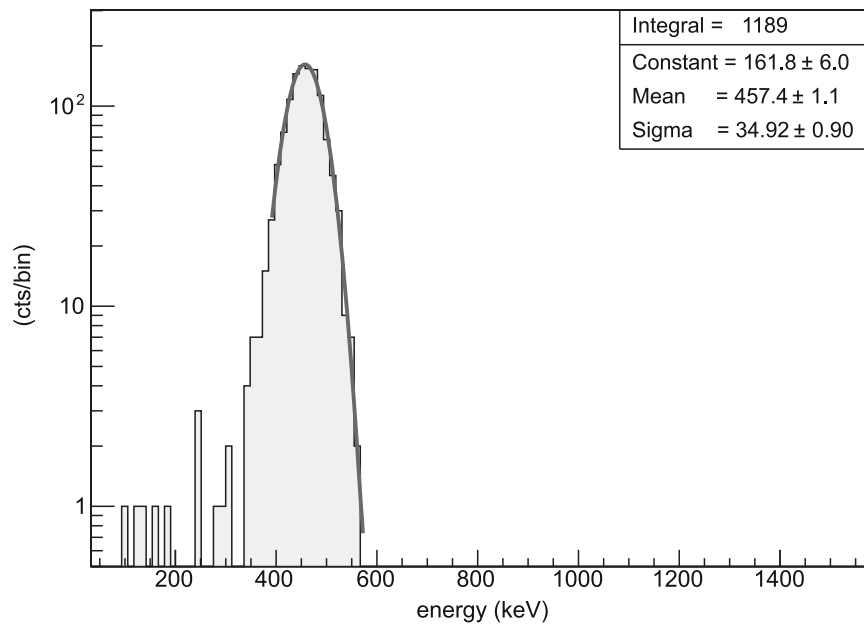
**Fig. 8** Same as Fig. 7, but for $E_{inc} = 492.9$ keV, $\Psi = 0.64° \pm 0.12°$, and $\Theta = 1.64° \pm 0.11°$

3.3 Beam direction and incident flux

The position of the incident proton beam at the detector plane varies on the order 0.5–1 mm between sets of measurements, when the beam has been set up newly, and deviates up to 1.5 mm from the position measured during the laser calibration.


Integral =	1472
Constant =	226.2 ± 7.6
Mean =	929.2 ± 0.8
Sigma =	29.87 ± 0.64
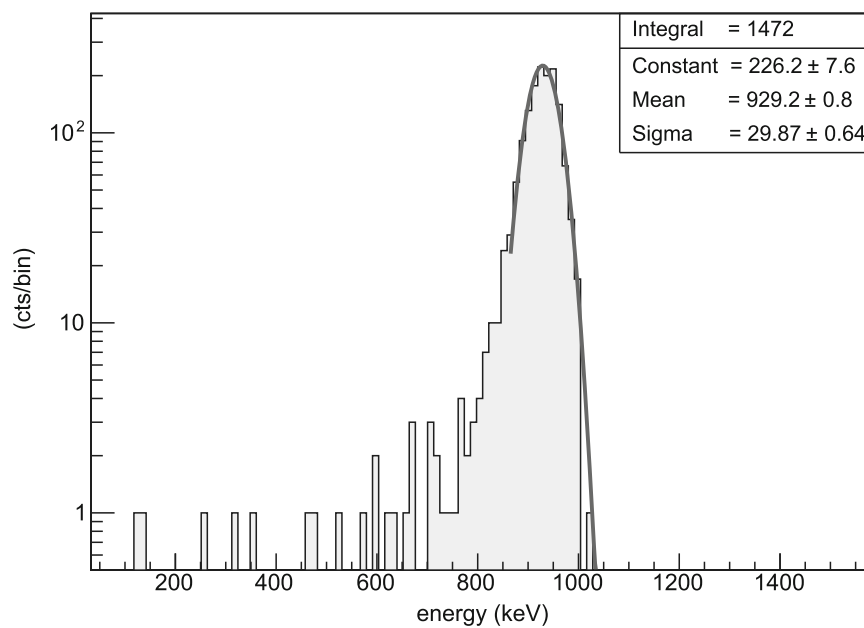
Fig. 9 Same as Fig. 7, but for $E_{inc} = 968.4$ keV, $\Psi = 0.61° \pm 0.15°$, and $\Theta = 1.61° \pm 0.10°$

Therefore, the mirror has been tilted out of the course of beam at the beginning of each set and the flux at different position close to the primary beam ($\Theta = 0°$) has been measured. The primary beam position has been derived from this data via fitting with a function that describes the overlapping area of two circles with different radii in dependence of the distance of the circle centers. Data of such a measurement and its good agreement with the theoretical description is shown in Fig. 10. The actual primary beam position has been considered in the final calculation of both angles, Ψ and Θ.

The variation of the direction of the incident proton beam impedes the determination of the incident flux from the measurement at the primary beam position, since the deviation is of the order of the diameter of the detector aperture and the detector can only be moved vertically. As an alternative, a detector has temporarily been mounted at the collimator exit to determine the transmitted proton flux (cf. Fig. 4d). A normalization parameter has been derived from this measurement, which associates the measured flux on the monitor detectors to the incident flux on the target. Since the widening of the beam by the degrader foils is energy dependent, this measurement has been repeated for all energies used. All measured fluxes have been normalized to the mean flux of the two monitor detectors. The uncertainty for the incident flux on the target by applying this method has been estimated to $\pm 10\,\%$.

Furthermore, the proton background at each of the measured scattering angles has been determined while the mirror has been tilted out of the course of beam. Background arises because protons scatter at the exit aperture of the collimator and hit – either directly or via a second small angle scatter on the inner beam line wall – the
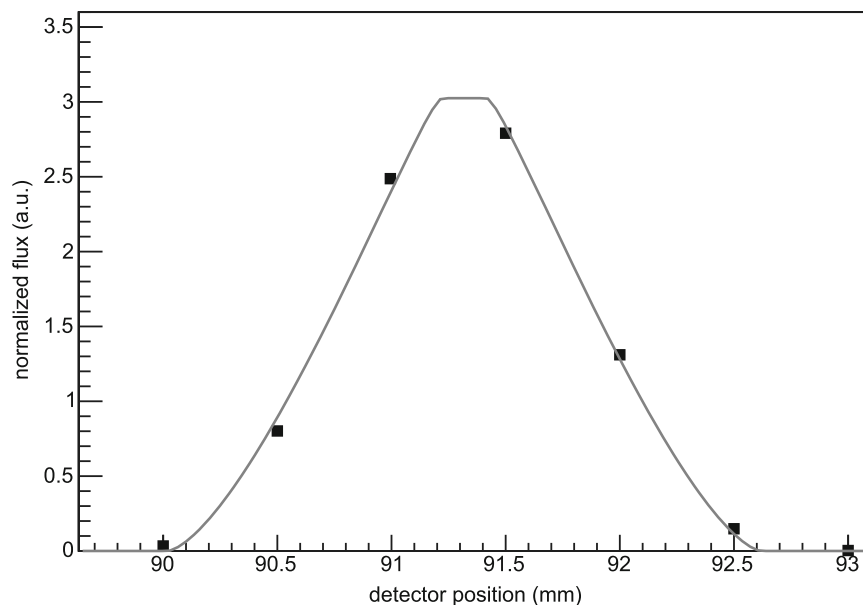
Fig. 10 Plot of the proton flux around the primary beam position ($\Theta = 0°$). The mirror has been tilted out of the course of beam for this measurement. A function that describes the area of two partially overlapping circles has been fitted to the data (grey line)

detector. The background contribution is on the order of a few percent and has been subtracted during the analysis of the scattering efficiency.

3.4 Angular coverage

The intention of the measurements is to cover the angles relevant for the assessment of the proton funneling to the focal plane of Wolter type-I mirror assemblies, which in principle comprises incidence angles in the range 0°–90°. Nevertheless, since the efficiency drops significantly towards larger incidence angles, the measurements have been focused on grazing incidence angles. The minimal feasible mirror angle in the experiment is about 0.3°, therefore incidence angles between this lower limit and 1.2° have been investigated in combination with scattering angles in the range 0.5° to 4.1°.

4 Results and discussion

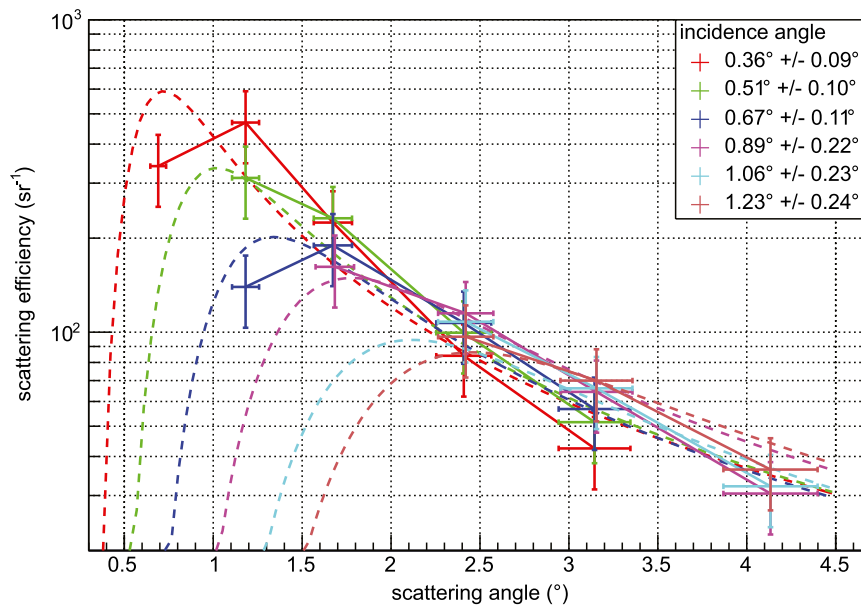### 4.1 Scattering efficiency

The differential scattering efficiency η is calculated according to Eq. 1 by dividing the detected number of protons N_{det} for a specific incidence angle Ψ and scattering angle Θ by the number of incident protons N_{inc} on the target mirror. The result has been normalized to the solid angle Ω of the detector, considering the dependence on Θ.

$$\eta(\Psi, \Theta) = \frac{\Phi_{\mathrm{det}}(\Psi, \Theta)}{\Phi_{\mathrm{inc}}} \frac{1}{d\Omega} = \frac{N_{\mathrm{det}}(\Psi, \Theta)}{N_{\mathrm{inc}}} \frac{1}{\Omega(\Theta)} \qquad (1)$$

The experimentally determined scattering efficiencies for the three incident energies E_{inc} are presented in Figs. 11, 12 and 13. The data have been acquired with two different settings of the target mirror, one optimized for $\Psi < 0.7°$, the other for $\Psi > 0.7°$. As the mirror bulk is shielding the detector for $\Psi > \Theta$, these data points are compatible with zero and, therefore, have not been plotted.

The errors for the scattering efficiency shown in the plots comprise counting statistics (effect on efficiency < 5 %), the estimated uncertainties of the effective detector area (19 % in excess and 15 % in deficit) as well as of the incident flux determination by using the peripheral monitor detectors ($\sim \pm 10$ %), the calibration and mechanical accuracy of incidence and scattering angles, and the uncertainty of the distance between the detector and the actual scattering position on the mirror (12 % in excess and 15 % in deficit). The latter dominates the angular error and causes the increase towards larger scattering angles because – besides the inevitable extension of the beam spot to several centimeters – the position of the spot on the 12 cm long target cannot be localized.

In order to check for systematic effects introduced by the mirror mounting and the laser calibration procedure, the measurements for $\Theta < 0.7°$ have been repeated twice: once with the same mirror mounted reversely and once with the second mirror sample (cf. Section 2.3). The data of all three measurements are consistent within the given errors.

Fig. 11 Scattering efficiency results for $E_{inc} = 250\,keV$. The values are normalized to the solid angle of the detector. The given errors account for counting statistics as well as uncertainties of the solid angle and the incidence and scattering angles. The individual data points for each incidence angle are connected by straight lines. The dashed lines are calculated by means of the Firsov formula (cf. Section 4.3)

The results show slightly higher efficiencies for larger incident energies. Table 2 lists the maximum measured efficiency $\hat{\eta}$ and the corresponding scattering angle for each incident energy and incidence angle. The maximum is in all measurements found around $\Theta = 2\Psi$, the condition for specular reflection.
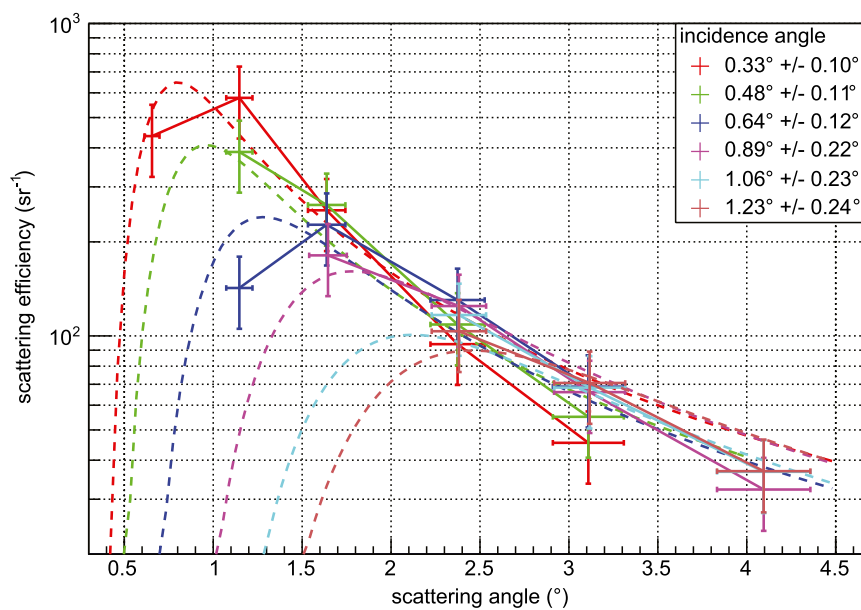
Fig. 12 Same as Fig. 11, but for $E_{inc} = 500\,keV$
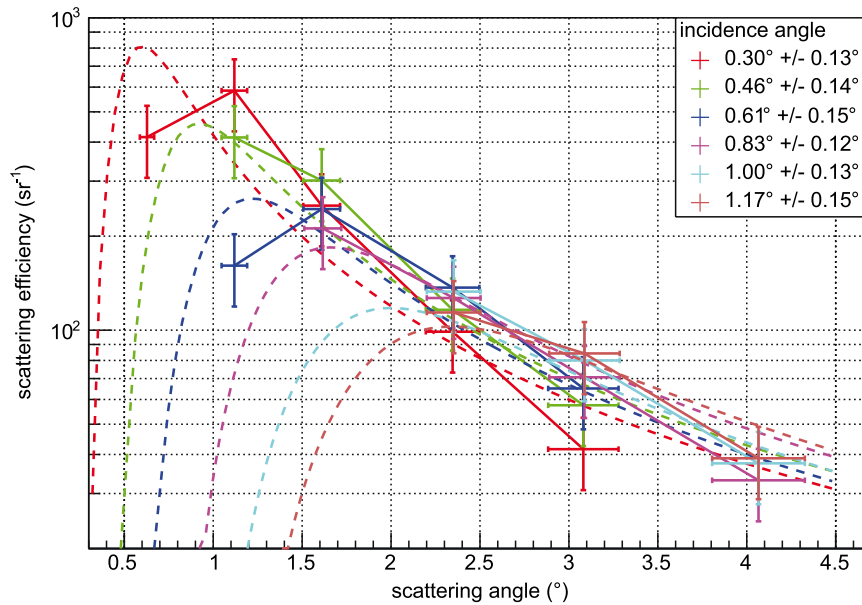
Fig. 13 Same as Fig. 11, but for $E_{inc} = 1\,\text{MeV}$

These results deviate from the findings in [8] for *XMM-Newton* mirrors, only the present data for 250 keV are in agreement with the reported efficiencies for $E_{inc} = 300\,\text{keV}$. For 500 keV the efficiencies of the present study are almost a factor of two higher; a comparison of the present 1 MeV measurement to the reported 1.3 MeV *XMM-Newton* data yields an even larger discrepancy around a factor of three and four. However, it should be stated that only six data points could be compared directly. The target mirrors and the experimental setups are comparable, except for the method of determining the incident flux, which might explain at least partially the systematically lower efficiencies of the former results towards higher energies: the current on the target mirror in the *XMM-Newton* setup has been integrated with an electrometer; from the collected charge the number of incident protons has been

Table 2 For each incidence angle Ψ and incident energy E_{inc}, the maximum efficiency $\hat{\eta}$ and the corresponding scattering angle Θ is listed. Since incidence and scattering angle deviate slightly between individual measurements, the mean values are given

| Ψ_{mean} (°)	Θ_{mean} (°)	$\hat{\eta}_{250\,keV}$ (sr^{-1})	$\hat{\eta}_{500\,keV}$ (sr^{-1})	$\hat{\eta}_{1\,MeV}$ (sr^{-1})
0.33	1.15	469 ± 122	578 ± 150	585 ± 152
0.48	1.15	312 ± 81	388 ± 101	414 ± 107
0.64	1.64	190 ± 49	227 ± 59	244 ± 63
0.86	1.65	162 ± 42	181 ± 47	212 ± 55
1.03	2.38	108 ± 28	117 ± 30	133 ± 35
1.20	2.38	97 ± 25	104 ± 27	114 ± 30

calculated. Although the emission of secondary electrons from the target has been reduced with a repulsion grid, the yield of these delta electrons is increasing with rising beam energy, possibly leading to an overestimation of the collected charge at higher energies and, therefore, to apparently lower efficiencies.
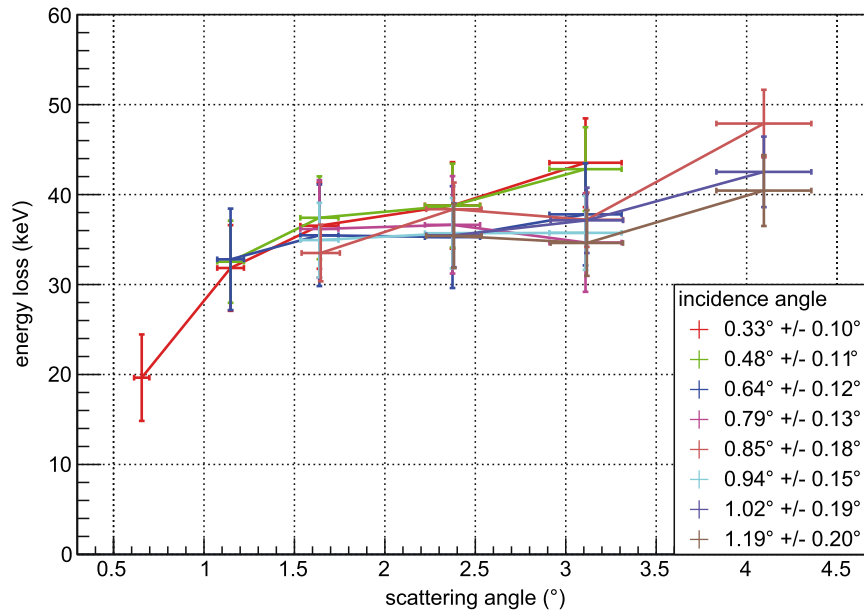
4.2 Energy loss

The results of the energy loss analysis is presented in Figs. 14, 15 and 16. The plots show the most probable energy loss ΔE, which is derived from Gaussian fits of the main peaks of the incident and the scattered spectra. Since shifts of the beam energy of a few keV can occur during the measurements, the incident spectrum has been measured immediately before and after each set of scattering measurements. The mean of these has been used as incident energy, from which the peak energy of the scattered spectra has been subtracted. For the calculation of the errors the deviation of the energy before and after the measurement as well as the errors of the fits have been considered. The former is dominating the errors, especially in the measurement around 250 keV. The angular errors have been derived as described in Section 4.1.

Since the Firsov scattering description makes no assumption of the energy loss, a narrow Gaussian distribution around 3 keV, independent of the incident energy has been used as default value in the implementation of the Firsov process in GEANT4. This assumption originates from high precision experimental data of grazing incidence proton scattering on a planar aluminum surface [19]. However, the present results for the gold coated *eROSITA* mirrors indicate significant higher losses: from
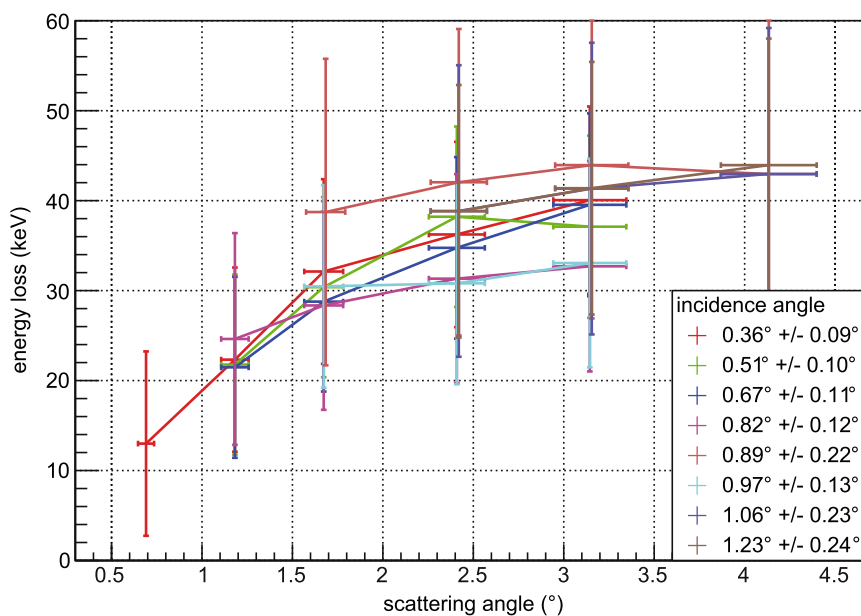
Fig. 14 Most probable energy loss for $E_{inc} = 250$ keV. The values have been calculated by subtracting the mean energy of the scattered spectra from the incident energy. All these values have been obtained by Gaussian fits to the main peak of the spectra. The individual data points for each incidence angle are connected by straight lines

Fig. 15 Same as Fig. 14, but for $E_{inc} = 500$ keV

13 keV for $\Theta = 0.69°$ and $E_{inc} = 250$ keV up to 54 keV for $\Theta = 3.09°$ and 1 MeV. It can be concluded that the most probable energy loss depends on the incident energy, similar to the results obtained with graphite targets reported in [20]. Furthermore, the data show a significant increase of the energy loss towards larger scattering angles, while being independent of the incident angle. An explanation for the discrepancy among the experimental results is first of all the different target materials as well as
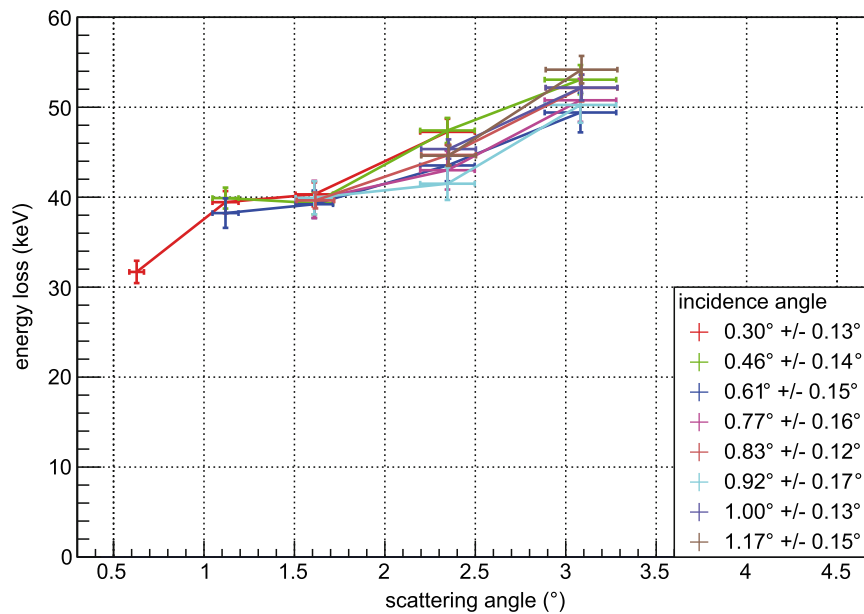
Fig. 16 Same as Fig. 14, but for $E_{inc} = 1$ MeV
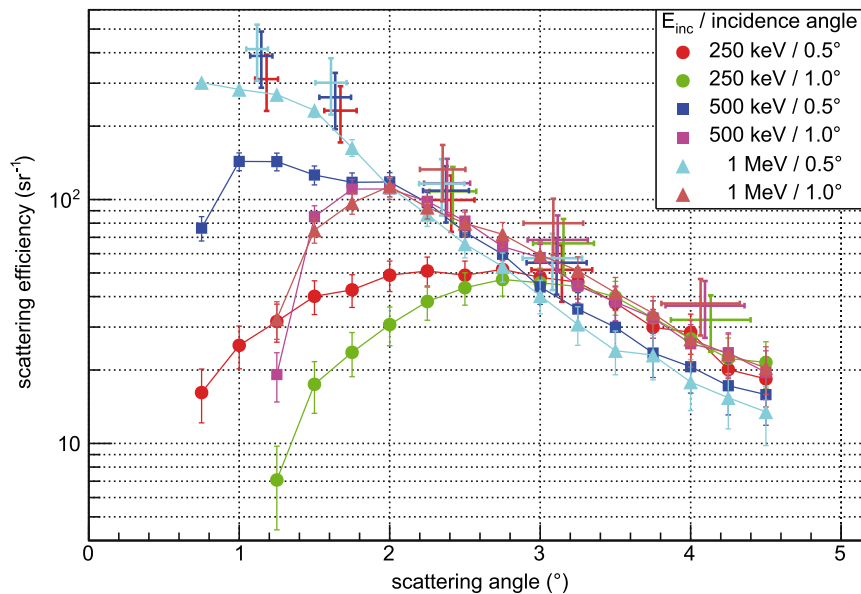
Fig. 17 Scattering efficiency results of TRIM simulations, each with 10 million protons. Angular cuts and an energy cut below 100 keV have been applied to match the acceptance angle and the energy threshold of the detector in the experimental setup. The individual data points of one parameter set are connected by straight lines. Included are the experimental data points of the measurement sets that correspond best to the parameters of the simulations (drawn in the respective color)

different surface conditions of the mirror samples used in the present study compared to the extensively prepared graphite and aluminum targets, which feature a clearly defined crystal orientation and flatness on an atomic level without contamination from adsorbed gases.

4.3 Comparison to the Firsov description and simulations

The theoretical scattering description by Firsov [5] (cf. Eq. 2)[3], which has been implemented in GEANT4 [7], predicts scattering distributions for grazing angle proton scattering that are shifted to smaller scattering angles in comparison to the GEANT4 multiple scattering process; the Firsov distributions peak at scattering angles that meet the condition for specular reflection ($\Theta = 2\Psi$). In order to compare the experimental data of the present study to the Firsov formula, the integral of the measured distributions from $\Theta = \Psi$, where zero efficiency has been assumed, to the largest scattering angle in the measurement has been estimated by a linear interpolation between the data points. The dashed curves in Figs. 11, 12 and 13 have been calculated by normalizing the integral of the Firsov curve for the particular incidence angle to the integral of the respective measurement, thereby equalizing the integral scattering efficiency in the considered range of scattering angles. The agreement with the experimental data is reasonable, considering that the mirror surface is not

---

[3]The scattering angle has been transformed to match the convention used in this study.

ideal, the uncertainties of the measurement, and the linear interpolation used for the comparison. However, the measured peak efficiencies are slightly shifted to larger scattering angles and the slope for larger scattering angles is steeper in the data than predicted by the formula. This should be taken into account in simulations of the proton propagation through an X-ray telescope, where two scatters can occur.

$$\epsilon(\Psi, \Theta) = \frac{3(\Psi(\Theta - \Psi))^{3/2}}{2\pi\Psi(\Psi^3 + (\Theta - \Psi)^3)} \tag{2}$$

The data have been compared to TRIM simulations. Therefore, the scattering of 10 million protons on a flat target, consisting of a 50 nm gold layer on a nickel substrate, has been simulated for each of the three incident energies by using incidence angles of 0.5° and 1.0°, respectively. Angular cuts and an energy cut at 100 keV have been applied to the simulation output to match the acceptance angle and the energy threshold of the detector in the experimental setup. The results for the scattering efficiency are shown in Fig. 17. TRIM reproduces the experimental data for the larger scattering angles, except for a slight systematic shift to lower efficiencies. Nevertheless, below a certain scattering angle the simulated efficiencies drop significantly with respect to the experimental data. For 500 keV incident energy the threshold is around a scattering angle of 2°, for 250 keV around 3°. Just the simulation for 1 MeV and an incidence angle of 0.5° is in agreement with the data down to a scattering
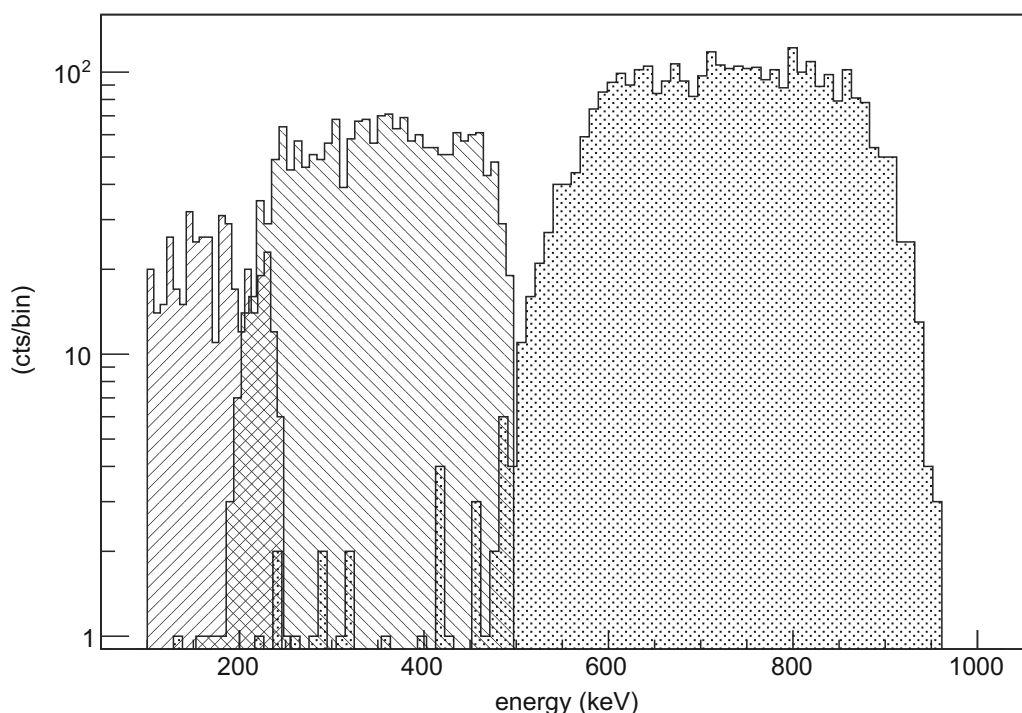
Fig. 18 Proton spectra after scattering obtained by means of TRIM simulations. From left to right the incidence energy is 250 keV, 500 keV, and 1 MeV, respectively. The incidence angle is 0.5°, the scattering angle 2°. Angular cuts and an energy cut below 100 keV have been applied to match the acceptance angle and the energy threshold of the detector in the experimental setup
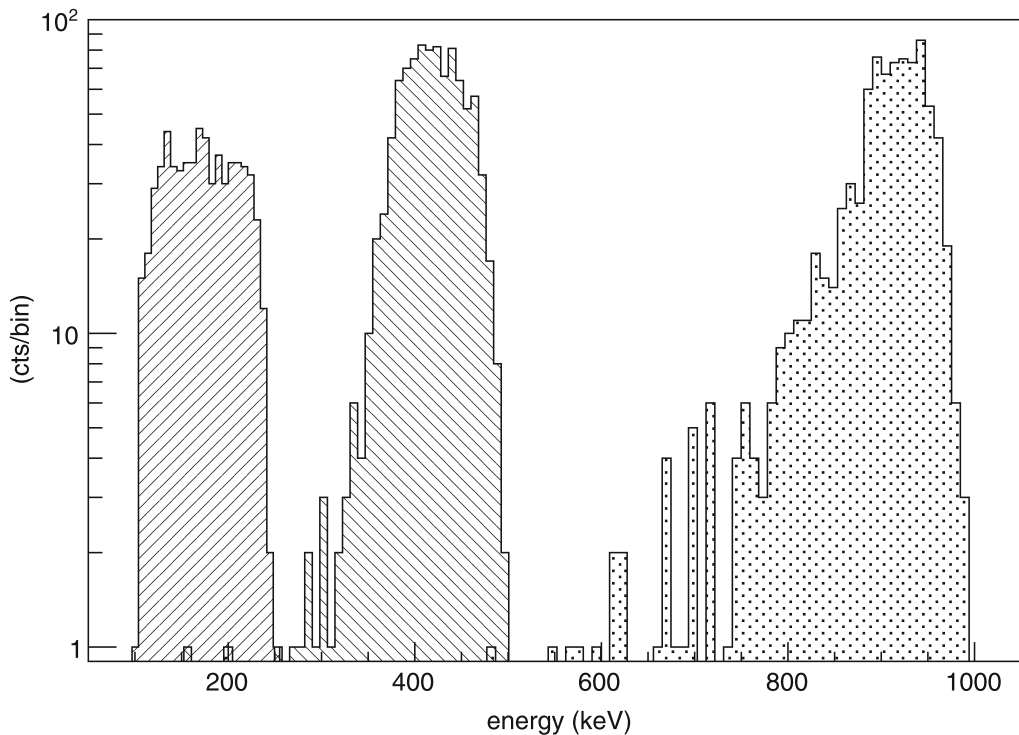
Fig. 19 Same as Fig. 18, but for $\Psi = 1.0°$

angle of 1°. Furthermore, the TRIM output shows significantly larger energy losses and broader distributions than the measured data. As shown in Figs. 18 and 19, this is more pronounced for smaller incidence angles. The broad energy loss distribution accounts partially for the low efficiencies at 250 keV, since a part of the scattered spectrum is affected by the 100 keV energy cut.

Since the compositions of the *eROSITA* and the *XMM-Newton* mirrors are almost identical, the measured efficiencies have also been compared to the GEANT4 results reported in [9]. In general, the simulation results show smaller efficiencies than the current experiment; deviations up to a factor of two occur in particular for large incidence angles, while for smaller incidence and larger scattering angles the results agree within the errors. Even though this behavior appears to be similar to the TRIM results discussed before, the overlap in parameter space is too small to allow significant conclusions.

5 Conclusions

The scattering setup presented in this work applies a unique method of determining the incident proton flux on the target via monitor detectors, enabling high accuracy efficiency measurements of grazing incidence scattering. The current data obtained with samples of *eROSITA* mirror shells show significant higher efficiencies compared to previous measurements with *XMM-Newton* mirrors at the Harvard University in

1999 [8]. An explanation, at least for a part of the discrepancy, could be the different methods for the determination of the incident flux.

The use of an energy degrader foil, which leads to a spectral broadening, and the moderate energy resolution of the SSB detectors limit the precision of energy loss measurements with the present setup. However, since the measured mean energy loss is more than one order of magnitude larger than estimated in [7], the deviation is significant.

It can be concluded that the scattering distributions of the present study are reasonably reproduced by the Firsov formula. However, a small systematic shift of the measured peak efficiencies to larger scattering angles and a steeper slope of the experimental data has been found. These deviations might be attributed to the non-ideal finite surface roughness of the mirror shells and a combination of Firsov scattering with other scattering processes, e.g. multiple scattering, might yield a more accurate description. If incident energies and scattering angles are sufficiently large, simulations by means of the TRIM code are in good agreement with the measured data. The lower thresholds for the applicability of TRIM for efficiency simulations are around a scattering angle of 3° for 250 keV incident energy and at about 2° for 500 keV and 1 MeV. For 1 MeV incident energy and an incidence angle of 0.5° the agreement between simulation and measurement extends even down to scattering angles of 1°. However, for all energies and angles studied within this work the energy loss in the simulation is larger and broader distributed than in the experimental results. As for the efficiencies, the deviation is decreasing with increasing energy and angles.

Future applications of the setup are grazing angle scattering measurements with different target materials that are used for X-ray mirror coatings as well, e.g. iridium, and aluminum for a comparison with a light target material. Additionally, measurements with alpha particles are planned. The results of this work will be incorporated in a ray tracing simulation code for protons that is currently under development in a collaboration of the IASF[4] in Palermo, the IAA[5] Tübingen, and the MPE[6] in Garching [13]. It is dedicated to the simulation of proton propagation through X-ray telescopes for the assessment of potential damage and proton induced background in future X-ray missions, such as *eROSITA* and *ATHENA*.

Conflict of interests   The authors declare that they have no conflict of interests.

---

[4]Istituto di Astrofisica Spaziale e Fisica Cosmica

[5]Institute for Astronomy and Astrophysics

[6]Max Planck Institute for Extraterrestrial Physics

References

1. Weisskopf, M.C. et al.: An overview of the performance and scientific results from the chandra X-Ray Observatory. PASP **114**(791), 1–24 (2002)
2. Lo, D.H., Srour, J.R.: Modeling of proton-induced CCD degradation in the Chandra X-ray observatory. IEEE Trans. Nucl. Sci. **50**(6), 2018–2023 (2003)
3. Jansen, F. et al.: XMM-newton observatory I. The spacecraft and operations. A&A **365**, L1–L6 (2002)
4. Kendziorra, E. et al.: The effect of low energy protons on the performance of the EPIC pn-CCD detector on XMM-newton. Proc. SPIE **4140**, 32–41 (2000)
5. Firsov, O.B.: Reflection of fast ions from a dense medium at glancing angles. Sov. Phys.-Doklady **11**(8), 732–733 (1967)
6. Agostinelli, S. et al.: Geant4 – a simulation toolkit. Nucl. Instrum. Methods Phys. Res., Sect. A **506**, 250–303 (2003)
7. Lei, F. et al.: Update on the use of Geant4 for the Simulation of low-energy protons scattering off X-ray mirrors at grazing incidence angles. IEEE Trans. Nucl. Sci. **51**(6), 3408–3412 (2004)
8. Rasmussen, A. et al.: Proton scattering off of XMM optics: XMM mirror and RGS grating samples, XMM Document RGS-COL-CAL-99009, Columbia Astrophysics Laboratory (1999)
9. Nartallo, R. et al.: Radiation environment induced degradation on chandra and implications for XMM, ESA Report (2000)
10. Diebold, S. et al.: A setup for soft proton irradiation of X-ray detectors for future astronomical space missions. Nucl. Instrum. Methods Phys. Res., Sect. A **721**, 65–72 (2013)
11. Feroci, M. et al.: The large observatory for x-ray timing. Proc. SPIE **9144**, 9144–100 (2014)
12. Ziegler, J.F. et al.: SRIM – The stopping and range of ions in matter. Nucl. Instrum. Methods Phys. Res., Sect. B **268**, 1818–1823 (2010)
13. Perinati, E. et al.: Analysis of proton propagation through the eROSITA telescope. Proc. SPIE **9144**, 9144–190 (2014)
14. Predehl, P. et al.: eROSITA on SRG. Proc. SPIE **9144**, 9144–64 (2014)
15. Nandra, K. et al.: Athena: exploring the hot and energetic universe. Proc. SPIE **9144**, 9144–84 (2014)
16. Brown, R.B. et al.: Precision ion beam energy measurement of a Van de Graaff accelerator using a generating voltmeter. Nucl. Instrum. Methods **151**, 377–380 (1978)
17. Kump, P. et al.: An absolute calibration of electrostatic accelerators in the energy region from 0.7 MeV to 2.1 MeV. Nucl. Instrum. Methods **112**, 489–494 (1973)
18. Diebold, S. et al.: A facility for soft proton irradiation and instrument testing for future space missions. IEEE Trans. Nucl. Sci. **61**(4), 1937–1942 (2014)
19. Winter, H. et al.: Energy loss of fast protons in grazing scattering from an Al(111)-surface. Nucl. Instrum. Methods Phys. Res., Sect. B **125**, 124–127 (1997)
20. Pfandzelter, R. et al.: Probing the stopping power near the surface by specular reflection of protons from graphite. Nucl. Instrum. Methods Phys. Res., Sect. B **72**, 163–175 (1997)

6 Conclusions

The opacity of the Earth atmosphere makes spaceborne observatories crucial for astronomical studies in the UV and X-ray domains. The UV band is enormously rich in spectroscopic atomic lines that hold information on, for instance, composition, temperature, and surface gravity of stellar objects, while the X-ray band provides unique information on energetic processes related to accreting binary systems, active galactic nuclei, supernovae, and many more. Often only the combination of data from several wavelength bands yields a deeper understanding of these objects aiding to constrain astrophysical and cosmological theories.

An advanced MCP detector for the application in a spaceborne UV instrument on a satellite observatory is currently under development at the IAAT. The key development items are a sensitive photocathode and the application of a cross-strip anode in conjunction with low power dissipation readout electronics. In the scope of the present thesis, an adaptable MCP test setup in a vacuum chamber was developed and constructed that is similar to the configuration of the finally desired sealed-tube detector. The intention was to provide realistic signal stimuli and conditions for the evaluation of a new cross-strip anode and the corresponding electronics. A second application was the initial electron scrubbing and conditioning of raw and untreated MCPs. A comprehensive description of the planned detector and front-end electronics design was published in Diebold et al. (2013b). The article includes also commissioning results of the readout electronics and outlines the MCP test setup.

The harsh space environment, e.g. large differences and rapid changes in temperature, micro-meteorites and high velocity debris particles, as well as various types of particle radiation, applies enormous stress to materials and electronics aboard a satellite. Particularly the performance of X-ray detectors can be degraded by soft proton radiation, thus requiring extensive evaluation to assess the end-of-life performance. Therefore, a setup for the soft proton irradiation of silicon sensors for X-ray astronomy as well as for other exposed and potentially vulnerable satellite parts was developed and constructed. The key features were a high flux uniformity over a large area and an independent monitoring system for the applied fluence and spectrum. The experimental setup is presented in Diebold et al. (2013a) along with calibration data and measurement results

that show the spectral and flux uniformity performance. The setup was used for two irradiation campaigns for silicon drift detector prototypes for *LOFT* and a test of two coated optics samples for *ADM-Aeolus*.

Even before the discovery of damages of the *Chandra ACIS* instrument it was well-known that Wolter-type X-ray optics focus also soft proton radiation and, therefore, lead to a concentration of the ambient orbital proton flux on X-ray sensors in the focal plane of the instrument. Besides a possible degradation of the detection performance, an enhancement of the observational background can occur. Up to now, experimental data of grazing angle proton scattering on X-ray mirrors were just sparsely reported. In order to improve this situation, the soft proton irradiation setup in Tübingen was upgraded to a grazing incidence scattering experiment. A new method was found to determine the incident flux and monitor it during measurements. A substantial set of measurements was obtained with two samples from an *eROSITA* spare mirror shell. Simulations of optimized aperture designs and preliminary test results were reported in Diebold et al. (2014a), while the actual scattering efficiency data were published in Diebold et al. (2015). The latter article comprises a detailed discussion of the results including the comparison to a previous experiment, to a proposed theoretical description, and to semi-empirical simulations. Improvements to enhance the capabilities of the setup are proposed in the present thesis, to extend the empirical data base even more in the future.

Bibliography

Agostinelli, S., Allison, J., Amako, K., Apostolakis, J., Araujo, H., et al. (2003). "GEANT4 - a simulation toolkit". In: *Nuclear Instruments and Methods in Physics Research A* 506, pp. 250–303. DOI: `10.1016/S0168-9002(03)01368-8`.

Barnstedt, J. (1985). "Entwicklung eines photonenzählenden transportablen Kamerasystems für astronomische Anwendungen im sichtbaren Spektralbereich". PhD thesis. Eberhard Karls Universität Tübingen.

Becker-Ross, H., Florek, S., Grewing, M., Kappelmann, N., Kraemer, G., et al. (1994). "Spectrum ultraviolet mission (SUV): a general purpose ultraviolet observatory". In: *Space Optics 1994: Earth Observation and Astronomy*. Ed. by M. G. Cerutti-Maori and P. Roussel. Vol. 2209. Society of Photo-Optical Instrumentation Engineers (SPIE) Conference Series, pp. 557–567.

Bohm, D. and Pines, D. (1953). "A Collective Description of Electron Interactions: III. Coulomb Interactions in a Degenerate Electron Gas". In: *Physical Review* 92, pp. 609–625. DOI: `10.1103/PhysRev.92.609`.

Brandt, S., Hernanz, M., Alvarez, L., Argan, A., Artigues, B., et al. (2014). "The design of the wide field monitor for the LOFT mission". In: *Society of Photo-Optical Instrumentation Engineers (SPIE) Conference Series*. Vol. 9144. Society of Photo-Optical Instrumentation Engineers (SPIE) Conference Series, p. 2. DOI: `10.1117/12.2055885`. arXiv: `1408.6540` `[astro-ph.IM]`.

Brosch, N. (2009). "Exotic UV astronomy". In: *Astrophysics and Space Science* 320, pp. 207–215. DOI: `10.1007/s10509-009-9988-7`.

Burwitz, V., Predehl, P., Friedrich, P., Bräuninger, H., Eder, J., et al. (2014). "The calibration and testing of the eROSITA X-ray mirror assemblies". In: *Society of Photo-Optical Instrumentation Engineers (SPIE) Conference Series*. Vol. 9144. Society of Photo-Optical Instrumentation Engineers (SPIE) Conference Series, p. 1. DOI: `10.1117/12.2056739`.

Dabiran, A. M., Wowchak, A. M., Chow, P. P., Siegmund, O. H. W., Hull, J. S., et al. (2009). "Direct deposition of GaN-based photocathodes on microchannel plates". In: *Society of Photo-Optical Instrumentation Engineers (SPIE) Conference Series*. Vol. 7212. Society of Photo-Optical Instrumentation Engineers (SPIE) Conference Series, p. 13. DOI: `10.1117/12.809503`.

Davies, J. K. (1997). *Astronomy from space: the design and operation of orbiting observatories.*

Del Monte, E., Azzarello, P., Bozzo, E., Bugiel, S., Diebold, S., et al. (2014a). "Radiation tests of the silicon drift detectors for LOFT". In: *Society of Photo-Optical Instrumentation Engineers (SPIE) Conference Series.* Vol. 9144. Society of Photo-Optical Instrumentation Engineers (SPIE) Conference Series, p. 64. DOI: `10.1117/12.2055747`. arXiv: `1408.6548 [astro-ph.IM]`.

Del Monte, E., Rachevski, A., Zampa, G., Zampa, N., Azzarello, P., et al. (2014b). "Measurement of the effect of non ionising energy losses on the leakage current of silicon drift detector prototypes for the LOFT satellite". In: *Journal of Instrumentation* 9, P07016, 7016P. DOI: `10.1088/1748-0221/9/07/P07016`. arXiv: `1405.5466 [astro-ph.IM]`.

Dichter, B. K. and Woolf, S. (2003). "Grazing angle proton scattering: effects on chandra and xmm-newton x-ray telescopes". In: *IEEE Transactions on Nuclear Science* 50, pp. 2292–2295. DOI: `10.1109/TNS.2003.822092`.

Diebold, S., Azzarello, P., Del Monte, E., Feroci, M., Jochum, J., et al. (2013a). "A setup for soft proton irradiation of X-ray detectors for future astronomical space missions". In: *Nuclear Instruments and Methods in Physics Research A* 721, pp. 65–72. DOI: `10.1016/j.nima.2013. 04.049`. arXiv: `1307.4204 [astro-ph.IM]`.

Diebold, S., Barnstedt, J., Hermanutz, S., Kalkuhl, C., Kappelmann, N., et al. (2013b). "UV MCP Detectors for WSO-UV: Cross Strip Anode and Readout Electronics". In: *IEEE Transactions on Nuclear Science* 60, pp. 918–922. DOI: `10.1109/TNS.2013.2248096`.

Diebold, S., Jochum, J., Kendziorra, E., Perinati, E., Santangelo, A., et al. (2014a). "A Facility for Soft Proton Irradiation and Instrument Testing for Future Space Missions". In: *IEEE Transactions on Nuclear Science* 61, pp. 1937–1942. DOI: `10.1109/TNS.2013.2292711`.

– (2014b). "A setup for soft proton scattering on x-ray mirrors". In: *Society of Photo-Optical Instrumentation Engineers (SPIE) Conference Series.* Vol. 9144. Society of Photo-Optical Instrumentation Engineers (SPIE) Conference Series, p. 4. DOI: `10.1117/12.2054887`.

Diebold, S., Tenzer, C., Perinati, E., Santangelo, A., Freyberg, M., et al. (2015). "Soft proton scattering efficiency measurement on x-ray mirror shells". In: *Experimental Astronomy.* DOI: `10.1007/s10686-015-9451-4`.

Feroci, M., den Herder, J. W., Bozzo, E., Barret, D., Brandt, S., et al. (2014). "The Large Observatory for x-ray timing". In: *Society of Photo-Optical Instrumentation Engineers (SPIE) Conference Series.* Vol. 9144. Society of Photo-Optical Instrumentation Engineers (SPIE) Conference Series, p. 2. DOI: `10.1117/12.2055913`. arXiv: `1408.6526 [astro-ph.IM]`.

Firsov, O. B. (1967). "Reflection of Fast Ions from a Dense Medium at Glancing Angles". In: *Soviet Physics Doklady* 11, p. 732.

Fraser, G. W. (1989). *X-ray Detectors in Astronomy.*

Giacconi, R., Gursky, H., and van Speybroeck, L. P. (1968). "Observational Techniques in X-Ray Astronomy". In: *Annual Review of Astronomy and Astrophysics* 6, p. 373. DOI: 10.1146/annurev.aa.06.090168.002105.

Grewing, M., Appenzeller, I., Barnstedt, J., Bowyer, S., Hurwitz, M., et al. (1998). "ORFEUS". In: *Ultraviolet Astrophysics Beyond the IUE Final Archive*. Ed. by W. Wamsteker, R. Gonzalez Riestra, and B. Harris. Vol. 413. ESA Special Publication, p. 757.

Hermanutz, S., Barnstedt, J., Diebold, S., Elsener, H. R., Kalkuhl, C., et al. (2014). "An introduction to the IAAT ultraviolet MCP detector development". In: *Society of Photo-Optical Instrumentation Engineers (SPIE) Conference Series*. Vol. 9144. Society of Photo-Optical Instrumentation Engineers (SPIE) Conference Series, p. 34. DOI: 10.1117/12.2054888.

Jansen, F., Lumb, D., Altieri, B., Clavel, J., Ehle, M., et al. (2001). "XMM-Newton observatory. I. The spacecraft and operations". In: *Astronomy & Astrophysics* 365, pp. L1–L6. DOI: 10.1051/0004-6361:20000036.

Kendziorra, E., Clauss, T., Meidinger, N., Kirsch, M., Kuster, M., et al. (2000). "Effect of low-energy protons on the performance of the EPIC pn-CCD detector on XMM-Newton". In: *X-Ray and Gamma-Ray Instrumentation for Astronomy XI*. Ed. by K. A. Flanagan and O. H. Siegmund. Vol. 4140. Society of Photo-Optical Instrumentation Engineers (SPIE) Conference Series, pp. 32–41.

Kuntz, K. D. and Snowden, S. L. (2008). "The EPIC-MOS particle-induced background spectra". In: *Astronomy & Astrophysics* 478, pp. 575–596. DOI: 10.1051/0004-6361:20077912.

Kushpil, S., Crescio, E., Giubellino, P., Idzik, M., Kolozhvari, A., et al. (2006). "Beam test results of the irradiated silicon drift detector for ALICE". In: *Nuclear Instruments and Methods in Physics Research A* 566, pp. 94–99. DOI: 10.1016/j.nima.2006.05.057. eprint: physics/0512057.

Lei, F., Nartallo, R., Nieminen, P., Daly, E., Evans, H., et al. (2004). "Update on the Use of Geant4 for the Simulation of Low-Energy Protons Scattering Off X-Ray Mirrors at Grazing Incidence Angles". In: *IEEE Transactions on Nuclear Science* 51, pp. 3408–3412. DOI: 10.1109/TNS.2004.839160.

Lo, D. H. and Srour, J. R. (2003). "Modeling of proton-induced ccd degradation in the chandra x-ray observatory". In: *IEEE Transactions on Nuclear Science* 50, pp. 2018–2023. DOI: 10.1109/TNS.2003.820735.

Löchner, S. and Schmelling, M. *The Beetle Reference Manual - chip version 1.3, 1.4 and 1.5*. Max Planck Institute for Nuclear Physics, Heidelberg, Germany.

Löchner, S. (2006). "Development, Optimisiation and Characterisation of a Radiation Hard Mixed-Signal Readout Chip for LHCb". PhD thesis. Ruperto-Carola University of Heidelberg.

Bibliography

Lumb, D. H., Warwick, R. S., Page, M., and De Luca, A. (2002). "X-ray background measurements with XMM-Newton EPIC". In: *Astronomy & Astrophysics* 389, pp. 93–105. DOI: `10.1051/0004-6361:20020531`. eprint: `astro-ph/0204147`.

Madsen, K. K., Harrison, F. A., An, H., Boggs, S. E., Christensen, F. E., et al. (2014). "The nuclear spectroscopic telescope array (NuSTAR) high-energy X-ray mission". In: *Society of Photo-Optical Instrumentation Engineers (SPIE) Conference Series*. Vol. 9144. Society of Photo-Optical Instrumentation Engineers (SPIE) Conference Series, p. 1. DOI: `10.1117/12.2056643`.

Moll, M., Fretwurst, E., Kuhnke, M., and Lindström, G. (2002). "Relation between microscopic defects and macroscopic changes in silicon detector properties after hadron irradiation". In: *Nuclear Instruments and Methods in Physics Research B* 186, pp. 100–110. DOI: `10.1016/S0168-583X(01)00866-7`.

Nartallo, R., Evans, H., Daly, E., Hilgers, A., Nieminen, P., et al. (2000). *Radiation Environment Induced Degradation on Chandra and Implications for XMM*. Tech. rep. ESA.

Petrov, A. N., Grigoryan, O. R., and Kuznetsov, N. V. (2009). "Creation of model of quasi-trapped proton fluxes below Earth's radiation belt". In: *Advances in Space Research* 43, pp. 654–658. DOI: `10.1016/j.asr.2008.11.019`.

Pfeifer, M., Diebold, S., Barnstedt, J., Hermanutz, S., Kalkuhl, C., et al. (2014). "Low power readout electronics for a UV MCP detector with cross strip anode". In: *Journal of Instrumentation* 9, C03059, p. C3059. DOI: `10.1088/1748-0221/9/03/C03059`.

Pfeifer, M. (2014). "Development of low power readout electronics for micro channel plate detectors with cross strip anodes for UV space observatories". PhD thesis. Eberhard Karls Universität Tübingen.

Photonis (2009). *Datasheet: ELECTROGEN Electron Generator Arrays*. Photonis. URL: `http://www.photonis.com/en/ism/33-electron-generator-arrays.html#idTab9`.

Pines, D. and Bohm, D. (1952). "A Collective Description of Electron Interactions: II. Collective vs Individual Particle Aspects of the Interactions". In: *Physical Review* 85, pp. 338–353. DOI: `10.1103/PhysRev.85.338`.

Predehl, P., Andritschke, R., Becker, W., Bornemann, W., Bräuninger, H., et al. (2014). "eROSITA on SRG". In: *Society of Photo-Optical Instrumentation Engineers (SPIE) Conference Series*. Vol. 9144. Society of Photo-Optical Instrumentation Engineers (SPIE) Conference Series, p. 1. DOI: `10.1117/12.2055426`.

Rachevski, A., Zampa, G., Zampa, N., Campana, R., Evangelista, Y., et al. (2014). "Large-area linear Silicon Drift Detector design for X-ray experiments". In: *Journal of Instrumentation* 9, P07014, 7014P. DOI: `10.1088/1748-0221/9/07/P07014`.

Rasmussen, A., Chervinsky, J., and Golovchenko, J. (1999). *Proton scattering off of XMM optics: XMM mirror and RGS grating samples.* Tech. rep. RGS-COL-CAL-99009. Columbia Astrophysical Laboratory.

Segneri, G., Brown, C., Carpenter, J.-D., Kuhnle, B., Lauf, T., et al. (2009). "Measurement of the Current Related Damage Rate at $-50°$ C and Consequences on Macropixel Detector Operation in Space Experiments". In: *IEEE Transactions on Nuclear Science* 56, pp. 3734–3742. DOI: 10.1109/TNS.2009.2033911.

Shustov, B., Sachkov, M., Gómez de Castro, A. I., Huang, M., Werner, K., et al. (2009). "WSO-UV - ultraviolet mission for the next decade". In: *Astrophysics and Space Science* 320, pp. 187–190. DOI: 10.1007/s10509-008-9817-4.

Siegmund, O. H. W., Tremsin, A. S., Vallerga, J. V., McPhate, J. B., Hull, J. S., et al. (2008). "Gallium nitride photocathode development for imaging detectors". In: *Society of Photo-Optical Instrumentation Engineers (SPIE) Conference Series.* Vol. 7021. Society of Photo-Optical Instrumentation Engineers (SPIE) Conference Series, p. 1. DOI: 10.1117/12.790076.

Spieler, H. (2005). *Semiconductor Detector Systems.* Ed. by R. J. Nicholas and H. Kamimura. Oxford University Press.

Stoffelen, A., Pailleux, J., Källén, E., Vaughan, J. M., Isaksen, L., et al. (2005). "The Atmospheric Dynamics Mission for Global Wind Field Measurement". In: *Bulletin of the American Meteorological Society* 86.1, pp. 73–87. DOI: 10.1175/BAMS-86-1-73.

Tenzer, J.-C. (2008). "Monte-Carlo Background Studies for Space-Based Detectors in X-ray Astronomy". PhD thesis. Eberhard-Karls-Universität zu Tübingen.

Tremsin, A. S., Vallerga, J. V., Siegmund, O. H. W., and Hull, J. S. (2003). "Centroiding algorithms and spatial resolution of photon counting detectors with cross-strip anodes". In: *UV/EUV and Visible Space Instrumentation for Astronomy II.* Ed. by O. H. W. Siegmund. Vol. 5164. Society of Photo-Optical Instrumentation Engineers (SPIE) Conference Series, pp. 113–124. DOI: 10.1117/12.508409.

Vallerga, J., Raffanti, R., Tremsin, A., Siegmund, O., McPhate, J., et al. (2010). "Large-format high-spatial resolution cross-strip readout MCP detectors for UV astronomy". In: *Society of Photo-Optical Instrumentation Engineers (SPIE) Conference Series.* Vol. 7732. Society of Photo-Optical Instrumentation Engineers (SPIE) Conference Series, p. 3. DOI: 10.1117/12.857820.

Volyanskyy, D. (2013). "The LHCb experiment: status and recent results". In: *European Physical Journal Web of Conferences.* Vol. 52. European Physical Journal Web of Conferences, p. 1005. DOI: 10.1051/epjconf/20125201005. arXiv: 1302.1891 [hep-ex].

Bibliography

Weisskopf, M. C., Aldcroft, T. L., Bautz, M., Cameron, R. A., Dewey, D., et al. (2003). "An Overview of the Performance of the Chandra X-ray Observatory". In: *Experimental Astronomy* 16, pp. 1–68. DOI: 10.1023/B:EXPA.0000038953.49421.54. eprint: astro-ph/0503319.

Werner, K., Barnstedt, J., Gringel, W., Kappelmann, N., Becker-Roß, H., et al. (2008). "HIRDES The High-Resolution Double-Echelle Spectrograph for the World Space Observatory Ultraviolet (WSO/UV)". In: *Advances in Space Research* 41, pp. 1992–1997. DOI: 10.1016/j.asr.2007.11.029. arXiv: 0711.4255.

Wilkinson, P. G. and Andrew, K. L. (1963). "Proposed standard wavelengths in the vacuum ultraviolet. Spectra of Ge, Ne, C, Hg, and N". In: *Journal of the Optical Society of America (1917-1983)* 53, p. 710.

Winter, H., Wilke, M., and Bergomaz, M. (1997). "Energy loss of fast protons in grazing scattering from an Al(111)-surface". In: *Nuclear Instruments and Methods in Physics Research B* 125, pp. 124–127. DOI: 10.1016/S0168-583X(96)00803-8.

Wiza, J. L. (1979). "Microchannel plate detectors". In: *Nuclear Instruments and Methods* 162, pp. 587–601. DOI: 10.1016/0029-554X(79)90734-1.

Wolter, H. (1952). "Spiegelsysteme streifenden Einfalls als abbildende Optiken für Röntgenstrahlen". In: *Annalen der Physik* 445, pp. 94–114. DOI: 10.1002/andp.19524450108.

Zane, S., Walton, D., Kennedy, T., Feroci, M., Den Herder, J.-W., et al. (2014). "The large area detector of LOFT: the Large Observatory for X-ray Timing". In: *Society of Photo-Optical Instrumentation Engineers (SPIE) Conference Series*. Vol. 9144. Society of Photo-Optical Instrumentation Engineers (SPIE) Conference Series, p. 2. DOI: 10.1117/12.2054654. arXiv: 1408.6539 [astro-ph.IM].

Ziegler, J. F., Ziegler, M. D., and Biersack, J. P. (2010). "SRIM - The stopping and range of ions in matter (2010)". In: *Nuclear Instruments and Methods in Physics Research B* 268, pp. 1818–1823. DOI: 10.1016/j.nimb.2010.02.091.

Acknowledgments

I would like to express my gratefulness to all the people who supported me throughout the course of my studies and contributed to the present thesis. In particular, I wish to thank my colleagues and friends at the IAAT at the Sand for the comfortable and familiar atmosphere during productive working hours, for interesting discussions during lunch and coffee breaks, and for the joint sports activities.

Several people have contributed to this thesis in a special way and deserve mentioning:

- **Prof. Dr. Klaus Werner**
  for sparking my interest in astronomy and the associated technologies, for friendly advising and supervising, and for encouraging me to follow all my research interests.

- **Prof. Dott. Andrea Santangelo**
  for kindly supervising and supporting the projects related to X-ray instrumentation at the accelerator facility.

- **Dr. Chris Tenzer**
  for mentoring with great enthusiasm, for innumerable helpful suggestions and contributions, and for the review and correction of several publications.

- **All members of the MCP detector group and my collaborators working on X-ray instrumentation**
  for excellent teamwork and cooperation as well as for friendly and immediate support at all times.

- **Thomas Schanz**
  for the generous and spontaneous help with the accelerator, for inspiring discussions, and for the thorough review of this thesis.

- **My parents Christine & Jakob Diebold and my girlfriend Sonja Liebendörfer**
  for support and backup in all circumstances.

Lebenslauf

31.10.1984	geboren in Reutlingen
1991–1995	August-Lämmle-Grundschule, Kusterdingen
1995–2004	Wildermuth-Gymnasium, Tübingen
2004	Abitur
2004–2005	Albert-Ludwigs-Universität Freiburg, Studium der Physik
2005–2011	Eberhard Karls Universität Tübingen, Studium der Physik
2006–2009	Eberhard Karls Universität Tübingen, Studium der Philosophie
04.2007–01.2014	wissenschaftliche Hilfskraft am Physikalischen Institut, am Institut für Theoretische Physik und am Institut für Astronomie und Astrophysik (IAAT) der Universität Tübingen
10.2009–10.2010	Anfertigung der Diplomarbeit mit dem Titel *Bestimmung der Stöchiometrie supraleitender Proben mittels Rutherford-Rückstreu-Spektrometrie* unter der Anleitung von Prof. Dr. J. Jochum
09.2010	Philosophikum der Fakultät für Philosophie und Geschichte der Universität Tübingen
01.2011	Physikdiplom
02.2011–01.2014	Stipendium des Kepler Center for Astro and Particle Physics der Universität Tübingen
ab 02.2014	wissenschtlicher Angestellter am IAAT
02.2011–02.2015	Anfertigung der Dissertation mit dem Titel *Development and Testing of Instrumentation for Space-Based Ultraviolet and X-Ray Astronomy* unter der Anleitung von Prof. Dr. K. Werner und Prof. Dott. A. Santangelo

Meine akademischen Lehrer waren die folgenden Professoren und Dozenten:

Astronomie und Astrophysik: N. Kappelmann, W. Kley, T. Nagel, A. Santangelo,
K. Werner

Chemie: N. Kuhn, H. Mayer

Experimentalphysik: P. Grabmayr, T. Hehl, J. Jochum, D. Kölle, D. Wharam

Kern- und Teilchenphysik: A. Buchmann, H. Clement, T. Gutsche, R. Meier

Mathematik: M. O. Ahmedou, A. Deitmar

Philosophie: E.-M. Engels, I. Goy, M. Heidelberger, M. Neuber

Theoretische Physik: M. Liu, H. Müther, H. Reinhardt, K. W. Schmid, N. Schopohl